Gas Foil Bearing: Effect of Foil Materials and Stability Analysis Using Different Models for Foil Structure

A Thesis Submitted in
Partial Fulfillment of the Requirements
for the Degree of

Doctor of Philosophy

by

T. Moasunep Jamir
(Roll No. 10610318)

Department of Mechanical Engineering
Indian Institute of Technology Guwahati,
Guwahati-781039, INDIA
April 2015

Department of Mechanical Engineering

Indian Institute of Technology Guwahati

Guwahati-781039, India

THESIS CERTIFICATE

It is certified that the work contained in the thesis entitled **"Gas Foil Bearing: Effect of Foil Materials and the Stability Analysis Using Different Models for Foil Structure"** by **T. Moasunep Jamir**, a student in the Department of Mechanical Engineering, Indian Institute of Technology Guwahati, India, for the award of the degree of the Doctor of Philosophy has been carried out under our supervision and that this work has not been submitted elsewhere for a degree.

Dr. S. K. Kakoty

Professor
Department of Mechanical Engineering
Indian Institute of Technology Guwahati

Dr. Karuna Kalita

Associate Professor
Department of Mechanical Engineering
Indian Institute of Technology Guwahati

Dedicated to my Loving Parents,

Mrs. Longritola Walling *and*

Late. Mr. Tongpangchiba Jamir

Acknowledgment

At the onset of the completion of this work, first and foremost my gratefulness goes to God the Almighty, once and for all.

It gives me immense sense of privilege and honor to acknowledge my PhD supervisors Prof. S. K. Kakoty and Dr. Karuna Kalita, for their exceptional supervising. Their insightful thoughts and innovation with an unfailing encouragement, love and support, were the concealed strength all throughout those years for which I am forever grateful. They not only became my professional mentors but also endeavored a nexus even in personal welfare, which eventually became the two pillars of reverence in my life.

I would like to express my sincere gratitude to Prof. S. K. Dwivedy, Prof. Amarendra Kumar Das and Dr. Atanu Banerjee, for their untiring surveillance as being members of my Doctoral Committee contributing ingenious suggestions, innovative outsets and active cooperation during the entire period of the research.
My sincere gratefulness to Prof. Anoop. K. Dass, Head, Department of Mechanical Engineering, for providing the accessibility for all the research facilities and laboratories in the Department of Mechanical Engineering, IIT Guwahati.

IIT Guwahati has been a place to call home which was made possible and enriched through interaction and intimacy with faculties, friends and fellow research scholars. Mr. T. T. Haokip and family, Dr. Lindoh and family, Dr. D. Pamu and family, Prof. U. S. Dixit, Daniel Vemagiri Marbaniang, Naveen Nischal, Dari, Onisha, Auri, Vinoh Swu, Ruchi, Ravi, Syed Nayab Rasool, Yeka Awomi, Aleem, Arvind, Vinod Yadav and all the IITG EU members.

I would like to take this opportunity to express my earnest gratitude and respect to my father, Late. Shri. Tongpangchiba Jamir, my model and my treasure, who left for his heavenly abode during the course of my studies and to my unconditional loving

mother Mrs. Longritola Walling, without whom things wouldn't be a reality. My gratefulness encompasses to all my affectionate family members, in-laws, niece and nephews for embracing me morally and continually upholding in prayers. Indeed, through and through it all, it's the support, love and your enduring spirits that moved me to be what I am now. Thank you so much.

Lastly, sincere gratitude to all the well wishes over the years whom I could not mention. May God bless you all.

T. Moasunep Jamir

TABLE OF CONTENTS

Acknowledgement i

Table of Contents iii

List of Figures vii

List of Tables xi

Nomenclature xii

Abstract xv

Chapter 1 **INTRODUCTION AND LITERATURE REVIEW**

1.1 Introduction 01

1.1.1 Why foil bearings 03

1.1.2 Foil bearing technology 05

1.2 State of the Art 07

1.3 Literature Review 09

1.3.1 Overview 09

1.3.2 Theoretical GFB models and predictions 10

1.3.3 Structural characteristics 15

1.3.4 Thermal predictions, high speed and high temperature operations 19

1.3.5 Distinct applications and operations 22

1.4 Objectives of the Present Work 24

1.5 Organization of the Thesis 26

Chapter 2 **BASIC EQUATIONS AND DESCRIPTION OF GAS FOIL BEARINGS (GFBs)**

2.1 Introduction 28

2.2 Description of Bump Type Gas Foil Bearing (GFB) 28

2.3 Basic Governing Equations 30

2.4 Steady State Formulation of Reynolds Equation 32

2.4.1 Solution method 35

2.4.2 Newton-Raphson method 36
2.5 Time Transient Stability Analysis 38
2.5.1 Equations of motion of a rigid rotor supported on journal bearings 38
2.5.2 Implementation of Runge-Kutta method to the equations of motion 41
2.6 Summary 44

Chapter 3 **DIFFERENT NUMERICAL MODELS OF THE FOIL STRUCTURE**

3.1 Introduction 45
3.2 Simple Elastic Foundation Model 46
3.3 1D Beam Model for Top Foil 48
3.3.1 Normalization of the governing equation of the top foil 49
3.3.2 Discretization of the governing equation using finite element formulation 50
3.3.3 Calculation of load vector from the pressure obtained from Reynolds equation 55
3.3.4 Coupling of FE solution with the FDM solution 56
3.4 2D Model for Top Foil 56
3.4.1 Classical plate theory model (CPT) 57
3.4.1.1 Normalization of the governing equation of the top foil 59
3.4.1.2 Discretization of the governing equation using finite element formulation 60
3.4.1.3 Calculation of load vector from the pressure obtained from Reynolds equation 63
3.4.1.4 Coupling of FE solution with the FDM solution 64
3.4.2 Shear deformation plate theory (SDT) 64
3.4.2.1 Normalization of the governing equation of the top foil 66
3.4.2.2 Discretization of the governing equation using finite element formulation 67

3.4.2.3 Calculation of load vector from the pressure obtained from Reynolds equation 70
3.4.2.4 Coupling of FE solution with the FDM solution 71
3.5 Summary 71

Chapter 4 **STEADY STATE CHARACTERISTICS OF GFBs**

4.1 Introduction 73
4.2 Methodology 73
4.3 Validation 75
4.3.1 Comparison with published theoretical results 75
4.3.2 Comparison with published experimental results 76
4.4 Steady State Characteristics 79
4.4.1 Pressure distribution, film thickness and top foil deflection 79
4.4.2 Load carrying capacity of GFBs for different top foil models 85
4.4.3 Effect of bearing number on the load carrying capacity of GFBs for different top foil models 86
4.4.4 Attitude angle of GFB for different top foil model 87
4.4.5 Effect of compliance coefficient on the load carrying capacity of GFBs 88
4.5 Summary 89

Chapter 5 **STABILITY ANALYSIS OF GAS FOIL JOURNAL BEARING**

5.1 Introduction 91
5.2 Stability Analysis 91
5.3 Non-linear Transient Stability Analysis 92
5.3.1 Effect of bearing number on stability 98
5.3.2 Effect of eccentricity ratio on stability 100
5.3.3 Effect of compliance coefficient on stability 101
5.4 Computational Time 103
5.5 Table Showing the Summary of Important Results 104
5.6 Summary 106

Chapter 6 **EFFECT OF BUMP FOIL MATERIALS ON GAS FOIL BEARINGS LOAD PERFORMANCE**

6.1 Introduction 107
6.2 GFBs Geometry and Compliance Coefficient 107
6.3 Load Capacity of GFBs with Different Foil Materials 109
6.4 Summary 113

Chapter 7 **CONCLUSIONS AND FUTURE SCOPE**

7.1 Conclusions 114
7.2 Scope for Future Work 118

References 120

LIST OF FIGURES

Fig. 1.1	Schematic views of two typical GFBs	01
Fig. 1.2	Principle of an air bearing [7]	06
Fig. 1.3	Hydrodynamic pressure generation [7]	06
Fig. 1.4	Comparison of operating principles of a liquid-lubricated journal bearing and a gas foil journal bearing [8]	07
Fig: 2.1	Schematic view of a bump type GFB	29
Fig. 2.2	An exfoliated view of a bearing showing the mesh size	33
Fig. 2.3	The coordinate system and the sign convention of the journal forces	34
Fig. 2.4	Flowchart of solution algorithm	37
Fig. 2.5	Rotor-Bearing configuration	39
Fig. 2.6	Plan circular journal bearing	39
Fig. 3.1	A single segment of bump foil	47
Fig. 3.2	1D Structural model of top foil	49
Fig. 3.3	A 1D beam element	50
Fig. 3.4	An exfoliated view of a bearing showing the mesh for finite difference mesh	52
Fig. 3.5	An exfoliated view of a bearing showing the mesh for 1D finite element mesh	53
Fig. 3.6	A finite element showing the nodal hydrodynamic gas pressure obtained by solving Reynolds equation	55
Fig. 3.7	Configuration of top foil supported on bump strips and its 2D structural model	57

Fig. 3.8	Details of one FE element	57
Fig. 3.9	Linear element for CPT with three degrees of freedom $\left(W, \frac{\partial W}{\partial \theta}, -\frac{\partial W}{\partial Z}\right)$ per node	60
Fig. 3.10	An exfoliated view of a bearing showing the mesh for 2D finite element mesh	62
Fig. 3.11	A finite element showing the nodal hydrodynamic gas pressure obtained by solving Reynolds equation	63
Fig. 3.12	Linear element for SDT with three degrees of freedom (W, ϕ_θ, ϕ_Z) per node	67
Fig. 4.1	Journal attitude angle Vs. static load for shaft speed of 45,000 rpm	77
Fig. 4.2	Minimum flim thickness Vs. static load for shaft speed of 45,000 rpm	78
Fig. 4.3	Pressure distribution of GFBs with simple foil structure model for ε = 0.6, L/D=1, S=1, Λ=1	80
Fig. 4.4	Flim thickness of GFBs with simple foil structure model for ε = 0.6, L/D=1, S=1, Λ=1	80
Fig. 4.5	Top foil deflection of GFBs with simple foil structure model for ε = 0.6, L/D=1, S=1, Λ=1	81
Fig. 4.6	Pressure distribution of GFBs with 1D foil structure model for ε = 0.6, L/D=1, S=1, Λ=1	81
Fig. 4.7	Flim thickness of GFBs with 1D foil structure model for ε = 0.6, L/D=1, S=1, Λ=1	82
Fig. 4.8	Top foil deflection of GFBs with 1D foil structure model for ε = 0.6, L/D=1, S=1, Λ=1	82
Fig. 4.9	Pressure distribution of GFBs with 2D CPT foil structure model for ε = 0.6, L/D=1, S=1, Λ=1	83

Fig. 4.10	Flim thickness of GFBs with 2D CPT foil structure model for ε = 0.6, L/D=1, S=1, Λ=1	83
Fig. 4.11	Top foil deflection of GFBs with 2D CPT foil structure model for ε = 0.6, L/D=1, S=1, Λ=1	83
Fig. 4.12	Pressure distribution of GFBs with 2D SDT foil structure model for ε = 0.6, L/D=1, S=1, Λ=1	84
Fig. 4.13	Flim thickness of GFBs with 2D SDT foil structure model for ε = 0.6, L/D=1, S=1, Λ=1	84
Fig. 4.14	Top foil deflection of GFBs with 2D SDT foil structure model for ε = 0.6, L/D=1, S=1, Λ=1	85
Fig. 4.15	Effect of eccentricity ratio (ε) on the load carrying capacity ($\bar{W}$) of GFB for different top foil models	85
Fig. 4.16	Effect of bearing number (Λ) on the load carrying capacity ($\bar{W}$) of GFB for different top foil models	87
Fig. 4.17	Effect of eccentricity ratio (ε) on the attitude angle (ϕ) of GFB for different top foil model	88
Fig. 4.18	Effect of compliance coefficient (S) on the load carrying capacity ($\bar{W}$) of GFB	89
Fig. 5.1	Trajectory of journal centre for simple model for L/D=1, ε =0.3, S=1, Λ =1, $\bar{M}$ =9	94
Fig. 5.2	Trajectory of journal centre for simple model for L/D=1, ε =0.3, S=1, Λ =1, $\bar{M}$ =16.9	94
Fig. 5.3	Trajectory of journal centre for simple model for L/D=1, ε =0.3, S=1, Λ =1, $\bar{M}$ =18	95
Fig. 5.4	Trajectory of journal centre for 1D model for L/D=1, ε =0.3, S=1, Λ =1, $\bar{M}$ =12	95
Fig 5.5	Trajectory of journal centre for 1D model for L/D=1, ε =0.3, S=1, Λ =1, $\bar{M}$ =14.8	95

Fig 5.6	Trajectory of journal centre for 1D model for L/D=1, ε =0.3, S=1, Λ =1, $\bar{M}$ =16.4	96
Fig. 5.7	Trajectory of journal centre for 2D CPT model for L/D=1, ε =0.2, S=1, Λ =2, $\bar{M}$ =8	96
Fig. 5.8	Trajectory of journal centre for 2D CPT model for L/D=1, ε =0.2, S=1, Λ =1, $\bar{M}$ =12.4	96
Fig. 5.9	Trajectory of journal centre for 2D CPT model for L/D=1, ε =0.2, S=1, Λ =1, $\bar{M}$ =14.5	97
Fig. 5.10	Trajectory of journal centre for 2D SDT model for L/D=1, ε =0.3, S=1, Λ =1, $\bar{M}$ =10	97
Fig. 5.11	Trajectory of journal centre for 2D SDT model for L/D=1, ε =0.3, S=1, Λ =1, $\bar{M}$ =11.3	97
Fig. 5.12	Trajectory of journal centre for 2D SDT model for L/D=1, ε =0.3, S=1, Λ =1, $\bar{M}$ =12	98
Fig. 5.13	Effect of bearing number (Λ) on the critical mass parameter ($\bar{M}$) of GFBs with different foil models for L/D=1, ε =0.3, S=1	99
Fig. 5.14	Effect of eccentricity ratio (ε) on critical mass parameter ($\bar{M}$) of GFBs with different foil models (L/D=1, Λ =1, S=1)	100
Fig. 5.15	Effect of bearing number (Λ) and compliance coefficient *(S)* on critical mass parameter ($\bar{M}$) for L/D=1, ε =0.3	101
Fig. 5.16	Plot showing critical mass parameter ($\bar{M}$) versus compliance coefficient *(S)*, for different Bearing Numbers (Λ) for a simple foil model of the GFBs	102
Fig. 5.17	Plot showing critical mass parameter ($\bar{M}$) for different Bearing Numbers (Λ) and eccentricity ratio (ε) for a simple foil model of the GFBs	103
Fig. 6.1	Comparison of load carrying capacity ($\bar{W}$) of GFBs and plain gas bearings (GBs)	110

Fig. 6.2 Load carrying capacity ($\bar{W}$) with respect to eccentricity ratio (ε) of GFBs with different foil materials 111

Fig. 6.3 Journal attitude angle (ϕ) versus load carrying capacity ($\bar{W}$) for GFB with different foil materials 112

LIST OF TABLES

Table 4.1	Steady state characteristics for L/D=1.0, S=0	76
Table 4.2	Steady state characteristics for L/D=1.0, Λ=1.0	76
Table 4.3	Geometry and operating conditions of GFB in Ruscitto et al. [97]	77
Table: 5.1	GFBs with simple foil structure model for L/D=1, S=1	104
Table: 5.2	GFBs with 1D foil structure model for L/D=1, S=1	105
Table: 5.3	GFBs with 2D CPT foil structure model for L/D=1, S=1	105
Table: 5.4	GFBs with 2D SDT foil structure model for L/D=1, S=1	105
Table 6.1	Variation of compliance coefficient (S) and material properties for different GFB geometries	108

NOMENCLATURE

C	Bearing radial clearance (m)
D	Diameter of journal (m)
e	Bearing eccentricity (m)
E_b	Young's modulus of bump foil (N/m^2)
E_t	Young's modulus of top foil (N/m^2)
F_X , F_Y	Vertical and horizontal components of hydrodynamic forces (N)
F_{X0} , F_{Y0}	vertical and horizontal steady state components of hydrodynamic forces (N)
F_ε, F_ϕ	Hydrodynamic forces in ε, ϕ coordinate system (N)
$\bar{F}_\varepsilon$, $\bar{F}_\phi$	Non-dimensional hydrodynamic forces in ε, ϕ coordinate system, $\bar{F}_\varepsilon = \frac{F_\varepsilon}{p_a R^2}$; $\bar{F}_\phi = \frac{F_\phi}{p_a R^2}$
G	Shear Modulus (N/m^2)
h	Film thickness (m)
h_o	Initial Bump height (m)
$h_{\min}$	Minimum film thickness (m)
H	Non-dimensional film thickness
$H_{\min}$	Non-dimensional minimum film thickness
i, j	Grid location in circumferential and axial directions of FDM mesh
K_f	Bump foil structural stiffness per unit area (N/m^2)
l_o	Half bump length (m)
l_s	Length of segment between the bumps (m)
L	Bearing length (m)
m	Number of divisions along j direction of FDM mesh

M	Mass of the rotor per bearing (Kg)
$\bar{M}$	Critical mass parameter
n	Number of divisions along i direction of FDM mesh
O	Center of bearing
O'	Center of journal
p	Hydrodynamic Pressure in gas film (N/m^2)
p_a	Atmospheric Pressure in gas film (N/m^2)
$\bar{p}$	Arithmetic mean pressure along bearing length (N/m^2)
P	Non-dimensional hydrodynamic pressure
$\bar{P}$	Non-dimensional arithmetic mean pressure along bearing length
R	Radius of journal (m)
s	Bump foil pitch (m)
S	Compliance coefficient/Number: $\frac{p_a}{CK_f}$
t	Time (s)
t_b	Bump foil thickness (m)
t_t	Top foil thickness (m)
w_t	Top foil transverse deflection (m)
W	Non-dimensional top foil transverse deflection
W_0	Steady state load carrying capacity (N)
$\overline{W}_X$, $\overline{W}_Y$	Non-dimensional vertical and horizontal steady state components of hydrodynamic forces: $\frac{F_{X0}}{p_a R^2}$; $\frac{F_{Y0}}{p_a R^2}$
$\overline{W}$	Non-dimensional steady state load carrying capacity
x, y, z	Coordinate system on the plane of bearing
Z	Non-dimensional axial coordinate of bearing: $\frac{z}{R}$

α	Compliance of the bump foil (m^3/N): $\frac{1}{K_f}$
ε	Eccentricity ratio
Λ	Bearing number: $\frac{6\mu\omega}{p_a}\left(\frac{R}{C}\right)^2$
μ	Gas viscosity ($N-s/m^2$)
ϕ	Attitude angle (rad)
θ	Angular coordinate of bearing (rad): $\frac{x}{R}$
θ_o	Half bump angle (rad)
υ	Poisson's ratio
τ	Non-dimensional time: ωt
ω	Rotor angular velocity (rad/s)
$\Delta\theta, \Delta Z$	Non-dimensional mesh size of FDM mesh

ABSTRACT

Gas foil bearings (GFBs) are compliant surfaces, self-acting hydrodynamic bearings typically constructed from several layers of sheet metal foils. These foils rest on elastic support structure and their performance largely depends on this support structure. A commonly used such foil structure consists of bump strips and the smooth foil rest on top of these strips.

The widespread usage of GFBs includes turbomachinery applications such as in turbo-generators, turbines, IC engines, compressors, pumps, light weight business aircraft engines etc. and a comprehensive numerical modelling verified with the available test data enables this usage.

This work sets out a structured and formal approach for the steady state analysis and the stability analysis of GFBs by mounting on a rotor bearing system. A literature review is carried out to assess the state of the art regarding both theoretical and experimental studies about GFBs. Based on the review, an attempt has been made to study several aspects of GFBs as mentioned hereunder in brief.

The compliant foil structure is modelled using the finite element method. Three different numerical models viz. One-dimensional (1D) beam element model, two-dimensional (2D) Classical Plate Theory (CPT) model and 2D Shear Deformation Theory (SDT) plate model were considered for modelling the compliant structure. The foil deflections calculated from the structural model using finite element analysis is coupled to the hydrodynamic gas film model governed by Reynolds equation to predict various characteristics of GFBs.

The steady state analysis of the GFBs are then carried out to predict various parameters such as load carrying capacity, effect of bump compliance coefficient etc. with different numerical models of the compliant foil structure.

Stability of the GFBs is also investigated using nonlinear time transient analysis with different numerical models of the foil structure by mounting the GFBs in a rotor bearing configuration. This study predicts the stability characteristics of the rotor motion, by tracing the journal centre trajectories at different locations of the rotor. The predicted results for each numerical model have been compared and an assessment of the models has been made to ascertain the best model for prediction. Also the conservative model is identified from the viewpoint of bearing designers.

The bump foil materials play a vital role in the load capacity performance of GFBs. Therefore, an attempt has also been made to explore the possibility of using different bump foil materials other than structural steel and the effect of compliance coefficient by estimating the load capacity performance of the GFBs.

Chapter 1

INTRODUCTION AND LITERATURE REVIEW

1.1. Introduction

Gas foil bearings (GFBs) are compliant surface, self-acting hydrodynamic bearings that use ambient gas as the working fluid. They are typically constructed from several layers of sheet metal foils from which they derive their name and do not require any external pressurization [1]. They supports the rotor by any combination of bending, membrane, or elastic foundation effects of the foil or thin shell. Two basic foil bearing configurations are shown in Fig. (1.1); firstly, the leaf type foil bearing (Fig. 1.1a) and secondly the elastically supported (bump type) foil bearing as shown in Fig. (1.1b).

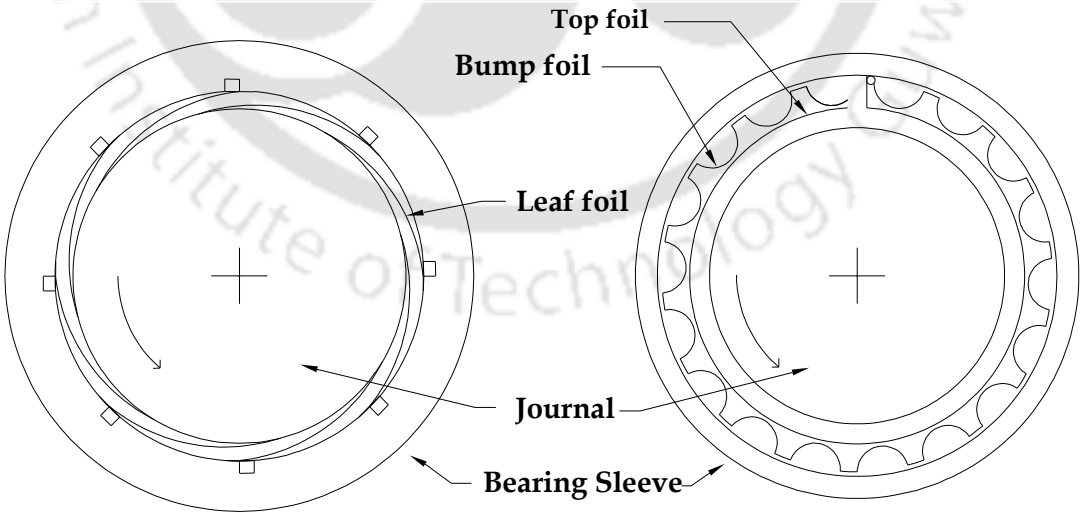

(a) Leaf type GFB **(b) Bump type GFB**

Fig. 1.1: Schematic views of two typical GFBs

The foil surface in the elastically supported foil bearing configuration resists deflection by means of the elastic foundation in back of the foil. The elastic foundation can be constructed from other structural shells, polymers, or springs. The foils in the leaf type bearing support load primarily by the resistance of the foils to bending [2]. Foil bearings are in widespread commercial use such as in Air Cycle Machines (ACM) which are employed to pressurize aircraft cabins, in turbo compressors, turbo expanders and in micro turbine generator systems.

Foil journal bearings are considered to be an alternative to rolling element bearings, and to rigid surface hydrostatic, hydrodynamic, or hybrid journal bearings for rotor support in turbomachinery applications such as rocket propulsion engines. In comparison to rolling element bearings and for operation with high surface speeds, both leaf type GFBs and bump type GFBs have demonstrated superior reliability in Air Cycle Machines (ACMs) of aircraft environmental control systems [3]. They offer compliance which can compensate for misalignment and deflection of rotors and machinery casings; reduces thermal distortion due to the thin shell structures of the bearing; and offers tolerance of dirt and debris in the lubricant flow and enhance the dynamic performance [2]. Since the 1960s, tension tape GFBs and multiple leaf GFBs with and without backing springs, as well as corrugated bump GFBs, have been implemented as low friction supports in oil-free rotating machinery.

Over the years, there has been subsequent development in the technology, design and performance of the gas foil bearings. The trends in its advancements can be generally grouped as the 1st generation gas foil bearings with axially and circumferentially uniform elastic support element, the 2nd generation gas foil bearings offering variable circumferential or axial compliance characteristics and the 3rd generation gas foil bearings with elastic support mechanism allowing both axial and circumferential tailoring of compliance [4]

1.1.1. Why foil bearings

Applications of air-lubricated foil bearing have been under extensive investigation by NASA Glenn research center by the name so-called as oil-free turbine engines. The implementation of this enabling technology is expected to result in a significant weight reduction of turbomachinery with lower maintenance requirements, by eliminating the conventional lubricant supply system with its associated piping arrangements. In addition, air is an environmentally friendly lubricant and is capable of accommodating operation at elevated temperatures compared to conventional oil lubricated bearings which fails because of oil viscosity that drops exponentially with increasing temperature. [5]

Some of the advantages of the foil bearings in turbo machinery applications are listed below [7]

- **Higher reliability:** Foil bearing machines are more reliable because

there are fewer parts necessary to support the relative assembly and there is no lubrication needed to feed the system. When the machine is in operation, the air/gas film between the bearing and the shaft protects the bearing foils from wear. The bearing surface is in contact with the shaft only when the machine starts and stops. During this time, a coating on the foils limits the wear.

- **No scheduled maintenance required**: Since there is no oil lubrication systems in machines that use foil bearings, there is never a need to check and replace the lubricant. This results in lower operating costs.
- **Soft failure:** Because of the low clearances and tolerances inherent in foil bearing design and assembly, if a bearing failure does occur, the bearing foils restrain the shaft assembly from excessive movement. As a result, the damage is most often confined to the bearings and shaft surfaces. The shaft may be used as is or can be repaired. Damage to the other hardware, if any, is minimal and repairable during overhaul.
- **High speed operation**: Compressor and turbine rotors have better aerodynamic efficiency at higher speeds. Foil bearings allow these machines to operate at higher speeds without any limitation as with ball bearings. In fact, due to the hydrodynamic action, they have a higher load capacity as the speed increases.
- **Low and high temperature capabilities**: Many oil lubricants cannot operate at very high temperatures without breaking down. At low

temperature, oil lubricants can become too viscous to operate effectively. Foil bearings, however, operate efficiently at severely high temperatures, as well as at cryogenic temperatures.

- **Process Fluid Operations**: Foil bearings have been operated in process fluids other than air such as helium, xenon, refrigerants, liquid oxygen and liquid nitrogen. For applications in vapour cycles, the refrigerant can be used to cool and support the foil bearings without the need for oil lubricants that can contaminate the system and reduce efficiency.
- **Cost saving**: The inherent simplicity of the foil bearing offers itself to rapid and easy fabrication. After an initial investment in tooling, foils can be stamped or rolled out at low cost. The greatest cost saving is realized by elimination of the oil network.

1.1.2. Foil bearing technology

The working principle of the foil bearing is based on the principle of air or gas bearing, and the primary load carrying function of the foil bearing is based on the principle of hydrodynamic pressure generation. As shown in Fig. (1.2), when two surfaces form a wedge, and one surface moves relative to the other surface, pressure is generated between the surfaces due to the hydrodynamic action of the fluid which carries load.

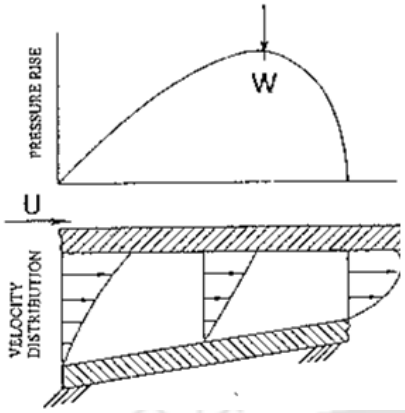

Fig. 1.2: Principle of an air bearing [7]

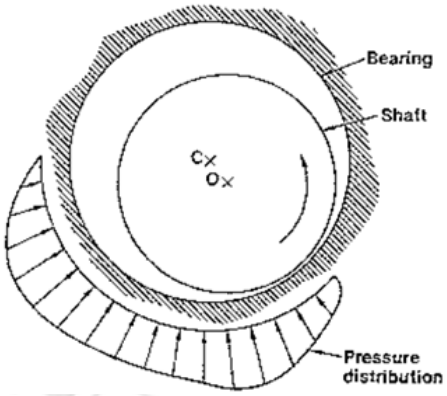

Fig. 1.3: Hydrodynamic pressure generation [7]

In a journal bearing, the shaft deflects and a wedge is formed due to the eccentricity between the shaft center and the bearing center. The resulting hydrodynamic pressure generation is shown in Fig. (1.3)

Even though, the principle of an air bearing is simple, yet the application is complex. Usually running radial clearance between the shaft and the bearing is less than 0.0005 inch for a 2 inch diameter shaft running at 36,000 rpm. But the shaft growth due to temperature and centrifugal force could be 0.0020 in [7]. Hence a bearing cannot be made to work at various speeds and temperatures. In addition, damping is required to suppress any whirl instability, and there could be misalignment between various rotating parts and stationary parts. Some of these problems are resolved by using the foil bearings technology. The operating principles comparison of a liquid-lubricated journal bearing and a gas foil journal bearing is shown in Fig. (1.4). While stationary, there is a small amount of preload between the shaft and the

bearing. As the shaft turns, the hydrodynamic pressure is generated, which pushes the foils away from the shaft and the shaft becomes completely airborne. This phenomenon occurs instantly during start-up at a very low speed. When the shaft is airborne, friction loss due to shaft rotation is very small. As the shaft grows, the foils get pushed further away keeping the film clearance relatively constant. In addition, foils provide coulomb damping due to relative sliding, which is essential for stability of the machine [8].

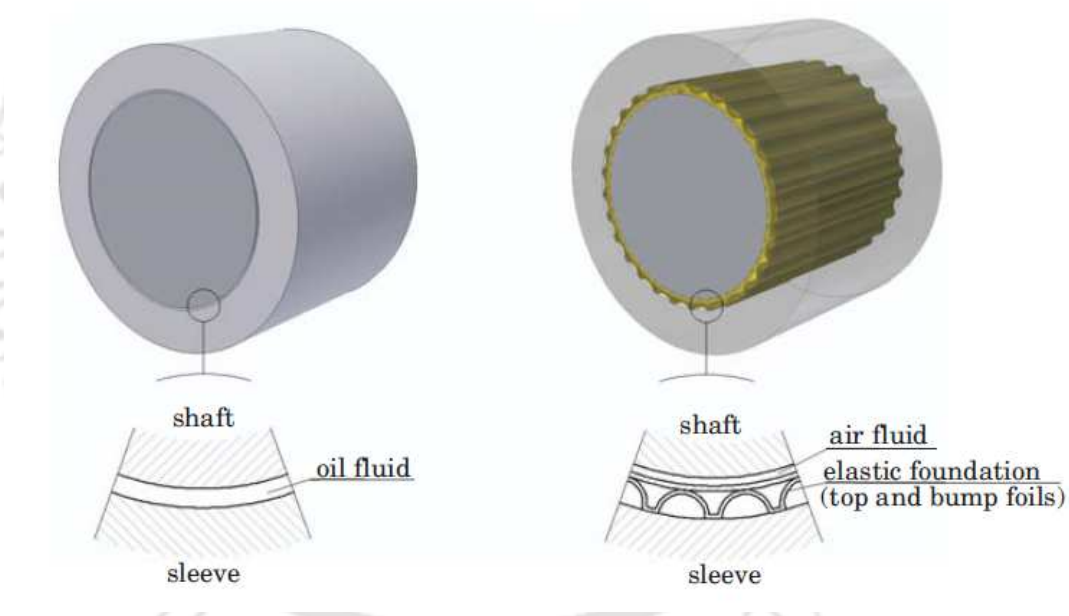

Fig. 1.4: Comparison of operating principles of a liquid-lubricated journal bearing and a gas foil journal bearing [8]

1.2. State of The Art

Gas foil bearing (GFB) technology has made significant progress over the last 40 years and fulfils most of the requirements of a novel oil-free turbo-machinery by increasing tenfold their reliability in comparison to rolling

elements bearings [2, 7]. Some of the several advantages of the foil bearing over the conventional rigid surface bearing or ball bearing, includes high speed operation, low and high temperature capabilities, lower power loss and better stability. These advantageous characteristics of foil bearings have been demonstrated through many experimental investigations [9-11,]

The rotor-bearing systems are one the of most common and essential machine parts used in many industrial machines such as turbo-generators, steam and gas turbines, IC engines, compressors, pumps, computer disk storages etc. Their performance is of utmost importance in modern industrial world due to the ever increasing need of power, higher speeds and number of complicated accessories attached with the rotor. The rotors are made light weight and required to run much above the critical speed. In view of this, study of static and dynamics characteristics of the rotor-bearing systems is essential in designing rotating equipments requiring in-depth rotor-dynamic modelling.

Rotor-bearing systems are subjected to unstable motions which if not addressed correctly may lead to catastrophic failures. Instabilities in rotor-bearing systems may arise due to a number of reasons such as fluid film bearings, shaft stiffness asymmetry, internal friction between mating components and aerodynamic forces [12]. The rotors exhibit high amplitude of vibration at critical speed due to the residual unbalance and also because of the presence of the different attachments to the rotor. Hence, the rotor centre of mass does not always coincide with the geometric centre. An external force

acts on the rotor because of this eccentricity of the unbalance mass, and the unbalance response becomes maximum when the shaft speed reaches the fundamental natural frequency.

Gas foil bearings (GFBs) which have been successfully used in various types of rotating machinery, such as turbochargers, auxiliary power units, and gas turbine engines, which offers compliant surface to rotor bearing system providing bearing structural stiffness. The underlying compliant structures provides a tenable structural stiffness source [13, 14] resulting in a larger film thickness than the rigid wall bearings [15, 16] enabling high-speed operation and larger load capacity including tolerance for shaft misalignment [7]. Also damping of coulomb type arises due to the relative motion between the bumps and the top foil, and between the bumps and the bearing wall [17].

1.3. Literature Review

1.3.1. Overview

In 1953, Blok and Van Rossum have introduced the concept of foil bearings (FBs). The authors have pointed out that a foil bearing film thickness, larger than that of rigid gas bearings, could improve operational reliability and provide a solution for problems related to thermal expansion of both a journal and its bearing [3]. Field experience has proved, since the late 1960's, that Gas Foil Bearings (GFBs) are far more reliable than ball bearings previously used in Air Cycle Machines (ACMs) installed in aircrafts.

Therefore, GFBs have since been used in almost every new ACM installed in both civil and military aircraft [7]. Implementation of GFBs into high performance turbo machinery applications demands accuracy in modelling capabilities. This literature review discusses previously published works regarding GFBs models and relevant experimental tests

1.3.2. Theoretical GFB models and predictions

Juan and Connolly [18] have developed a model based on auxiliary dependent variables incorporating the compressibility and slip flow. They have obtained the governing motion equation by finite element discretization and used the mixed interpolation method. The hydrodynamic theory of foil bearings has been reviewed by Tadjbaksh and Ahmadi [19]. He has included the relationship between fluid pressure and film thickness and the compressibility of gas in the analysis and has developed a simple numerical scheme for solution of the nonlinear boundary value problem.

An integrated procedure which analyses the dynamics of a foil bearing on elastic supports, have been presented by Braun et al. [20]. They have illustrated the formulation of complete time dependent Navier-Stokes equations and have presented the simulation of finite element (FE) model for elastic deformation of the foil and its supports.

Peng [21] has developed a mathematical model and a numerical scheme for simulating the hydrodynamic pressure and temperature rise of compliant foil.

He has presented a series of parametric study to illustrate the utility of the developed algorithms for characterization of foil bearing performance using both isothermal and thermo hydrodynamic theories. Peng and Khonsari [22] have presented a thermo hydrodynamic analysis capable of predicting the thermal performance of foil bearings.

A simple physical model for gas foil bearings with a double bump strip layer have been developed by Kim and Andre´s [23]. They coupled the Reynolds equation for the thin film flow of an ideal gas to the elastic supports deflections and have predicted that the gas foil bearing with a two bump strip layer enhances the bearing direct damping force coefficients. They also demonstrated that foil bearings have greatly different static and dynamic force characteristics [24]. A complex finite element (FE) model coupling the elastic deformations of the top foil to the bump deflections have also been presented in [25], where in they predicted the stiffness and damping coefficients versus excitation frequency, journal attitude angle and minimum film thickness for increasing static loads. Furthermore, in [26] they have developed and analyzed the thermohydrodynamic (THD) model for prediction of gas foil bearing (GFB) performance.

Iordanoff et al. [27] have described a non-linear model, coupling a simplified equation of the rotor motion for both Reynolds equation and foil assembly model. They have outlined the possibility to optimize the friction between the foils in order to improvise the dynamic behaviour of foil bearings

Park et al. [28] have analyzed the characteristics of the air foil thrust bearing. They have identified the stiffness and damping of the bump foil under the condition of various bump parameters as well as the load carrying capacity and bearing torque at the tilting state and the bearing performance. The performance parameters of load capacity and power loss has been analysed and tested through a new design for oil-free journal bearings by Knowels [29] He has used the numerical algorithms to predict the performance of the foil bearings.

The effect of foil local deflection have been investigated by Feng and Kaneko [30]. They have developed a finite difference computer program to solve the Reynolds equation and the elastic deflection equations. The perturbation techniques have been used to determine the dynamic coefficients. Lee et al. [31] have developed a static structural model of the foil journal bearing considering the hysteretic behaviour of the friction between bumps and their mating surfaces. Nalepa et al. [8] have overviewed the bearing technology with deformable elements which utilizes bearing sleeve. They have distinguished three foil bearing generations which differ in the structure and properties with regard to load capacity, stiffness and undesirable variation damping. They have incorporated the technical solutions of the foil journal and the thrust bearings.

A numerical model with protuberant foil structure have been developed Yu et al. [32]. They have applied the perturbation method to linearize the Reynolds

equation and analyzed the effects of eccentricity ratio, bearing number, and number of protuberances on the characteristics of bearings. Yang et al. [33] have calculated the dynamic stiffness and damping coefficients of tilting pad gas bearings by the partial derivative method. They have presented two computational models for the stability analysis on rotor systems supported by tilting pad gas bearings which has impacted on perfecting the stability analysis method of rotor systems supported by gas bearings.

Lez et al. [34] have presented a static structural model considering the structure as multi degrees of freedom. They also have validated the model by FE simulations and experimental tests data. Besides they have investigated the behaviours of the bump type foil bearing structure under static and dynamic loads [35]. An analysis of a gas lubricated multi-leaf journal bearing. Have been presented by Reddy et al. [36]. They have solved the two dimensional (2D) compressible Reynolds equation and coupled the elastic deformation equation with the Reynolds equation to get the foil deflections and change in film thickness. The incremental finite element method and Newton Raphson iterative procedure have been used to formulate the problem and to investigate the static performance parameters and dynamic characteristics.

A novel design feature of Hybrid Air Foil Thrust Bearings [HAFTB] with radially arranged bump foils have been presented by Lee and Kim [37]. They performed the Rayleigh step contour and have investigated the simulated

static and dynamic characteristics of the HAFTB. The possibilities to predict the foil bearings performance potential based on its design have been assessed by DellaCorte and Valco [38] through an introduction of a simple ROT (Rule of thumb) method for foil air Journal bearings.

Howard and DellaCorte [39] have investigated the rotor dynamic analysis to assess the viability of foil bearing supported turbo alternator. They discussed briefly the technological background, various assumptions made and analysed the rotor dynamic behaviour, which eventually concludes that a foil bearing supported turbo alternator is possible. However, there is still more work needed to gain knowledge about foil bearing behaviour in helium-xenon gas.

The design and manufacturing processes of mesoscale foil gas bearings which are applicable for the micro turbo machinery have been introduced by Kim et al. [40]. They have demonstrated and predicted the performances of the foil through a nonlinear orbit simulations. Radil and DellaCorte [41] have presented the concept of a 3-D power loss performance map of the foil bearing as a function of speed and load. The technological history, primary physics, engineering practicalities, and existing experimental and experimental database for scaling foil bearings have been reviewed by DellaCorte and Bruckner [42]. They have identified some of the major remaining technical challenges.

1.3.3. Structural characteristics

Song and Kim [43] have constructed, analysed, and tested a new foil gas bearing with spring bumps. The load capacity, structural stiffness, and equivalent viscous damping (and structural loss factor) have been measured to demonstrate the feasibility of the new foil bearing. The stiffness and damping of radial air-foil bearings in the light of experimental results have been presented by Arora et al. [44]. They have proposed an experimental setup which uses single air-foil bearing instead of standard two-foil bearing setups. The results indicate that the developed experimental procedure is able to identify the stiffness and damping properties of radial air-foil bearings accurately.

San Andrés et al. [45] have presented a hollow shaft, warmed by an electric heater which holds a floating second generation FB loaded dynamically by an electromagnetic shaker. The dynamic load, structural stiffness, FB deflection and bearing energy dissipation have been measured. Rubio and San Andrés [46] have investigated the structural stiffness, dry friction coefficient, and equivalent viscous damping in a bump-type foil gas bearing. The structural force coefficients in a bump-type foil bearing for oil-free turbomachinery have been experimentally identified by Breedlove [47]. He determined the static and dynamic bearing parameters for increasing shaft temperature.

A new test rig to measure load capacity of the bearing at higher speeds have

been designed and constructed by Kim et al. [48]. They have conducted experiments to estimate the structural stiffness of a test gas foil bearing for increasing shaft temperatures and have analyzed the stiffness, damping, and dry friction. Kumar and Kim [49] have investigated the experimental results on load capacity of a new hydrostatic air foil bearing made of corrugated bump foils.

A multifunctional test rig has been built by Yang et al. [50]. They have described an experimental method to identify the static and dynamic performance of compliant foil air bearing. Dickman [51] has manufactured three identical open source foil gas thrust bearings. He has tested the bearings for load capacity, bearing torque and its characteristics. Lee et al. [52] have investigated the static and dynamic characteristics of the bump foil bearing considering the top foil bending effect correlation among bumps numerically as well as experimentally.

Kim and Lee [53] have reported the design and preliminary test results of a hydrodynamically preloaded three-pad Hybrid Air Foil Bearing [HAFB] aimed for midsized airborne turbomachinery applications. They have combined the hydrodynamic pressure with hydrostatic lift to investigate the load carrying capacity of the hydrostatic operation at zero running speed. Radil et al. [54] has also shown how variations in the radial clearance effect the load capacity coefficient of the foil air bearings.

A new foil bearing known as Visco Elastic Foil Bearing (VEFB) has been proposed by Lee et al. [55]. They have examined the structural dynamic characteristics of the conventional bump foil bearing and the flexible rotor system supported by a viscoelastic foil bearing (VEFB).

San Andre´s and Kim [56] have modelled a Foil Bearing as a third order structural element with nonlinear stiffness which was derived from the measurements. They have predicted the performance of a rigid rotor supported on bump-type foil bearings and compared to rotor response measurements. San Andre´s et al. [57] have presented the test data and analytical results of a test rotor and GFB system operating at very high temperature. Kim and San Andre´s [58] have investigated the rotor dynamic response measurements on a rigid rotor supported on gas foil bearings. The experimental results of the rotordynamic performance of a small rotor supported on two bump-type gas foil bearings have been presented by San Andre´s et al. [59]. They recorded the coast down rotor responses from 25 krpm to rest for various imbalance conditions and increasing air feed pressures. They observed that rotor imbalance exacerbates the severity of subsynchronous motions, denoting a forced nonlinearity in the GFBs and gas pressurization through the bearings' side improves rotor subsynchronous motions and reduces the peak amplitudes at the critical speed. They also noticed wear spots on the top foils and rotor surface through post-test inspection.

A preliminary experimental investigation of the misalignment tolerance of gas foil journal bearing systems has been presented by Howard [60]. Through the study it has been indicated that the dynamic response of the rotor misalignment may affect the force coefficients of gas foil bearing. The effect of side end pressurization of the gas foil bearing and predicted that the side end pressurization delays the threshold speed of instability has been presented by Kim [3]. He also has conducted the dynamic response measurements on a rigid rotor supported on GFBs. San Andrés and Ryu [61] have presented the measurements of the rotordynamic response of a rigid rotor supported on flexure pivot tilting pad hybrid gas bearings. They have performed tests for various imbalances, increasing supply pressures, and under load on-pad and the load-between-pad configurations.

Shetty [62] has performed the Hydrodynamic and hydrostatic conditions tests using a custom made test rig and has compared the imbalance response simulations of a four degree of freedom rigid rotor support by hybrid three pad air foil bearing with the empirical results. An analysis and experimental validation of a hybrid gas bearing with static and dynamic force characteristics desirable for high-speed turbomachinery has been presented San Andrés [63]. He developed a computational model including the effects of external pressurization and predicts the rotordynamic coefficients of the test bearings.

Kaneko et al. [64] have presented the design and manufacturing process of

radial foil bearing for the rotor diverted from a commercially available turbocharger. Kim and Park [65] have developed a simple analytical model for prediction of top foil deflection and sagging effects under hybrid (both hydrostatic and hydrodynamic) mode. The time-domain orbit simulations have been utilized to predict imbalance responses of a rigid rotor supported by Hydrostatic Air Foil Bearing (HAFBs). Osborne and San Andre´s, [66] have investigated the rotordynamic performance of a small rotor supported on simple and inexpensive hybrid gas bearings. Bou-Saïd et al. [67] have presented a nonlinear time dependent calculation used for the dynamic simulation of a rotor mounted with aerodynamic (gas) bearings.

1.3.4. Thermal predictions, high speed and high temperature operations

Heshmat et al. [68] has presented the results on development of an advanced coating system used with compliant foil bearings that permits higher operating speeds and at high temperatures. They have designed a foil journal bearing with a composite coating consisting of korolon applied to the bearing top foil and a dense chrome coating to the journal surface. The foil bearing and journal have been installed in a 240-lb thrust turbojet engine and operated successfully. Sadashiva [69] has developed a new modified test rig AFB capability to measure bearing torque during start-up, shut-down and high speed operation. The design, modifications, fabrication and experimental investigation of thermal behaviour of the AFB has been presented. He has

computed the critical speeds, mode shapes and un-damped critical speed maps by lateral vibration analysis of the shaft. Dykas and Tellier [70] evaluated the performance and durability of a simulated machine's lifetime, subjecting the bearing and thrust runner to high temperature repeated start/stop cycles. Radil and Zeszotek [71] have performed tests to determine the internal temp profile in a compliant foiled air bearing under various speed and load conditions. They have determined the heat generation responsible for and the area of maximum temperature.

Feng and Kaneko [72] have solved the Reynolds equation with gas viscosity as a function of temperature and presented a 3D temperature prediction of air film. They have utilized the Lobatto point quadrature to accelerate the iteration process and have made a comparison of thermo hydrodynamic to isothermal results to emphasize the importance of thermal effects. San Andrés and Kim [73] have presented a thermo hydrodynamic model predictions and performance measurements of a bump-type foil bearing for oil-free turbo shaft engines in rotorcraft propulsion systems. Lee et al. [74] have presented a transient 3D thermo hydrodynamic (3D THD) model of radial foil bearings. They have predicted the transient thermal behaviour of the bearing-rotor system and verified through extensive experimental measurements of the transient thermal behaviour of three-pad foil bearing for various cooling air pressures, external loads, and speeds.

Kim and San Andrés [75] presented a simple analysis to estimate the limiting

journal eccentricity, minimum film thickness, and stiffness of a gas foil bearing operating at infinite high shaft speed. Bauman [76] has presented a new test apparatus capable of testing thrust foil air bearings up to 100 mm in diameter at the speed of 80,000 rpm and a temperature up to 650 °C. He has measured the bearing torque, load capacity, and bearing temperatures. The test rig seems to be a valuable tool for thrust foil bearing research, parametric studies, and technology development. Salehi et al. [77] have tested a small mesoscopic gas turbine engine (MGTE) simulator at speeds over 700,000 rpm. They have operated the MGTE with specially designed miniature compliant foil journal and thrust air bearings. They have carried out an analysis of the results of the rotor bearing system dynamics along with experimentally measured natural frequencies at many operating speeds. The design and test results of an ultra-high speed tape type radial foil bearing for turbo machinery have been described by Hikichi et al. [78]. The bearing performance has showed no significant deterioration after 300 start-and-stop cycles. They have achieved the highest DN product ('D' rotor diameter in mm and 'N' is rotation speed in rpm.) at maximum rotation speed of 642,000 rpm.

Zhou et al. [79] have presented the test results of a gas thrust bearing (compliant foil bearings, with top thin metal foil and a bottom thin rubber foil.) with viscoelastic support designed for high speed turbomachinery. They have conducted the static and stability experiments on a high speed gas turbine test rig. Vleugels et al. [80] have discussed a test set-up to validate the

numerical models of high-speed foil bearings for microscopic gas turbines. They have conceivably measured the load characteristics of a bearing in a very accurate way based on a 3-bearing configuration. Xiong et al. [81] have designed a small high speed cryogenic turbo-expander. They studied the effect of foil stiffness on the vibration performance of the bearings.

1.3.5. Distinct applications and operations

Creary [82] has explored the miniaturization of gas foil bearings for palm-sized turbomachinery using silicon parts. He has suggested an alternative microfabrication technique called LIGA (German acronym meaning Lithography, Electroplating, and Molding) and has investigated the predicted performance of the bearing through orbit simulation method. A methodology for the design and construction of a simple foil thrust bearings have been proposed by Dykas et al. [83] for parametric performance testing for microturbomachinery applications and for low marginal costs. They have demonstrated the tests for bearing load capacity. Radil and DellaCorte [84] have investigated the foil bearing starting considerations and requirements for rotorcraft engine applications and have indicated that a polymer-coated foil bearing can tolerate the sliding conditions that would occur during the conventional start-up at room temperature.

The use of gas foil bearing technology for use in Closed Brayton Cycle (CBC) power turbines for future space electric power generation have been investigated by Howard et al. [85]. They have developed a model and they

observed and reported the effects of very high ambient pressure, startup torque, and misalignment. Dykas [86] has explored experimentally the operating characteristics of foil gas thrust bearings for oil- free turbomachinery applications and have analytically ascertained the physical mechanisms that limit bearing performance. He also have quantified the effects of non-ideal surface conditions on the load capacity of foil thrust bearings.

Two kinds of new compliant foil journal bearing for a small cryogenic turbo-expander have been presented by Hou et al. [87]. And based on the performance of the same experimental set-up, they have observed that the foil bearing supported with elastic material have more stability than the one supported with copper wires. Koepsel [88] have extended and demonstrated the state-of- the-art of gas lubricated compliant surface bearings for advanced turbomachines. The gas-lubricated foil bearings utilized for this program are of a design patented by the Garrett Corporation, the bearings initially developed for experimental use in cooling turbines of the Boeing 727 air conditioning system.

An experimental study have been conducted by Bruckner [89] which helps in obtaining the direct torque measurements on gas foil bearings and the generator rotor stator gaps of high speed generators. He has investigated a non-dimensional analysis to extend the experimental results into the closed supercritical cycle (CSC) range for the generator windage. Hashimoto [90] has

presented a new type of hybrid porous foil bearings for web handling. The traveling web is supported by the externally pressurized porous foil bearings with the hybrid effects of hydrodynamic pressure. He has illuminated experimentally the hybrid effects of porous foil bearing on the web spacing height characteristics.

1.4. Objectives of the Present Work

From the foregoing literature review, it has been observed that the elastic support structure of the gas foil bearings (GFBs) has been modelled in various ways. Experimental as well as theoretical investigations of GFBs have been carried out to assess the performance of the bearing at different operating conditions. However, different foil structure models have not been compared as to ascertain which model should be considered for prediction of steady-state as well as dynamic performances of GFBs.

In view of the above, the simple elastic foundation model (simple model) is extended to account for and integrate with the elastic deformation of the top foil. Four different numerical foil structure have been modelled, namely, the simple model, a 1D (one dimensional) beam element model, two 2D (two dimensional) classical plate theory (CPT) model and 2D (two dimensional) shear deformation plate theory (SDT) model respectively. The steady state characteristics of the GFBs with different numerical foil structure model have been investigated.

An attempt has also been made to study the stability characteristics of a rigid

rotor mounted on two symmetrical gas foil bearings. A theoretical analysis using a non-linear time transient method has been carried out for stability analysis. The stability maps have been plotted by observing the trajectories of the journal centre for different rotor-bearing parameters.

Further, it is noteworthy to observe that over the years the foils used in GFBs are mostly structural steel, which is mainly because of its favourable characteristics. Structural steel has been substituted by other materials including composites in different utilities in recent times. In view of this fact, it is felt pertinent to explore the possibilities of substituting the foil material. Therefore, an attempt has been made at exploring the possibility of using a suitable alternative material for the foil. It has been observed that the load capacity of the GFBs is greatly enhanced by using a fibre reinforced polymer (FRP) composite as the bump foil materials. Further, an attempt has also been made to see the effects of compliance coefficients and its influence on the static load performance of the GFBs.

The following theoretical analyses are carried out to achieve the foresaid objectives.

1. Numerical modelling of the compliant foil structure by incorporating finite element model of the top foil, namely 1D beam model, 2D classical plate theory (CST) model and 2D shear deformation plate theory (SDT) model.
2. Derivation of the discretised Reynolds equation as a non-linear matrix

equation.

3. Steady state characteristics analysis of the gas foil bearing with different numerical foil structure models
4. Nonlinear time transient stability analysis of the GFBs by mounting the GFBs in a rotor bearing configuration to ascertained the stability characteristics of the rotor motion.
5. Load capacity analysis of the gas foil bearing with different bump foil materials.

1.5. Organization of the Thesis

The present thesis is broadly divided into seven chapters. Chapter 1 deals with the introduction, state of the art, some relevant literature review and the objectives of the present work. GFBs description, mathematical formulation of basic governing equations, the equations of motion of rigid rotor supported on symmetrical gas foil journal bearings and the solution methodology are presented in chapter 2. A non-dimensional form of the governing equation and the equation of motion is also presented in this chapter. Chapter 3 describes the detail formulation of different numerical foil structure models of the GFBs. Analysis of the steady state characteristics of the GFBs with different foil structure models are detailed in chapter 4. The stability analysis of a fully-balanced rigid rotor supported on two symmetrical GFBs using a non-linear transient method is presented in chapter 5. Chapter 6 explores

different bump foil materials of the GFBs and its effect on GFBs load performance. Finally, the major inferences drawn from the work carried out in this thesis are produced in chapter 7 along with the scope of future work.

Chapter 2

BASIC EQUATIONS AND DESCRIPTION OF GAS FOIL BEARINGS (GFBs)

2.1. Introduction

This chapter deals with the general description of the bump type gas foil bearing and the basic governing equations of the gas foil bearing. The mathematical formulation of the equation of motion of rigid rotor supported on two symmetrical gas journal bearings has been presented. The non-dimensional form of the governing equations and the equation of motion derived for the study of nonlinear stability analysis are also presented in this chapter. Furthermore, the methodology and the solution algorithm have been detailed in the form of flowchart.

2.2. Description of Bump Type Gas Foil Bearing (GFB)

Figure (2.1) shows the configuration of a typical bump type GFB. The GFB consists of a thin (top) foil and a series of corrugated bump strip which supports (bump foil) the rotor. The leading edge of the thin foil is kept free, and the foil trailing edge is welded to the bearing housing. A bump structure is laid on the inner surface of the bearing beneath the top foil. The top foil of smooth surface is supported by a series of bumps acting as springs, thus making

the bearing compliant. The presence of bump strip offers a tenable structural stiffness [13, 14].

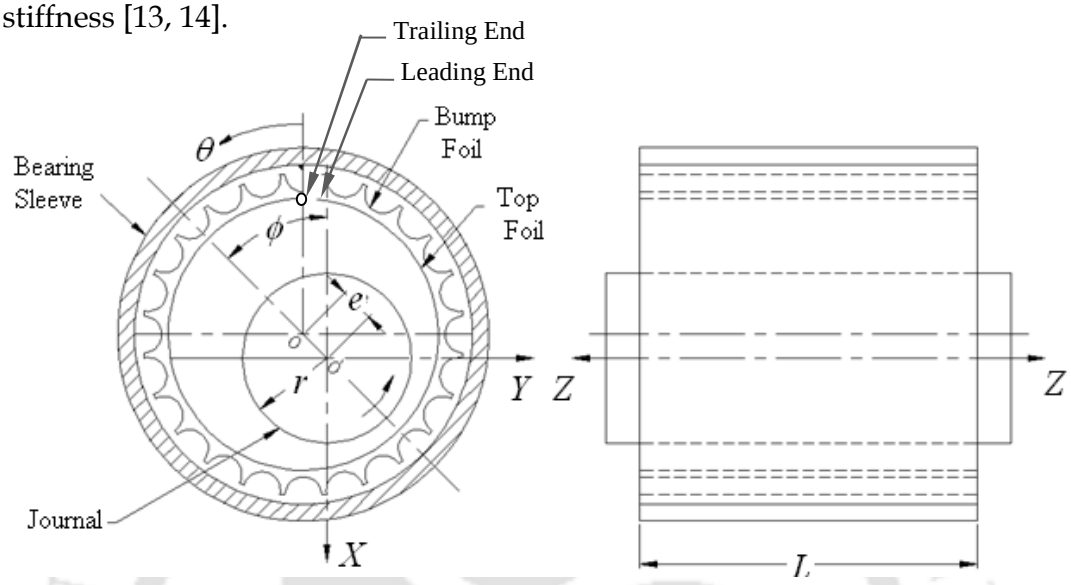

Fig. 2.1: Schematic view of a bump type GFB

The bump foil layer gives the bearing flexibility that allows it to tolerate significant amount of misalignment, and distortion that would otherwise cause a rigid bearing to fail. In addition, micro-sliding between the top foil and bump foil and the bump foil and the housing generates coulomb damping which can increase the dynamic stability of the rotor-bearing system [17]. During normal operation of GFB supported machine, the rotation of the rotor generates a pressurized gas film that pushes the top foil out in radial direction and separates the top foil from the surface of the rotating shaft. The pressure in the gas film is proportional to the relative surface velocity between the rotor and the GFB top foil. Thus, the faster the rotor rotates, the higher the pressure, and the more load the bearing can support. When the

rotor first begins to rotate, the top foil and the rotor surface are in contact until the speed increases to a point where the pressure in the gas film is sufficient to push the top foil away from the rotor and support its weight. Likewise, when the rotor slows down to a point where the speed is insufficient to support the rotor weight, the top foil and rotor again comes in contact. Hence solid lubricant coating were used to mimimize wear and friction, either on the shaft surface or the foil during startup and shut down [2].

2.3. Basic Governing Equations

The schematic view of a bump type gas foil bearing has been shown in Fig (2.1). The Reynolds equation describes the generation of the gas pressure (p) within the film thickness (h) and for an isothermal, isoviscous ideal gas this equation is,

$$\frac{\partial}{\partial x}\left(ph^3 \frac{\partial p}{\partial x}\right)+\frac{\partial}{\partial z}\left(ph^3 \frac{\partial p}{\partial z}\right)=6\mu\omega R\frac{\partial (ph)}{\partial x}+12\mu\frac{\partial (ph)}{\partial t} \tag{2.1}$$

where, (x, z) are the circumferential and axial coordinates on the plane of bearing, . The pressure takes ambient value p_a on the side boundaries of the bearing.

The boundary conditions for the solution of Eqn. (2.1) are

$$p = p_a \quad at \quad \theta=0 \text{ and } 2\pi$$

$$p = p_a \quad at \quad z=0 \text{ and } L \tag{2.2}$$

The film thickness (h) for a perfectly aligned journal configuration is given by

$$h = C + e\cos(\theta - \phi) + w_t \tag{2.3}$$

where, C, e and w_t are the assembled clearance, journal eccentricity and the elastic deformation of the foil structure respectively.

Therefore, Eqn. (2.1) and Eqn. (2.3) are coupled through the hydrodynamic pressure and elastic deformation of the foil structure as a function of the hydrodynamic pressure.

The above governing equations can be normalized by using the following substitutions as follows:

$$S = \alpha p_a / C \qquad \alpha = 1/K_f \qquad H = h/C \qquad z = Z/R \qquad \frac{x}{R} = \theta$$
$$y = Y/L \qquad P = \bar{p}/p_a \qquad \varepsilon = e/C \qquad W = w_t/C \qquad t = \frac{\tau}{\omega} \tag{2.4}$$

Hence, the non-dimensional Reynolds equation as given in Eqn. (2.1) is given by

$$\frac{\partial}{\partial\theta}\left(PH^3\frac{\partial P}{\partial\theta}\right) + \frac{\partial}{\partial Z}\left(PH^3\frac{\partial P}{\partial Z}\right) = \Lambda\frac{\partial PH}{\partial\theta} + 2\Lambda\frac{\partial(PH)}{\partial\tau} \tag{2.5}$$

where $\Lambda = \left(6\mu\omega/p_a\right)\left(R/C\right)^2$

For steady state condition, Eqn. (2.5) reduces to

$$\frac{\partial}{\partial\theta}\left(PH^3\frac{\partial P}{\partial\theta}\right) + \frac{\partial}{\partial Z}\left(PH^3\frac{\partial P}{\partial Z}\right) = \Lambda\frac{\partial PH}{\partial\theta} \tag{2.6}$$

And similarly the non-dimensional film thickness is given as,

$$H = 1 + \varepsilon \cos(\theta - \phi) + W \tag{2.7}$$

where, ε is the eccentricity ratio and W non dimensional foil deflection.

2.4. Steady State Formulation of Reynolds Equation

The non-dimensionalized steady state Reynolds Eqn. (2.6) has been discretized using a finite difference approach. For all the derivatives present in Eqn. (2.6) the central difference formula have been used. Figure (2.2) shows an exfoliated view of a bearing showing the mesh size $(\Delta\theta \times \Delta Z)$, m and n are the divisions along θ and Z respectively. The dimension of the pressure in the domain in matrix form will be $(m+1)\times(n+1)$ represent by $\mathbf{P}$. The vector representation of $\mathbf{P}$ is p and its length is $(m+1)(n+1)$. Similarly foil deflection and film thickness in matrix forms are represented by **W** and **H** respectively. If *(i, j)* is any arbitrary point in the matrix representation, its position in the vector representation can be written as $q = (j-1)(m+1)+i$. The four adjacent nodes associated with node *(i, j)* are $(i+1, j)$, $(i-1, j)$, $(i, j+1)$ and $(i, j-1)$ as shown in Fig. (2.2). The discretized form of Eqn. (2.6) for *(i, j)*th node or q^{th} node can be written in a quadratic form as

$$\left(\mathbf{p}_q^e\right)^T \mathbf{A}_q^e \mathbf{p}_q^e + \mathbf{b}_q^e \mathbf{p}_q^e = \mathbf{0} \tag{2.8}$$

where, $\mathbf{p}_q^e = \left\{P_{(i,j-1)} \quad P_{(i-1,j)} \quad P_{(i,j)} \quad P_{(i+1,j)} \quad P_{(i,j+1)}\right\}^T$ and its size is 5×1,

$$\mathbf{A}_q^e = \begin{bmatrix} \frac{H^3_{(i,j-1)}}{4(\Delta Z)^2} & 0 & 0 & 0 & -\frac{H^3_{(i,j-1)}}{4(\Delta Z)^2} \\ 0 & \frac{H^3_{(i-1,j)}}{4(\Delta\theta)^2} & 0 & -\frac{H^3_{(i-1,j)}}{4(\Delta\theta)^2} & 0 \\ \frac{H^3_{(i,j)}}{(\Delta Z)^2} & \frac{H^3_{(i,j)}}{(\Delta\theta)^2} & -\frac{2H^3_{(i,j)}}{(\Delta\theta)^2}-\frac{2H^3_{(i,j)}}{(\Delta Z)^2} & \frac{H^3_{(i,j)}}{(\Delta\theta)^2} & \frac{H^3_{(i,j)}}{(\Delta Z)^2} \\ 0 & -\frac{H^3_{(i+1,j)}}{4(\Delta\theta)^2} & 0 & \frac{H^3_{(i+1,j)}}{4(\Delta\theta)^2} & 0 \\ -\frac{H^3_{(i,j+1)}}{4(\Delta Z)^2} & 0 & 0 & 0 & \frac{H^3_{(i,j+1)}}{4(\Delta Z)^2} \end{bmatrix}$$

$\mathbf{A}_q^e$ is a 5×5 non-symmetric matrix;

$\mathbf{b}_q^e = \begin{bmatrix} 0 & \frac{\Lambda H_{(i-1,j)}}{2(\Delta\theta)} & 0 & -\frac{\Lambda H_{(i+1,j)}}{2(\Delta\theta)} & 0 \end{bmatrix}$ is a row vector of size 1×5.

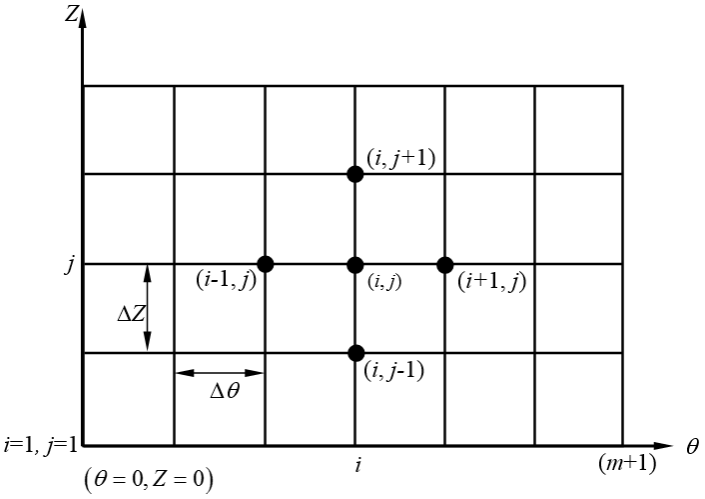

Fig. 2.2: An exfoliated view of a bearing showing the mesh size

The force of the gas film acting on the journal can be computed by integrating the pressure over the bearing surface. According to the coordinate system illustrated in Fig. (2.3), this integration can be written as:

$$\bar{W}_X = -\int_{-L/D}^{L/D}\int_{0}^{2\pi} P\cos\theta d\theta dZ$$

$$\bar{W}_Y = \int_{-L/D}^{L/D}\int_{0}^{2\pi} P\sin\theta d\theta dZ \qquad (2.9)$$

For numerical integration, Simpson's one third rule has been used.

Finally the total non-dimensional load is given by

$$\bar{W} = \sqrt{\bar{W}_X{}^2 + \bar{W}_Y{}^2} \qquad (2.10)$$

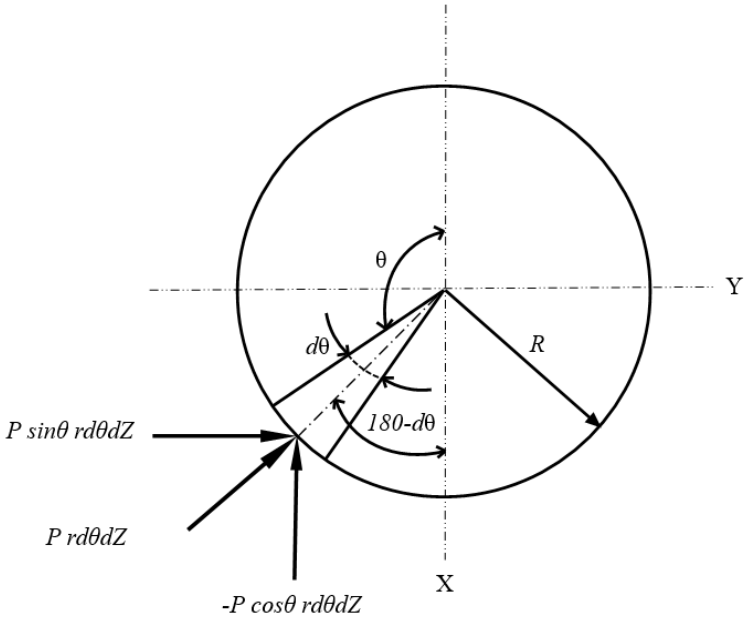

Fig. 2.3: The coordinate system and the sign convention of the journal forces

2.4.1. Solution Method

In the present algorithm, a fixed coordinate system has been considered (X and Y). Therefore, for steady state equilibrium, the horizontal load

component should become zero. The flowchart of the solution process is shown in Fig. (2.4). For a given eccentricity ratio, the attitude angle is varied till the horizontal load component approximately becomes zero. Bisection method has been used for bracketing and also to calculate the correct attitude angle. The load capacity is simply equal to the vertical load component. Initially, the non-dimensional top foil deflection W is assumed as zero. To start with the iteration, the non-dimensionalize pressures at all the mesh points are assumed as 1 (i.e. ambient pressure) and those at the boundaries are also set to the ambient pressure.

Newton-Raphson method has been used to solve the discretized Reynolds Eqn. (2.8) for air pressure $\mathbf{p}$ in this present work. Once the pressure is found out the non-dimensional top foil deflection W is calculated. After that, substituting the new value of non-dimensional top foil deflection W in the equation of film thickness, the quadratic equation is solved for all the mesh points to estimate the pressure at all these points. This quadratic equation would not be satisfied for the pressures which are assumed to be constant in the beginning. Hence, the iterative process is carried out until the following convergence criterion is satisfied.

$$\frac{\left|\sum\left(\mathbf{p}^{(k-1)}\right)-\sum\left(\mathbf{p}^{(k)}\right)\right|}{\left|\sum\left(\mathbf{p}^{(k)}\right)\right|}\leq 10^{-6} \tag{2.11}$$

2.4.2. Newton-Raphson Method

Newton-Raphson method has been used to solve the discretized Reynolds Eqn. (2.8) for air pressure **p** in this present work. And in order to apply Newton-Raphson method the residue vector **r** is define in Eqn. (2.8) as

$$\mathbf{r}_q = \left(\mathbf{p}_q^e\right)^T \mathbf{A}_q^e \mathbf{p}_q^e + \mathbf{b}_q^e \mathbf{p}_q^e \qquad \text{where } q = 1,2,...,(m+1)(n+1) \tag{2.12}$$

Where, $\mathbf{r}_q$ is the residue vector for q^{th} node and its length is 5×1. The length of the residue vector **r** is $(m+1)(n+1)$. The residue vector of the q^{th} node for the k^{th} iteration is

$$\left(\mathbf{r}_q^e\right)^{(k)} = \left[\left(\mathbf{p}_q^e\right)^T\right]^{(k)} \left(\mathbf{A}_q^e\right)^{(k)} \left(\mathbf{p}_q^e\right)^{(k)} + \left(\mathbf{b}_q^e\right)^{(k)} \left(\mathbf{p}_q^e\right)^{(k)} \quad \text{where } q = 1,2,..,(m+1)(n+1) \tag{2.13}$$

The q^{th} row of the sensitivity matrix, **G** is calculated as

$$\left(\mathbf{G}_q\right)^{(k)} = \left[\left(\mathbf{p}_q^e\right)^T\right]^{(k)} \left[\left(\mathbf{A}_q^e\right)^{(k)} + \left\{\left(\mathbf{A}_q^e\right)^T\right\}^{(k)}\right] + \left(\mathbf{b}_q^e\right)^{(k)} \qquad \text{where } q = 1,2,...,(m+1)(n+1) \tag{2.14}$$

The size of the matrix **G** is $\left[(m+1)(n+1)\times(m+1)(n+1)\right]$.

And the pressure is updated as : $$\mathbf{p}^{(k+1)} = \mathbf{p}^{(k)} - \lambda^{(k)} \left(\mathbf{G}^{-1}\right)^{(k)} \mathbf{r}^{(k)} \tag{2.15}$$

where, $\mathbf{p}^{(k+1)}$ and $\mathbf{p}^{(k)}$ are the pressures at $(k+1)$ th and k^{th} iterations respectively. $\mathbf{G}^{(k)}$ is the sensitivity matrix at k^{th} iteration. $\lambda^{(k)}$ is the k^{th} step length. The computation is stopped when the error between two successive iteration steps is smaller than 1×10^{-6}.

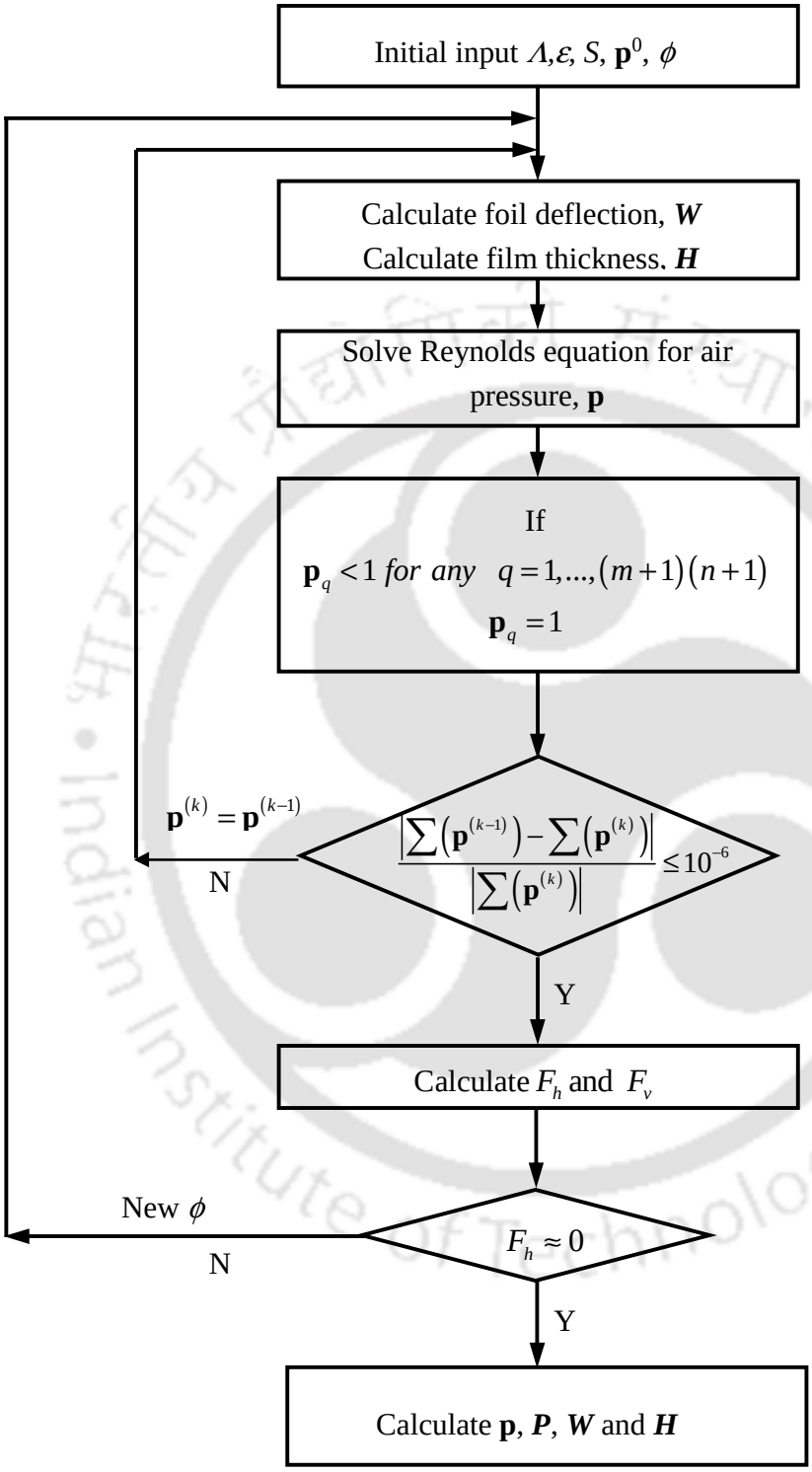

Fig. 2.4: Flowchart of solution algorithm

2.5. Time Transient Stability Analysis of Rigid Rotor Supported on Two Symmetrical GFBs

An attempt is being made here to determine the mass parameter which is a measure of stability of GFBs with the help of solution of dynamic Reynolds equation and the equations of motion of the rigid rotor supported on two symmetrical GFBs under unidirectional load at every time step. A non-linear time transient method is used to simulate the journal center trajectory and thereby estimate the mass parameter which is a function of speed.

2.5.1. Equations of motion of a rigid rotor supported on gas foil journal bearings

For the derivation of equations of motion of a rotor-bearing system, consider a symmetric rigid disc of mass 2*M*, supporting a static load $2W_0$ along X-axis as shown in Fig. (2.5). The disc is mounted on two identical hydrodynamic gas journal bearings.

The above rotor-bearing system may be fully described for nonlinear transient simulation by the coordinate system as shown in Fig. (2.6), where, *x(t)* and *y(t)* are the co-ordinates of the rotor mass centre, and F_X, F_Y are the fluid film bearing reaction forces. Since the rotor is rigid, the centre of mass displacements is identical to those of the journal centre.

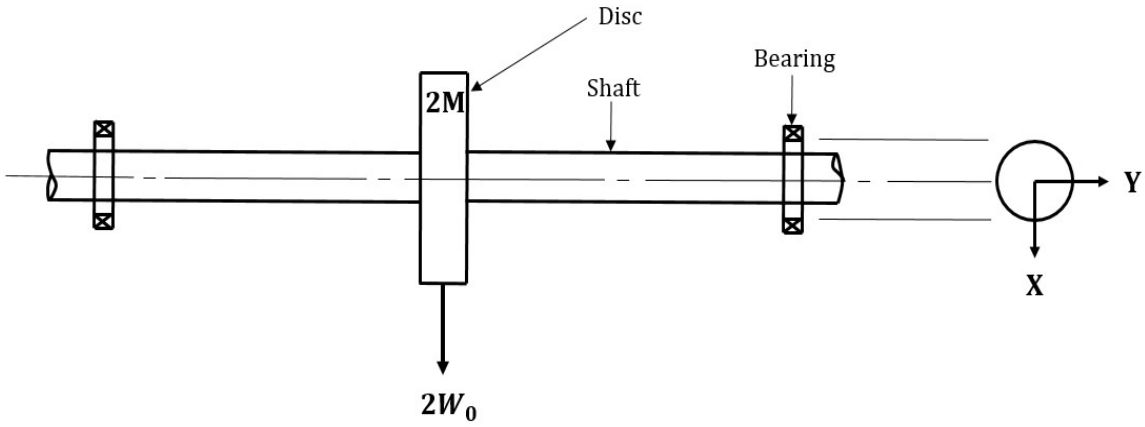

Fig. 2.5: Rotor-Bearing configuration

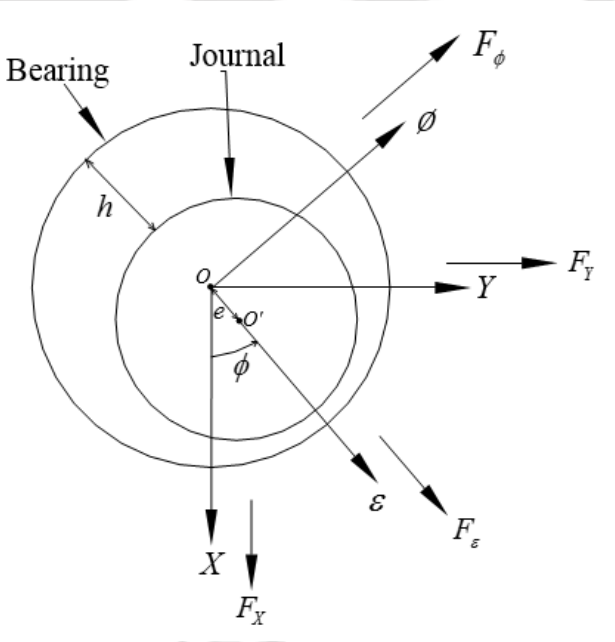

Fig. 2.6: Plain circular journal bearing

The equations of motion of the rotating system at constant rotational speed ω are given by,

$$M\ddot{x} = F_X + W_0 \tag{2.16}$$

$$M\ddot{y} = F_Y \tag{2.17}$$

Displacements of rotor centre along x and y directions in terms of e and ϕ are given by,

$$x(t) = e(t)\cos\phi(t) \tag{2.18}$$

$$y(t) = e(t)\sin\phi(t) \tag{2.19}$$

Fluid film bearing reaction forces in terms of e and ϕ are given by

$$F_X = F_\varepsilon \cos\phi + F_\phi \sin\phi \tag{2.20}$$

$$F_Y = F_\varepsilon \sin\phi + F_\phi \cos\phi \tag{2.21}$$

Substituting the values of x(t), y(t), F_X and F_Y in Eqns. 2.16 and 2.17 we get,

$$M\omega^2\ddot{e} - Me\omega^2\dot{\phi}^2 - F_\varepsilon - W_0\cos\phi = 0 \tag{2.22}$$

$$Me\omega^2\ddot{\phi} + 2M\omega^2\dot{e}\dot{\phi} - F_\phi + W_0\sin\phi = 0 \tag{2.23}$$

By using the substitution,

$$\varepsilon = \frac{e}{C}$$

we get the non-dimensional equations of motion in the following form

$$\bar{M}\bar{W}_0\left[\ddot{\varepsilon} - \varepsilon\left(\dot{\phi}\right)^2\right] = \bar{F}_\varepsilon + \bar{W}_0\cos\phi \tag{2.24}$$

$$\bar{M}\bar{W}_0\left[\varepsilon\ddot{\phi} + 2\dot{\varepsilon}\dot{\phi}\right] = \bar{F}_\phi - \bar{W}_0\sin\phi \tag{2.25}$$

where,

$$\bar{M} = \frac{MC\omega^2}{W_0},\ \bar{W} = \frac{W_0}{p_a R^2},\ \bar{F}_\varepsilon = \frac{F_\varepsilon}{p_a R^2},\ \bar{F}_\phi = \frac{F_\phi}{p_a R^2}$$

Reynolds equation for dynamic state (Eqn. 2.5) and equations of motion (Eqn. 2.24 and Eqn. 2.25) are solved successively at every time step for obtaining the values of $\varepsilon, \phi, \dot{\varepsilon}$ and $\dot{\phi}$. Once these values are calculated, the motion trajectories are obtained by plotting the attitude angle and eccentricity ratio at every time step showing position of journal orbit at various time steps. By observing these trajectories it can be ascertained whether the rotor system is stable, unstable or at critical condition. It is observed that at a certain value of mass parameter journal centre ends in a limit cycle and above that there is transition in rotor motion from stable to unstable state. The corresponding value of the mass parameter at this transition is known as critical mass parameter.

2.5.2. Implementation of Runge-Kutta method to the equations of motion

The equations of motion of rigid rotor (Eqn. 2.24 and Eqn. 2.25) are second order ordinary differential equations and hence these equations are solved by using an appropriate solution method. In the present study, these equations have been solved by using the fourth order Runge-Kutta method. The implementation of fourth order Runge-Kutta method for the solution of these equations are given as,

Step 1: Deducing the second order of Eqn. (2.24) and Eqn. (2.25) into first order equations.

$$f_1 = \dot{\varepsilon}$$

$$f_2 = \dot{\phi}$$

$$f_3 = \ddot{\varepsilon} = \frac{\bar{F}_\varepsilon + \bar{W}\cos\phi}{\bar{M}\bar{W}} + \varepsilon\dot{\phi}^2$$

$$f_4 = \ddot{\phi} = \frac{\bar{F}_\phi + \bar{W}\sin\phi}{\varepsilon\bar{M}\bar{W}} - \frac{2\dot{\varepsilon}\dot{\phi}}{\varepsilon}$$

Step 2: Calculating the values of k_1, k_2, k_3, k_4, l_1, l_2, l_3, l_4, m_1, m_2, m_3, m_4, n_1, n_2, n_3 and n_4 *by* using the following expressions

$$k_1 = \Delta\tau . f_1\left(\dot{\varepsilon}\right)$$

$$l_1 = \Delta\tau . f_2\left(\dot{\phi}\right)$$

$$m_1 = \Delta\tau . f_3\left(\varepsilon, \phi, \dot{\varepsilon}, \dot{\phi}, \bar{M}, \bar{W}, \bar{F}_\varepsilon, \bar{F}_\phi\right)$$

$$n_1 = \Delta\tau . f_4\left(\varepsilon, \phi, \dot{\varepsilon}, \dot{\phi}, \bar{M}, \bar{W}, \bar{F}_\varepsilon, \bar{F}_\phi\right)$$

$$k_2 = \Delta\tau . f_1\left(\dot{\varepsilon} + \frac{1}{2}m_1\right)$$

$$l_2 = \Delta\tau . f_2\left(\dot{\phi} + \frac{1}{2}n_1\right)$$

$$m_2 = \Delta\tau . f_3\left(\varepsilon + \frac{1}{2}k_1, \phi + \frac{1}{2}l_1, \dot{\varepsilon} + \frac{1}{2}m_1, \dot{\phi} + \frac{1}{2}n_1, \bar{M}, \bar{W}, \bar{F}_\varepsilon, \bar{F}_\phi\right)$$

$$n_2 = \Delta\tau . f_4\left(\varepsilon + \frac{1}{2}k_1, \phi + \frac{1}{2}l_1, \dot{\varepsilon} + \frac{1}{2}m_1, \dot{\phi} + \frac{1}{2}n_1, \bar{M}, \bar{W}, \bar{F}_\varepsilon, \bar{F}_\phi\right)$$

$$k_3 = \Delta\tau . f_1\left(\dot{\varepsilon} + \frac{1}{2}m_2\right)$$

$$l_3 = \Delta\tau . f_3\left(\dot{\phi} + \frac{1}{2}n_2\right)$$

$$m_3 = \Delta\tau . f_3\left(\varepsilon + \frac{1}{2}k_2, \phi + \frac{1}{2}l_2, \dot{\varepsilon} + \frac{1}{2}m_2, \dot{\phi} + \frac{1}{2}n_2, \bar{M}, \bar{W}, \bar{F}_\varepsilon, \bar{F}_\phi\right)$$

$$n_3 = \Delta\tau . f_4\left(\varepsilon + \frac{1}{2}k_2, \phi + \frac{1}{2}l_2, \dot{\varepsilon} + \frac{1}{2}m_2, \dot{\phi} + \frac{1}{2}n_2, \bar{M}, \bar{W}, \bar{F}_\varepsilon, \bar{F}_\phi\right)$$

$$k_4 = \Delta\tau . f_1\left(\dot{\varepsilon} + m_3\right)$$

$$l_4 = \Delta\tau . f_2\left(\dot{\phi} + n_3\right)$$

$$m_4 = \Delta\tau . f_3\left(\varepsilon + k_3, \phi + l_3, \dot{\varepsilon} + m_3, \dot{\phi} + n_3, \bar{M}, \bar{W}, \bar{F}_\varepsilon, \bar{F}_\phi\right)$$

$$n_4 = \Delta\tau . f_4\left(\varepsilon + k_3, \phi + l_3, \dot{\varepsilon} + m_3, \dot{\phi} + n_3, \bar{M}, \bar{W}, \bar{F}_\varepsilon, \bar{F}_\phi\right)$$

Step 3: Calculating $\Delta\varepsilon$, $\Delta\phi$, $\Delta\dot{\varepsilon}$ and $\Delta\dot{\phi}$ with the help of following expressions,

$$\Delta\varepsilon = \frac{1}{6}\left(k_1 + 2k_2 + 2k_3 + k_4\right)$$

$$\Delta\phi = \frac{1}{6}\left(l_1 + 2l_2 + 2l_3 + l_4\right)$$

$$\Delta\dot{\varepsilon} = \frac{1}{6}\left(m_1 + 2m_2 + 2m_3 + m_4\right)$$

$$\Delta\dot{\phi} = \frac{1}{6}\left(n_1 + 2n_2 + 2n_3 + n_4\right)$$

Step 4: Finding the values of $\varepsilon, \phi, \dot{\varepsilon}$ and $\dot{\phi}$ for each and every time step with the following expressions.

$$\varepsilon_{i+1} = \varepsilon_i + \Delta\varepsilon$$

$$\phi_{i+1} = \phi_i + \Delta\phi$$

$$\dot{\varepsilon}_{i+1} = \dot{\varepsilon}_i + \Delta\dot{\varepsilon}$$

$$\dot{\phi}_{i+1} = \dot{\phi}_i + \Delta\dot{\phi}$$

Step 5: Finally, by plotting the values of ε and ϕ in polar graph, the trajectory of journal centre will be attained.

2.8. Summary

In this chapter, a general description of the bump type gas foil bearing (GFB) and the governing Reynolds equation and the film thickness equation has been presented. The solution methodology and the algorithm are outlined in the form of flow chart. The use of finite difference method (FDM) to discretize the non dimensional governing equations and the application of Newton-Raphson method to solve the discretized Reynolds equation for air pressure (**p**) has also been detailed.

Furthermore, the equations of motion of rigid rotor supported on two symmetrical gas foil journal bearing has been derived for the study of nonlinear stability analysis. The equations of motion and the solution of dynamic Reynolds equation are then solved under unidirectional load at every time step to simulate the journal center trajectory and thereby estimate the mass parameter which is a function of speed.

The formulations of different numerical models of the foil structure of the GFBs have been discussed in the following chapter.

Chapter 3

DIFFERENT NUMERICAL MODELS OF THE FOIL STRUCTURE

3.1. Introduction

In the previous chapter, the general description of the bump type gas foil bearing, the basic governing equations, solution methods and its methodology etc. have been presented. The hydrodynamic pressure generations and the film thickness equations have also been reflected, however the deflection of the foil (***W***) which undergoes by the action of hydrodynamic pressure is by and large overseen by the nature of foil structure considered. The compliant foil structure which gives flexibility to GFB hence can be modeled in several ways from simple model considering only deflection of bump foils to more complex models considering deflection of bump as well as top foil. As such this chapter deals in describing the different numerical models of the foil structure which have been considered. The simple elastic foundation model which is the original work of Heshmat et al. [9], which many other researchers have worked with have been extended to account for and integrate with the elastic deformation of the top foil. Primarily, four different models of the foil structure have been considered. Firstly, the simple elastic foundation model [9], secondly, a one-dimensional top foil model

considering an axially averaged gas film pressure which acts along the top foil width has been considered. The top foil structural model is modelled as a beam element without the effects of curvature incorporating the bump strip layer as a series of linear springs which not connected with each other. The interactions between adjacent bumps are altogether neglected and the stiffness of each bump is observed as constant (regardless of the load) and does not denote any change in the nominal or manufactured bump pitch. Finally, two-dimensional (2D) numerical model of the top foil where in the top foil is modeled as a two dimensional flat plate supported on axially distributed linear springs located at every bump pitch. The 2D numerical formulation of the foil structure were based on two plate model, basically the classical plate theory (CPT) and the shear deformation plate theory (SPT) respectively. The numerical formulation of each foil structural model considered has been entails in details and the deductions and the assumptions made also have been specified.

3.2. Simple Elastic Foundation Model

Most of the published models of the foil structure are based on the original work of Heshmat et al [9], wherein it proposed a simple foil structure of the bump type GFB considering only the deflection of bump foils. This analysis relies on several assumptions and many researchers have reproduced these results using the same assumptions. The assumptions made are as follows:

1) The stiffness of a bump strip is uniformly distributed throughout the bearing surface, i.e. the bump strip is regarded as a uniform elastic foundation.
2) The bump stiffness is constant, independent of the actual bump deflection, not related to or constrained by adjacent bumps.
3) The top foil does not sag between adjacent bumps. The top foil does not have either bending or membrane stiffness, and its deflection follows that of the bump
4) Film thickness does not vary along the bearing length.

With this considerations, the deformation (w_t) depends on the bump compliance (α) and the average pressure across the bearing width as shown Fig. 3.1,

$$w_t = \alpha(\bar{p} - p_a) \tag{3.1}$$

where, $\bar{p}$ and α are the arithmetic mean pressure along the radial direction and compliance of the bump foil.

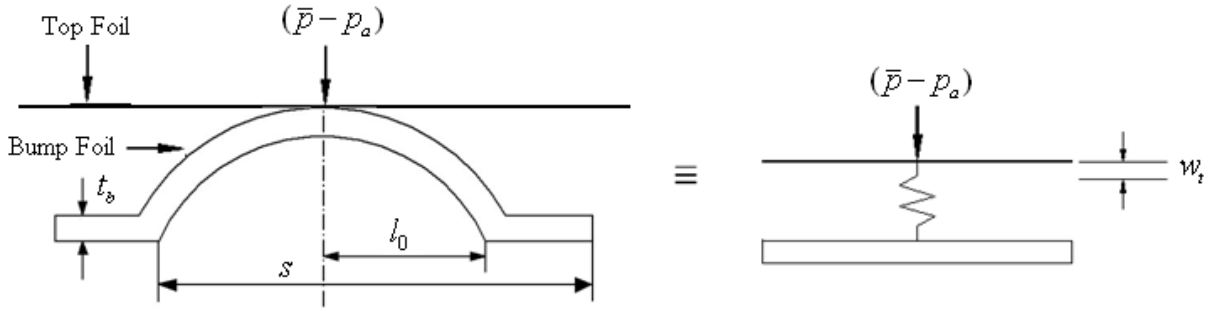

Fig. 3.1: A single segment of bump foil

The dimensionless deflection of the bump is given by

$$W = S(P-1) \tag{3.2}$$

where, $S = \frac{\alpha p_a}{C}$ is the compliance coefficient, α being the compliance of the bump foil, C is the bearing radial clearance; p_a is the ambient pressure and P is the dimensionless pressure.

The coupling of the simple elastic foil model equation Eqn. (3.2) with the solution of Reynolds equation Eqn. (2.6) is straightforward as described in the flow chart of Fig. (2.4) for the prediction of the performance characteristic of GFBs.

3.3. 1D Beam Model for Top Foil

The simple elastic model discussed in Section 3.2 did not took into account the bending effect of the foil structure, hence by incorporating the bending of the top foil, the 1D foil structure has been modelled as a Euler-like beam element. The top foil is modelled as a one dimensional (1D) structural model, Fig. (3.2) with one end of the top foil fixed, i.e. with transverse deflection and without any rotational effect while keeping the other end free. The stiffness of the bump strip is assumed to be uniformly distributed throughout the bearing surface, i.e. the bump strip is regarded as a uniform elastic foundation and independent of the

actual bump deflection and an average pressure causes a uniform elastic deformation along the top foil of width (L).

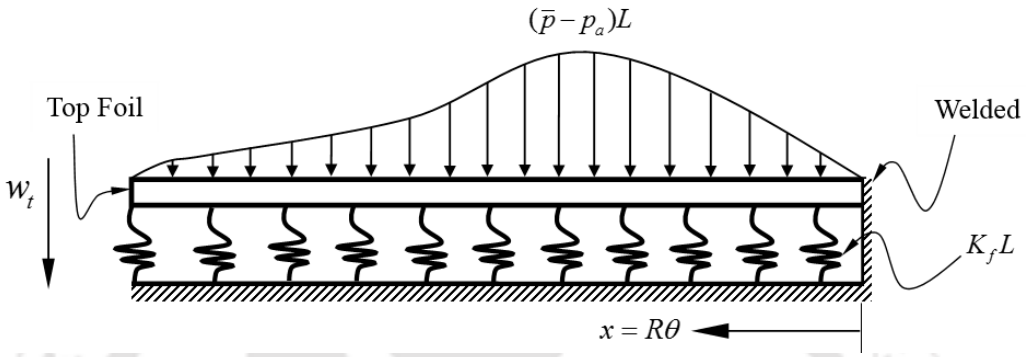

Fig. 3.2: 1D Structural model of top foil

The top foil Transverse deflection (w_t) of top foil along the circumferential axis (x) is governed by the fourth order differential equation [94],

$$\frac{d^2}{d\theta^2}\left(\frac{E_t I_t}{LR^4}\frac{d^2 w_t}{d\theta^2}\right)+K_f w_t=(\bar{p}-p_a) \tag{3.3}$$

where E_t, I_t and K_f are the elastic modulus, moment of inertia and structural stiffness per unit area respectively and $(\bar{p}-p_a)L$ is the distributed load per unit circumferential length. Note that Eqn. (3.3) is the typical formulation for the deflections of an Euler-like beam.

3.3.1. Normalization of the governing equation of the top foil

The transverse deflection of the top foil is governed by the fourth order differential equation as shown in Eqn. (3.3). This equation is normalized by

substituting Eqn. (2.4) and converted it into the non-dimensional form which is given by

$$A\frac{d^2}{d\theta^2}\left(\frac{d^2W}{d\theta^2}\right)+\frac{W}{S}=(P-1) \tag{3.4}$$

where, $A=\frac{E_t I_t C}{p_a L R^4}$ is called the top foil structural stiffness; $S=\frac{p_a}{CK_f}$ and K_f is the structural stiffness per unit area. Note that in Eqn. (3.4) $A\frac{d^2}{d\theta^2}\left(\frac{d^2W}{d\theta^2}\right)$ denotes the 1D foil bending part of the beam element, which when excluded the equation becomes a simple elastic formulation with foil deflection equivalent to Eqn. (3.2).

3.3.2. Discretization of the governing equation using finite element formulation

Now Eqn. (3.4) is discretized using the finite element method [94]. The weak form over a finite element domain as shown in Fig. (3.3) becomes

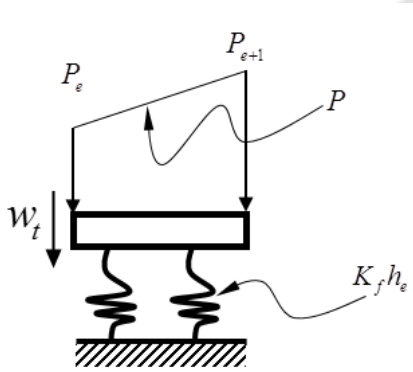

Fig. 3.3: A 1D beam element

$$0=\int_{\theta_e}^{\theta_{e+1}}\left(A\frac{d^2V}{d^2\theta}\frac{d^2W}{d^2\theta}+\frac{1}{S}VW-V(P-1)\right)d\theta-V|_{\theta_e}\,Q_1^e-\left(-\frac{dV}{d\theta}\right)\Bigg|_{\theta_e}Q_2^e-V|_{\theta_e+1}\,Q_3^e-\left(-\frac{dV}{d\theta}\right)\Bigg|_{\theta_e+1}Q_4^e \tag{3.5}$$

where V is the weight function. Q_1^e and Q_3^e denote the shear forces, and Q_2^e and Q_4^e denote the bending moments at the boundary of an element, i.e.,

$$Q_1^e\equiv\left[\frac{d}{d\theta}\left(A\frac{d^2W}{d\theta^2}\right)\right]\Bigg|_{\theta_e};\ Q_2^e\equiv\left(A\frac{d^2W}{d\theta^2}\right)\Bigg|_{\theta_e};$$

$$Q_1^e\equiv-\left[\frac{d}{d\theta}\left(A\frac{d^2W}{d\theta^2}\right)\right]\Bigg|_{\theta_e+1};\ Q_2^e\equiv-\left(A\frac{d^2W}{d\theta^2}\right)\Bigg|_{\theta_e+1} \tag{3.6}$$

An appropriate interpolation function W must satisfy the essential boundary conditions, i.e.

$$W^e=\sum_{j=1}^{4}w_j^e\psi_j^e=w_1^e\psi_1^e+w_2^e\psi_2^e+w_3^e\psi_3^e+w_4^e\psi_4^e \tag{3.7}$$

where $\{\psi\}$ is the set of Hermite cubic interpolation function [94].

Now, setting $V=\{\psi\}$ and substitution of Eqn. (3.7) into Eqn. (3.5) yields the force equation

$$[K^e]\{w^e\}=\{F^e\} \tag{3.8}$$

$[K^e]$ = elemental stiffness matrix

$\{w^e\}$ = vector of primary nodal variables or generalized displacements

$\{F^e\}$ = force vector

The expression for the stiffness matrix $\left[K^e\right]$ is given by

$$\left[K^e\right]=\frac{2A}{h_e^3}\begin{bmatrix} 6 & -3h_e & -6 & -3h_e \\ -3h_e & 2h_e^2 & 3h_e & h_e^2 \\ -6 & 3h_e & 6 & 3h_e \\ -3h_e & h_e^2 & 3h_e & 2h_e^2 \end{bmatrix}+\frac{h_e}{420S}\begin{bmatrix} 156 & -22h_e & 54 & 13h_e \\ -22h_e & 4h_e^2 & -13h_e & -3h_e^2 \\ 54 & -13h_e & 156 & 22h_e \\ 13h_e & -3h_e^2 & 22h_e & 4h_e^2 \end{bmatrix} \tag{3.9}$$

where, $A=\frac{E_t I_t C}{p_a L R^4}$ is called the top foil structural stiffness; $S=\frac{p_a}{CK_f}$ and K_f is the structural stiffness per unit area.

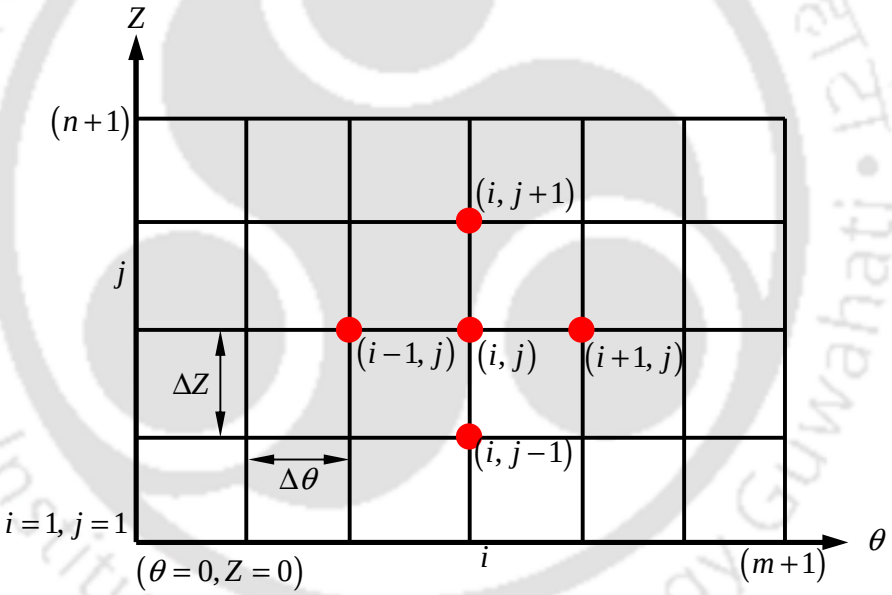

Fig. 3.4: An exfoliated view of a bearing showing the mesh for finite difference mesh

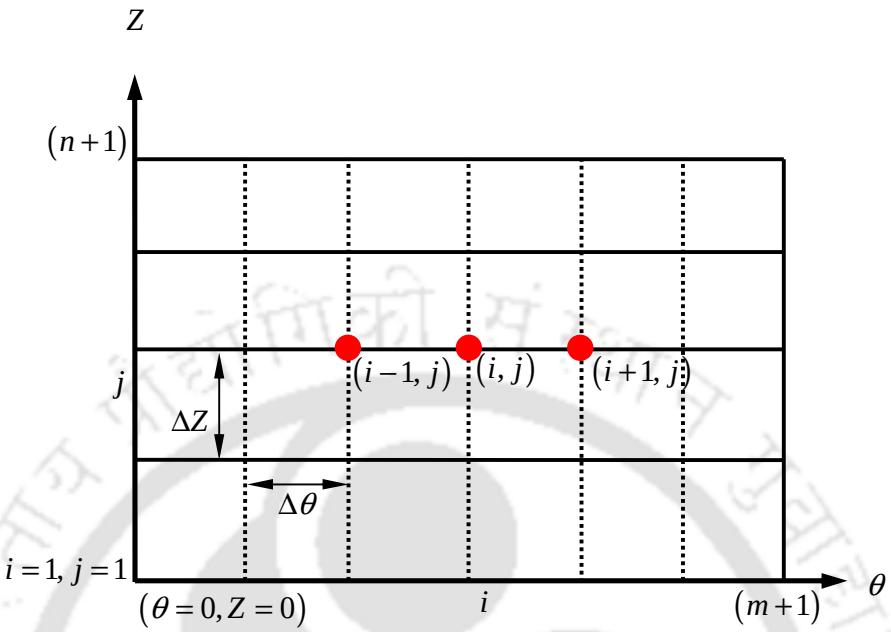

Fig. 3.5: An exfoliated view of a bearing showing the mesh for 1D finite element mesh

The domain is discretized as m divisions along θ direction and n divisions along Z direction. So the grid size is $(m+1)\times(n+1)$. This grid is used for solving the Reynolds equation for calculating the hydrodynamic gas pressure using finite difference scheme. An exfoliated view of a bearing showing the mesh for finite difference mesh is shown in Fig. (3.4). The same discretization of the domain is used for calculating the foil deflection using finite element method. There will be (n+1) individual 1D beams for a mesh size of $(m+1)\times(n+1)$. A typical mesh for 1D beam element is shown in Fig. (3.5). The size of the global matrix for a particular 1D beam will be $\left[2(m+1)\right]\times\left[2(m+1)\right]$ considering two degrees of freedom per node.

We can write the assembled equation for the j^{th} beam as

$$[K_j]\{w_j\}=\{F_j\} \tag{3.10}$$

where $[K_j]$ is the assembled stiffness matrix, $\{w_j\}$ is the nodal deflections and slopes and $\{F_j\}$ is the force vector for j^{th} 1D beam.

A similar equation as Eqn. (3.10) is attained for the entire domain by assembling the stiffness matrix for the entire domain and this is shown in Eqn. (3.11) and (3.12).

$$\begin{bmatrix} [K_1] & [0] & [0] & [0] & [0] \\ [0] & \vdots & \vdots & \vdots & [0] \\ [0] & \dots & [K_j] & \dots & [0] \\ [0] & \vdots & \vdots & \vdots & [0] \\ [0] & [0] & [0] & [0] & [K_{n+1}] \end{bmatrix} \begin{Bmatrix} \{w_1\} \\ \vdots \\ \{w_j\} \\ \vdots \\ \{w_{n+1}\} \end{Bmatrix} = \begin{Bmatrix} \{F_1\} \\ \vdots \\ \{F_j\} \\ \vdots \\ \{F_{n+1}\} \end{Bmatrix} \tag{3.11}$$

$$[K_G]\{w_G\}=\{F_G\} \tag{3.12}$$

where, $[K_G]$ is the global stiffness matrix and its size is $\left[2(n+1)(m+1)\times 2(n+1)(m+1)\right]$, $\{w_G\}$ is the global foil deflection vector and its size is $\left[2(n+1)(m+1)\times 1\right]$ and $\{F_G\}$ is the global force vector and its size is $\left[2(n+1)(m+1)\times 1\right]$.

3.3.3. Calculation of load vector from the pressure obtained from Reynolds equation

The Reynolds equation (Eqn. 2.6) is solved for calculating the nodal hydrodynamic gas pressure using finite difference scheme. Suppose P_i and P_{i+1} are the nodal hydrodynamic gas pressure for i^{th} and $(i+1)^{th}$ nodes respectively calculated by solving Reynolds equation using finite difference scheme. q_i and q_{i+1} are calculated as $(P_i - 1)$ and $(P_{i+1} - 1)$. The nodal force in the finite element model due to this nodal hydrodynamic gas pressure for an element is calculated using Eqn. (3.13)

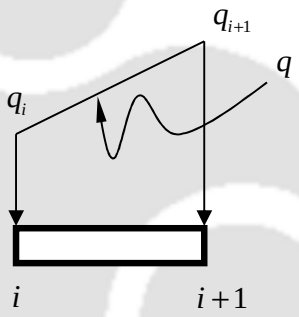

Fig. 3.6: A finite element showing the nodal hydrodynamic gas pressure obtained by solving Reynolds equation

$$\{w^e\} = \begin{Bmatrix} w_1^e \\ w_2^e \\ w_3^e \\ w_4^e \end{Bmatrix}; \quad \{F^e\} = \frac{q_i h_e}{12} \begin{Bmatrix} 6 \\ -h_e \\ 6 \\ h_e \end{Bmatrix} - \frac{(q_{i+1} - q_i)}{60} \begin{Bmatrix} -9h_e \\ 2h_e^2 \\ -21h_e \\ -3h_e^2 \end{Bmatrix} \tag{3.13}$$

where, $q_i = (P_i - 1)$, $q_{i+1} = (P_{i+1} - 1)$

The nodal force $\{F_j\}$ for the entire j^{th} beam is calculated by assembling the elemental contribution. The nodal force $\{F_G\}$ for the entire domain is also

calculated in a similar way.

3.3.4. Coupling of FE solution with the FDM solution

The nodal foil deflection calculated using finite element method is used in Eqn. (2.7) to calculate the non-dimensional film thickness. This non-dimensional film thickness is used in Eqn. (2.6) to calculate the hydrodynamics gas pressure. The solution of Reynolds equation (Eqn. 2.6) is straightforward and the flow chart for the prediction of the performance characteristic of GFBs is shown in Fig. (2.4).

3.4. 2D Model for Top Foil

In the previous two foil models so far discussed, i.e., the simple elastic model which considers only the deflection of bump foils and 1D model which assumes the top foil as a beam element incorporating the effect of bending of beams. This section entails the modelling of foil structure as a two dimensional flat plate. The foil structure are modelled as flat plate supported on axially distributed linear springs located at every bump pitch as shown in Figs. (3.7) and (3.8). The modelling considers two plate theory namely the classical plate theory (CPT) and the shear deformation theory (SDT) and based on these two theories the foil structure have been formulated using the standard methodology as given in [94].

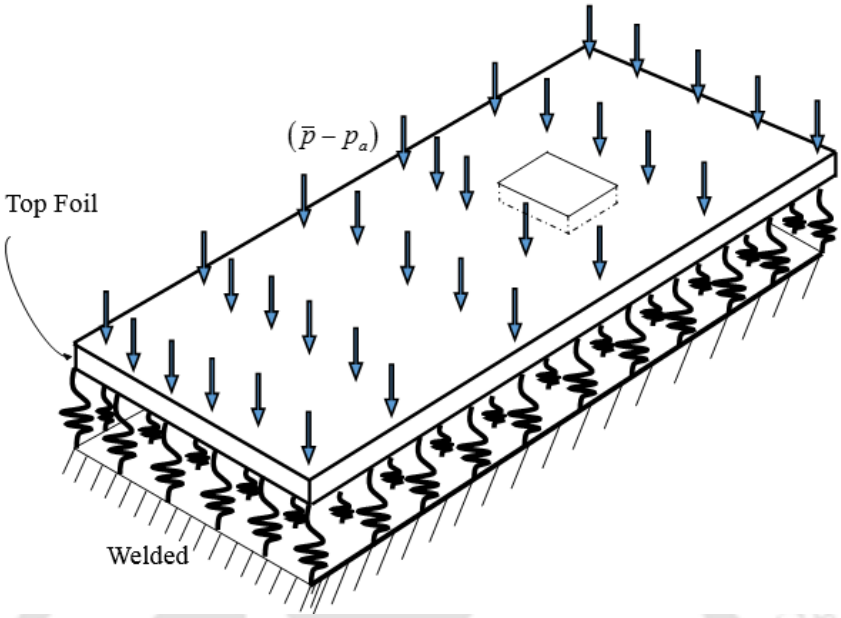

Fig. 3.7: Configuration of top foil supported on bump strips and its 2D structural model

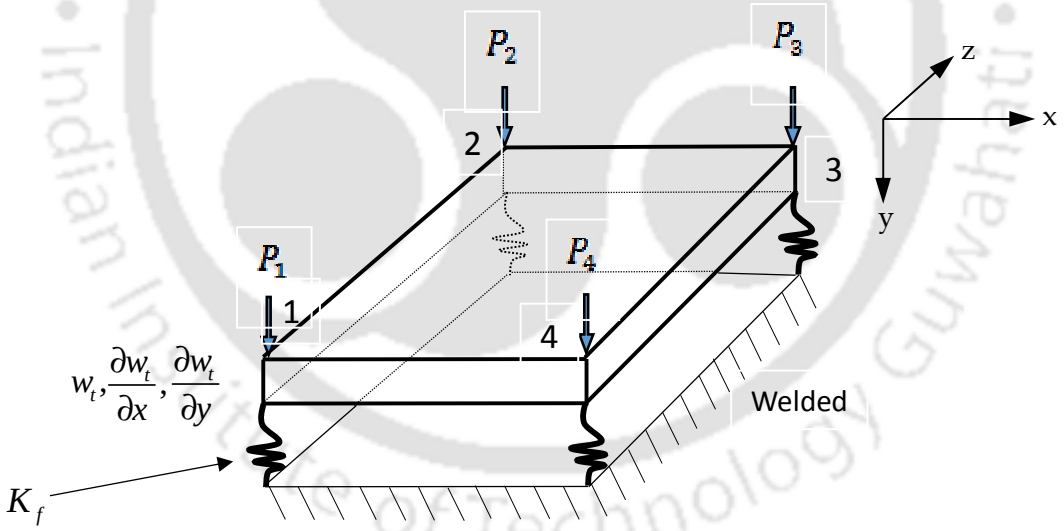

Fig. 3.8: Details of one FE element

3.4.1. Classical plate theory model (CPT)

The CPT is based on the assumptions that a straight line perpendicular to the plane of the plate is (i) inextensible, (ii) remains straight, and (iii) rotates such that

it remains perpendicular to the tangent to the deformed surface. Assuming the above accounts and considering the details as given in [94], the governing differential equation (i.e., the Euler-Lagrange equation) governing w_t is given as,

$$\frac{\partial^2}{\partial x^2}\left(D_{11}\frac{\partial^2 w_t}{\partial x^2}+D_{12}\frac{\partial^2 w_t}{\partial z^2}\right)+\frac{\partial^2}{\partial z^2}\left(D_{12}\frac{\partial^2 w_t}{\partial x^2}+D_{22}\frac{\partial^2 w_t}{\partial z^2}\right)+2\frac{\partial^2}{\partial x\partial z}\left(2D_{66}\frac{\partial^2 w_t}{\partial x\partial z}\right)+K_f w_t = (\bar{p}-p_a)-I_o\frac{\partial^2 w_t}{\partial t^2}+I_2\frac{\partial^2}{\partial t^2}\left(\frac{\partial^2 w_t}{\partial x^2}+\frac{\partial^2 w_t}{\partial z^2}\right) \quad (3.14)$$

where, D_{11} D_{12} D_{22} and D_{66} are the plate material stiffness given by

$$D_{11}=\frac{E_1 h^3}{12(1-\upsilon_{12}\upsilon_{21})},\ D_{22}=\frac{E_2 h^3}{12(1-\upsilon_{12}\upsilon_{21})},\ D_{12}=\frac{\upsilon_{12}E_2 h^3}{12(1-\upsilon_{12}\upsilon_{21})} \text{ and } D_{66}=\frac{G_{12}h^3}{12}$$

where, E_1 and E_2 are the anisotropic elastic moduli of the materials; υ_{12} and υ_{21} are the poisons ratio; G_{12} is the shear modulus of the material and t is the time.

In Eqn. (3.14) I_0 and I_2 are the mass moment of inertia defined as

$$I_0=\int_{-h/2}^{h/2}\rho dz=\rho h,\ I_2=\int_{-h/2}^{h/2}\rho z^2 dz=\frac{1}{12}\rho h^3;$$

where, h denotes the total thickness of the plate, ρ is the mass density of the material. However the present analysis does not consider the inertia effects.

Now, excluding the inertia terms (I_0 and I_2) Eqn. (3.14) becomes

$$\frac{\partial^2}{\partial x^2}\left(D_{11}\frac{\partial^2 w_t}{\partial x^2}+D_{12}\frac{\partial^2 w_t}{\partial z^2}\right)+\frac{\partial^2}{\partial z^2}\left(D_{12}\frac{\partial^2 w_t}{\partial x^2}+D_{22}\frac{\partial^2 w_t}{\partial z^2}\right)+2\frac{\partial^2}{\partial x\partial z}\left(2D_{66}\frac{\partial^2 w_t}{\partial x\partial z}\right)+K_f w_t=(\bar{p}-p_a) \quad (3.15)$$

3.4.1.1. Normalization of the governing equation of the top foil

Eqn. (3.15) can be normalized by substituting Eqn. (2.4),

$$S = \alpha p_a / C \qquad H = h/C \qquad z = Z/R \qquad \frac{x}{R} = \theta$$
$$y = Y/L \qquad P = \bar{p}/p_a \qquad \varepsilon = e/C \qquad W = w_t/C \tag{2.4}$$

Therefore, the normalized governing equation is given by

$$\frac{\partial^2}{\partial\theta^2}\left(D'_{11}\frac{\partial^2 W}{\partial\theta^2}+D'_{12}\frac{\partial^2 W}{\partial Z^2}\right)+\frac{\partial^2}{\partial Z^2}\left(D'_{12}\frac{\partial^2 W}{\partial\theta^2}+D'_{22}\frac{\partial^2 W}{\partial Z^2}\right)+4\frac{\partial^2}{\partial\theta\partial Z}\left(D'_{66}\frac{\partial^2 W}{\partial\theta\partial Z}\right)+\frac{W}{S}=(P-1) \tag{3.16}$$

where, $D'_{11}=\frac{C}{p_a R^4}D_{11}$, $D'_{12}=\frac{C}{p_a R^2 L^2}D_{12}$, $D'_{22}=\frac{C}{p_a L^4}D_{22}$, $D'_{66}=\frac{C}{p_a R^2 L^2}D_{66}$ (3.17)

and $D_{11}=\frac{E_1 h^3}{12(1-\upsilon_{12}\upsilon_{21})}$; $D_{12}=\frac{\upsilon_{12}E_1 h^3}{12(1-\upsilon_{12}\upsilon_{21})}$; $D_{22}=\frac{E_2 h^3}{12(1-\upsilon_{12}\upsilon_{21})}$; $D_{66}=\frac{G_{12}h^3}{12}$ (3.18)

In Eqn. (3.18), h is the the plate thickness, υ_{12} and υ_{21} are the poison's ratio, E_1 and E_2 are the anisotropic elastic moduli and G_{12} is the shear modulus of the material.

In Eqn. (3.16) it has been observed that by neglecting the top foil 2D term, $\frac{\partial^2}{\partial\theta^2}\left(D'_{11}\frac{\partial^2 W}{\partial\theta^2}+D'_{12}\frac{\partial^2 W}{\partial Z^2}\right)+\frac{\partial^2}{\partial Z^2}\left(D'_{12}\frac{\partial^2 W}{\partial\theta^2}+D'_{22}\frac{\partial^2 W}{\partial Z^2}\right)+4\frac{\partial^2}{\partial\theta\partial Z}\left(D'_{66}\frac{\partial^2 W}{\partial\theta\partial Z}\right)$

Eqn. (3.16) reduces to simple bump foil model with foil deflection depending on the compliance coefficient (S) and the hydrodynamic pressure (P).

3.4.1.2. Discretization of the governing equation using finite element formulation

Now the above Eqn. (3.16) is discretized using the finite element method [94] integrating over a 2D finite element domain.

An appropriate interpolation function W must satisfy the essential boundary conditions, i.e.

$$W^e = \sum_{j=1}^{n} w_j^e \psi_j^e = w_1^e \psi_1^e + w_2^e \psi_2^e + \cdots + w_n^e \psi_n^e \tag{3.19}$$

where $\{\psi\}$ is the set of interpolation function [3] and n is the number of interpolation function.

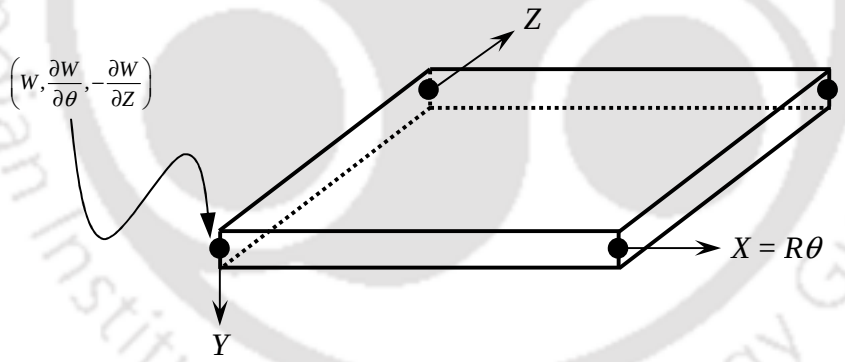

Fig. 3.9: Linear element for CPT with three degrees of freedom

$$\left(W, \frac{\partial W}{\partial \theta}, -\frac{\partial W}{\partial Z}\right) \textbf{ per node}$$

The domain is discretized as $(m+1)\times(n+1)$ for solving the Reynolds equation for calculating the hydrodynamic gas pressure using finite difference scheme. The same discretization of the domain is used for calculating the foil deflection using

finite element method. A typical mesh is shown in Fig. (3.10). The finite element equation for an element in matrix form can be written as

$$[K^e_{CPT}]\{w^e_{CPT}\}=\{F^e_{CPT}\} \tag{3.20}$$

where, $[K^e_{CPT}]$ is the elemental stiffness matrix, $\{w^e_{CPT}\}$ is the vector of primary nodal variables or generalized displacements, and $\{F^e_{CPT}\}$ is the force vector.

The elemental stiffness matrix $[K^e_{CPT}]$ can be written as

$$\left[K^e_{CPT}\right]=\int_{\Omega_e}[B_2]^T[C][B_2]d\mathbf{x} \tag{3.21}$$

where

$$[B_2]=\begin{bmatrix} \frac{\partial^2\psi_1}{\partial\theta^2} & \frac{\partial^2\psi_2}{\partial\theta^2} & \cdots & \frac{\partial^2\psi_{12}}{\partial\theta^2} \\ \frac{\partial^2\psi_1}{\partial Z^2} & \frac{\partial^2\psi_2}{\partial Z^2} & \cdots & \frac{\partial^2\psi_{12}}{\partial Z^2} \\ 2\frac{\partial^2\psi_1}{\partial\theta\partial Z} & 2\frac{\partial^2\psi_2}{\partial\theta\partial Z} & \cdots & 2\frac{\partial^2\psi_{12}}{\partial\theta\partial Z} \end{bmatrix}_{3\times12} \text{ and } [C]=\begin{bmatrix} D'_{11} & D'_{12} & 0 \\ D'_{12} & D'_{22} & 0 \\ 0 & 0 & D'_{66} \end{bmatrix}_{3\times3}$$

$\{\phi\}^T=\{\psi_1 \quad \psi_2 \quad \cdots \quad \psi_{12}\}^T$ and $\psi_1,\psi_2,\psi_3,\cdots,\psi_{12}$ are the shape functions. The procedure for calculation of the force vector $\{F^e_{CPT}\}$ is described in the next section.

A rectangular element with four nodes, with $\left(W,\frac{\partial W}{\partial\theta},-\frac{\partial W}{\partial Z}\right)$ at each node requires 12-term polynomial approximation of *W*.

$$W = a_1 + a_2\theta + a_3 Z + a_4\theta Z + a_5\theta^2 + a_6 Z^2 + a_7\theta^2 Z + a_8\theta Z^2 + a_9\theta^3 + a_{10} Z^3 + a_{11}\theta^3 Z + a_{12}\theta Z^3 \quad (3.22)$$

The size of the global matrix for a particular 2D CPT will be $\left[3(m+1)(n+1)\right]\times\left[3(m+1)(n+1)\right]$ considering three degrees of freedom per node. We can write the assembled equation for the entire domain as

$$[K_{CPT}]\{w_{CPT}\} = \{F_{CPT}\} \quad (3.23)$$

where, $[K_{CPT}]$ is the assembled stiffness matrix, $\{w_{CPT}\}$ is the nodal deflections and slopes and $\{F_{CPT}\}$ is the force vector.

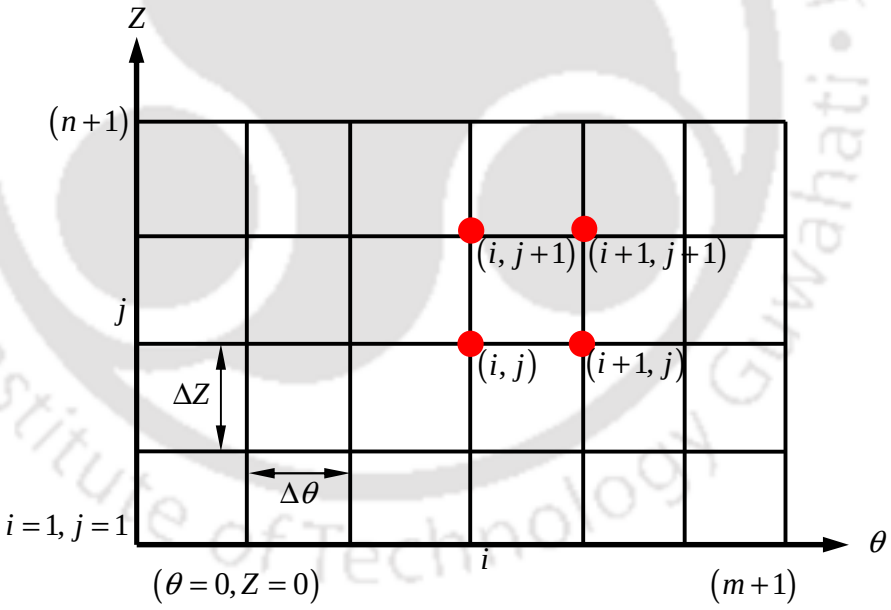

Fig. 3.10: An exfoliated view of a bearing showing the mesh for 2D finite element mesh

3.4.1.3. Calculation of load vector from the pressure obtained from Reynolds equation

The Reynolds equation (Eqn. 2.6) is solved for calculating the nodal hydrodynamic gas pressure using finite difference scheme. Suppose $P_{i,j}$, $P_{i,j+1}$, $P_{i+1,j+1}$, $P_{i+1,j}$ are the nodal non-dimensionalized hydrodynamic gas pressure for $(i,j)^{th}$, $(i, j+1)^{th}$, $(i+1, j+1)^{th}$ and $(i+1, j)^{th}$ nodes respectively (shown in Fig. 3.10) calculated by solving Reynolds equation using finite difference scheme. A finite element showing the nodal hydrodynamic gas pressure obtained by solving Reynolds equation is shown in Fig. (3.11). The nodal force in the finite element model due to this nodal hydrodynamic gas pressure for an element with nodes i^{th} and $(i+1)^{th}$ is calculated using Eqn. (3.24).

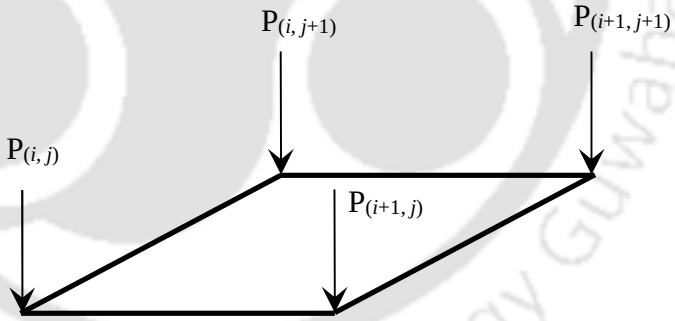

Fig. 3.11: A finite element showing the nodal hydrodynamic gas pressure obtained by solving Reynolds equation

Now the pressure at point on the domain is calculated as

$$P = N_1' P_{i,j} + N_2' P_{i,j+12} + N_3' P_{i+1,j+1} + N_4' P_{i+1,j} \tag{3.24}$$

where N_1', N_2', N_3', N_4' are the shape functions for nodes $(i,j)^{th}$, $(i, j+1)^{th}$, $(i+1, j+1)^{th}$ and $(i+1, j)^{th}$ nodes respectively and $(i,j)^{th}$, $(i, j+1)^{th}$, $(i+1, j+1)^{th}$ and $(i+1, j)^{th}$ nodes constitutes a four-noded quadrilateral elements.

Now $\{F_{CPT}^e\}$ is calculated as

$$\{F_{CPT}^e\} = \int_{\Psi} \mathbf{P}\ \{\mathbf{N}\}\, d\Psi \tag{3.25}$$

where, $\{\mathbf{N}\} = \{N_1 \quad N_2 \quad N_3 \quad N_4 \quad N_5 \quad N_6 \quad N_7 \quad N_8 \quad N_9 \quad N_{10} \quad N_{11} \quad N_{12}\}$ are the interpolation functions and calculated from Eqn. (3.22)

3.4.1.4 Coupling of FE solution with the FDM solution

As discussed in Section. (3.3.3) the nodal foil deflection calculated using finite element method is used in Eqn. (2.7) to calculate the non-dimensional film thickness. This non-dimensional film thickness is used in Eqn. (2.6) to calculate the hydrodynamics gas pressure. The solution of Reynolds equation (Eqn. 2.6) is straightforward and the flow chart for the prediction of the performance characteristic of GFBs is shown in Fig. (2.4).

3.4.2. Shear deformation plate theory (SDT)

In the SDT formulations, the assumptions made in CPT has been relaxed, such that the transverse normal may rotate without remaining normal to the mid-plane. Now, taking the anisotropic behavior of the material, the shear deformable plate

model has been modelled based on first-order shear deformation theory. As given in [94], the governing differential equation is given by

$$\frac{\partial Q_x}{\partial x}+\frac{\partial Q_z}{\partial z}+K_f w_t=-q \tag{3.26}$$

$$\frac{\partial M_{xx}}{\partial x}+\frac{\partial M_{xz}}{\partial z}=Q_x \tag{3.27}$$

$$\frac{\partial M_{xz}}{\partial x}+\frac{\partial M_{zz}}{\partial z}=Q_z \tag{3.28}$$

The shear forces Q_x and Q_z; bending moments M_{zz}, M_{xx}, and M_{xz} in the above equations are given by,

$$Q_x=K_s A_{55}\left(\phi_x+\frac{\partial w_t}{\partial x}\right) \qquad Q_z=K_s A_{44}\left(\phi_z+\frac{\partial w_t}{\partial z}\right) \qquad M_{xx}=D_{11}\frac{\partial \phi_x}{\partial x}+D_{12}\frac{\partial \phi_z}{\partial z}$$

$$M_{zz}=D_{12}\frac{\partial \phi_x}{\partial x}+D_{22}\frac{\partial \phi_z}{\partial z} \qquad M_{xz}=D_{66}\left(\frac{\partial \phi_x}{\partial z}+\frac{\partial \phi_z}{\partial x}\right) \tag{3.29}$$

Also, ϕ_x and ϕ_z in Eqn. (3.29) denote the rotation angles about the z and x axes, respectively, and D_{11}, D_{12}, D_{22}, D_{66}, A_{44} and A_{55} are given in Eqn. (3.18).

D_{11} D_{12} D_{22} and D_{66} are the plate material stiffness given by

$$D_{11}=\frac{E_1 h^3}{12(1-\upsilon_{12}\upsilon_{21})},\ D_{22}=\frac{E_2 h^3}{12(1-\upsilon_{12}\upsilon_{21})},\ D_{12}=\frac{\upsilon_{12}E_2 h^3}{12(1-\upsilon_{12}\upsilon_{21})} \text{ and } D_{66}=\frac{G_{12}h^3}{12}$$

$$A_{44}=G_{23}h \qquad A_{55}=G_{13}h \tag{3.30}$$

In Eqn. (3.30), h is the the plate thickness, υ_{12} and υ_{21} are the poison's ratio, E_1 and

E_2 are the anisotropic elastic moduli and G_{12} is the shear modulus of the material.

3.4.2.1. Normalization of the governing equation of the top foil

Eqns. (3.26-3.28) can be normalized by substituting Eqn. (2.4). Therefore, after substitution the non dimensional governing equations for 2D SDT of plate is given by

$$\frac{\partial}{\partial\theta}\left[K_s A'_{55}\left(\phi'_\theta+\frac{\partial W}{\partial\theta}\right)\right]+\frac{\partial}{\partial Z}\left[K_s A'_{44}\left(\phi'_Z+\frac{\partial W}{\partial Z}\right)\right]+\frac{W}{S}=-(\bar{P}-1) \tag{3.31}$$

$$\frac{\partial}{\partial\theta}\left(D'_{11}\frac{\partial\phi'_\theta}{\partial\theta}+D'_{12}\frac{\partial\phi'_Z}{\partial Z}\right)+\frac{\partial}{\partial Z}\left[D'_{66}\left(\frac{\partial\phi'_\theta}{\partial Z}+\frac{\partial\phi'_Z}{\partial\theta}\right)\right]=K_s A'_{55}\left(\phi'_\theta+\frac{\partial W}{\partial\theta}\right) \tag{3.32}$$

$$\frac{\partial}{\partial\theta}\left[D'_{66}\left(\frac{\partial\phi'_\theta}{\partial Z}+\frac{\partial\phi'_Z}{\partial\theta}\right)\right]+\frac{\partial}{\partial Z}\left(D'_{12}\frac{\partial\phi'_\theta}{\partial\theta}+D'_{22}\frac{\partial\phi'_Z}{\partial Z}\right)=K_s A'_{44}\left(\phi'_Z+\frac{\partial W}{\partial Z}\right) \tag{3.33}$$

where,

$$A'_{44}=\frac{C}{p_a L^2}A_{44} \qquad A'_{55}=\frac{C}{p_a R^2}A_{55} \qquad \phi'_\theta=\frac{R}{C}\phi_x$$

$$\phi'_Z=\frac{L}{C}\phi_z \qquad D'_{11}=\frac{C}{p_a R^4}D_{11} \qquad D'_{12}=\frac{C}{p_a L^2 R^2}D_{12}$$

$$D'_{22}=\frac{C}{p_a L^4}D_{22} \qquad D'_{66}=\frac{C}{p_a L^2 R^2}D_{66} \tag{3.34}$$

ϕ'_θ and ϕ'_Z in Eqn. (3.34) denote rotation angles about the z and θ axes, respectively.

3.4.2.2. Discretization of the governing equation using finite element formulation

Now the above Eqns. (3.29-3.31) is discretized using the finite element method [94] integrating over a 2D finite element domain. A Linear element for SDT with three degrees of freedom (W,ϕ_θ,ϕ_Z) per node is shown in Fig. (3.12).

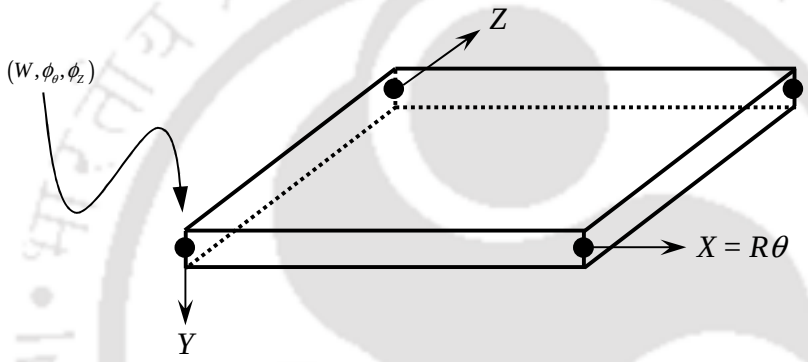

Fig. 3.12: Linear element for SDT with three degrees of freedom (W,ϕ_θ,ϕ_Z) per node

Now, assuming the finite element interpolation of W, ϕ_θ, and ϕ_Z in the form

$$W(\theta,Z,t)=\sum_{j=1}^{n}W_j(t)\psi_j^1(\theta,Z), \qquad \phi_\theta(\theta,Z,t)=\sum_{j=1}^{m}S_j^\theta(t)\psi_j^2(\theta,Z),$$

$$\phi_Z(\theta,Z,t)=\sum_{j=1}^{m}S_j^Z(t)\psi_j^2(\theta,Z), \qquad W(\theta,Z,t)=\{\psi^1\}^T\{W\}$$

$$\{\phi\}=\begin{Bmatrix}\phi_\theta\\ \phi_Z\end{Bmatrix}=\{\psi^2\}\{S\} \tag{3.35}$$

where, $\{\psi^1\}^T = \{\psi_1^1 \quad \psi_2^1 \quad \psi_3^1 \quad \psi_4^1\}$, $\{\psi^2\} = \begin{bmatrix} \psi_1^2 & 0 & \psi_2^2 & 0 & \psi_3^2 & 0 & \psi_4^2 & 0 \\ 0 & \psi_1^2 & 0 & \psi_2^2 & 0 & \psi_3^2 & 0 & \psi_4^2 \end{bmatrix}$

$$\{S\}^T = \{S_1^\theta \quad S_1^Z \quad S_2^\theta \quad S_2^Z \quad S_3^\theta \quad S_3^Z \quad S_4^\theta \quad S_4^Z\}, \quad \{W\}^T = \{w_1 \quad w_2 \quad w_3 \quad w_4\} \tag{3.36}$$

ψ_j^1 and ψ_j^2 are interpolation function used for w and (ϕ_θ, ϕ_Z), respectively. In general, ψ_j^1 and ψ_j^2 are polynomial of different degree. However, in the present study, we take $\psi_j^1 = \psi_j^1 = \psi$.

The domain is discretized as $(m+1)\times(n+1)$ for solving the Reynolds equation for calculating the hydrodynamic gas pressure using finite difference scheme. The same discretization of the domain is used for calculating the foil deflection using finite element method. A typical mesh is shown in Fig. (3.10). The finite element equation for an element in matrix form can be written as

$$[K_{SDT}^e]\{w_{SDT}^e\} = \{F_{SDT}^e\} \tag{3.37}$$

where, $[K_{SDT}^e]$ is the elemental stiffness matrix, $\{w_{SDT}^e\}$ is the vector of primary nodal variables or generalized displacements, and $\{F_{SDT}^e\}$ is the force vector. $\{w_{SDT}^e\}$ consists of the nodal foil deflections and the rotation of the transverse normal.

The elemental finite element equation Eqn. (3.37) can be written as

$$\begin{bmatrix} [K^{11}] & [K^{12}] \\ [K^{21}] & [K^{22}] \end{bmatrix} \begin{Bmatrix} \{W\} \\ \{S\} \end{Bmatrix} = \begin{Bmatrix} \{F^1\} \\ \{F^2\} \end{Bmatrix} \tag{3.38}$$

where, $\{W\}$ is the nodal foil deflections vector, $\{S\}$ is the rotation of the transverse normal and the components of the stiffness matrix are given by

$$\left[K^{11}\right]=\int_{\Omega_e}\left[B_1\right]^T\left[A\right]\left[B_1\right]d\mathbf{x},$$

$$\left[K^{12}\right]=\int_{\Omega_e}\left[B_1\right]^T\left[A\right]\left[\psi^2\right]d\mathbf{x}=\left[K^{21}\right]^T$$

$$\left[K^{22}\right]=\int_{\Omega_e}\left(\left[\psi^2\right]^T\left[A\right]\left[\psi^2\right]+\left[B\right]^T\left[C\right]\left[B\right]\right)d\mathbf{x} \tag{3.39}$$

$$\left[B_1\right]=\begin{bmatrix}\frac{\psi_1^1}{\partial\theta} & \frac{\psi_2^1}{\partial\theta} & \frac{\psi_3^1}{\partial\theta} & \frac{\psi_4^1}{\partial\theta}\\ \frac{\psi_1^1}{\partial Z} & \frac{\psi_2^1}{\partial Z} & \frac{\psi_3^1}{\partial Z} & \frac{\psi_4^1}{\partial Z}\end{bmatrix}_{(2\times4)} ;\ \left[B\right]=\begin{bmatrix}\frac{\partial\psi_1^2}{\partial\theta} & 0 & \frac{\partial\psi_2^2}{\partial\theta} & 0 & \cdots & \frac{\partial\psi_m^2}{\partial\theta} & 0\\ 0 & \frac{\partial\psi_1^2}{\partial Z} & 0 & \frac{\partial\psi_2^2}{\partial Z} & \cdots & 0 & \frac{\partial\psi_m^2}{\partial Z}\\ \frac{\partial\psi_1^2}{\partial Z} & \frac{\partial\psi_1^2}{\partial\theta} & \frac{\partial\psi_2^2}{\partial Z} & \frac{\partial\psi_2^2}{\partial\theta} & \cdots & \frac{\partial\psi_m^2}{\partial Z} & \frac{\partial\psi_m^2}{\partial\theta}\end{bmatrix} \tag{3.40}$$

The component of the of the load vector are $\{F^1\}$ and $\{F^2\}$. $\{F^1\}$ is the force generated due to the hydrodynamic gas pressure and $\{F^2\}$ is the load due to moments. The calculation of $\{F^1\}$ is explained in the next section. Due to the absence of any moments $\{F^2\}$ is zero in this case.

3.4.2.3. Calculation of load vector from the pressure obtained from Reynolds equation

The Reynolds equation (Eqn. 2.6) is solved for calculating the nodal hydrodynamic gas pressure using finite difference scheme. Suppose $P_{i,j}$, $P_{i,j+1}$, $P_{i+1,j+1}$, $P_{i+1,j}$ are the nodal non-dimensionalized hydrodynamic gas pressure for $(i,j)^{th}$, $(i, j+1)^{th}$, $(i+1, j+1)^{th}$ and $(i+1, j)^{th}$ nodes respectively (shown in Fig. 3.10) calculated by solving Reynolds equation using finite difference scheme. A finite element showing the nodal hydrodynamic gas pressure obtained by solving Reynolds equation is shown in Fig. (3.13). The nodal force in the finite element model due to this nodal hydrodynamic gas pressure for an element with nodes i^{th} and $(i+1)^{th}$ is calculated using Eqn. (3.41). Pressure at point on the domain is calculated as

$$P = N_1' P_{i,j} + N_2' P_{i,j+12} + N_3' P_{i+1,j+1} + N_4' P_{i+1,j} \tag{3.41}$$

where N_1', N_2', N_3', N_4' are the shape functions for nodes $(i,j)^{th}$, $(i, j+1)^{th}$, $(i+1, j+1)^{th}$ and $(i+1, j)^{th}$ nodes respectively and $(i,j)^{th}$, $(i, j+1)^{th}$, $(i+1, j+1)^{th}$ and $(i+1, j)^{th}$ nodes constitutes a four-noded quadrilateral elements.

Now $\{F^1\}$ is calculated as

$$\{F^1\} = \int_{\Psi} P \left\{\psi^1\right\} d\Psi \tag{3.42}$$

where $\{\psi^1\}^T = \{\psi_1^1 \quad \psi_2^1 \quad \psi_3^1 \quad \psi_4^1\}$ is the shape functions of a four noded quadrilateral element.

3.4.2.4 Coupling of FE solution with the FDM solution

As discussed in earlier Section (3.3.3), the nodal foil deflection calculated using finite element method is used in Eqn. (2.7) to calculate the non-dimensional film thickness. This non-dimensional film thickness is used in Eqn. (2.6) to calculate the hydrodynamics gas pressure. The solution of Reynolds equation (Eqn. 2.6) is straightforward and the flow chart for the prediction of the performance characteristic of GFBs is shown in Fig. (2.4).

3.5. Summary

This chapter expounds the description of different GFBs numerical foil structural models namely the simple elastic foundation, 1D beam model, 2D CPT model and 2D SDT model. Three finite element models have been introduced for the top foil elastic structure. Firstly, the simplest FE model which assumes the top foil as a 1D beam with negligible deflections along the axial coordinate, i.e. infinite stiffness and acted upon by a uniformly distributed pressure field. Secondly, two 2D FE model, 2D CPT and 2D SDT models respectively, which takes the top foil as a flat plate with anisotropic material properties. The underlying bumps as described in

Sections (3.3) and (3.4) were modeled as a uniform elastic foundation along the edge of a typical finite element representing the top foil and are directly integrated into a global stiffness matrix that relates the top foil (and bumps) deflections produced by the gas film pressure or contact pressure, depending on the operating condition.

Chapter 4

STEADY STATE CHARACTERISTICS OF GFBs

4.1. Introduction

Preview of GFBs and basic equations have been provided in Chapter 2. Different numerical foil models, viz., simpel model, 1D model, 2D CPT model and 2D SDT model have also been presented in Chapter 3. The present scheme is validated by comparing present results with some published results in this chapter. The validation has been followed up by presentation of the steady state characteristics of GFBs for different foil structure models.

4.2. Methodology

As discuss in Sections (2.4, 2.5 and2.6), the steady state characteristics of the gas foil bearings (GFBs) are obtained by solving the steady state Reynolds equation (Eqn. 2.6) in a finite difference grid. Since the finite difference equation is a non-linear equation, therefore, the Newton-Raphson method is utilized to estimate the pressure distribution. Once the pressure distribution is obtained, the steady state characteristics of the GFBs can be determined.

The non-dimensional horizontal and vertical steady state load components are obtained by the following Eqn. (2.9).

$$\bar{W}_X = -\int_{-L/D}^{L/D}\int_{0}^{2\pi} P\cos\theta d\theta dZ$$

$$\bar{W}_Y = \int_{-L/D}^{L/D}\int_{0}^{2\pi} P\sin\theta d\theta dZ$$

For numerical integration, the Simpson's one third rule has been used.

Finally the total non-dimensional load is given by Eqn. (2.10)

$$\bar{W} = \sqrt{\bar{W}_X{}^2 + \bar{W}_Y{}^2}$$

For steady state equilibrium condition, the horizontal load component should become zero theoretically, however, in actual numerical solution it is not exactly zero but negligible. Initially an attitude angle is assumed for a given eccentricity ratio and the assumed attitude angle is varied till the horizontal load component approximately becomes zero.

A matlab computational code has been developed for GFBs computational analysis by integrating the finite element top foil structural models. Grid independent result has been generated to ascertain various parametric studies. The finite element models vis-à-vis 1D beam model, 2D CPT model and 2D SDT model uses a mesh size of 104x16 elements in the circumferential and axial directions respectively and the same mesh is used for the finite difference numerical scheme to solve the Reynolds equation for calculating the hydrodynamic gas film pressure. While, on the other hand, the simple foil structure model uses a mesh of 90x10 elements in the circumferential and axial directions respectively, to analyze the gas film pressure. All the computational

analysis has been performed off-line in a computational laboratory.

The GFBs with 2D foil model has 5355 degrees of freedom (DOF), the 1D model has 3570 degrees of freedom. In the simple elastic model, however the nodal displacement is simply a scalar multiplication of the nodal pressure.

4.3. Validation

4.3.1. Comparison with published theoretical results

The validity of the present analysis and the computational program are assessed by comparison of the steady state results with the published data available in the literature.

The present steady state load carrying capacity ($\bar{W}$) and the attitude angle (ϕ) have been compared with the published theoretical results as shown in Table (4.1) and Table (4.2). The results have been equated for L/D=1.0 and S=0 with Yang et al, [94] as shown in Table (4.1) for different values of eccentricity ratios (ε) and bearing number (Λ). The GFBs reduce to ordinary gas bearings when S=0, i.e., when compliance coefficient is zero.

Table (4.2) shows the comparison of the steady state load capacity ($\bar{W}$) and attitude angle (ϕ) for L/D=1.0, Λ=1 for S=0 and S=1 with the published results of Heshmat et al. [9] and Peng and Carpino [16]

Table 4.1: Steady state characteristics for *L/D*=1.0, *S*=0

Λ	ε	ϕ	ϕ (*ref*)	$\bar{W}$	$\bar{W}$ (*ref*)
0.6	0.2	79.639	#79.080	0.18.05	#0.1806
0.6	0.4	74.171	#74.020	0.4050	#0.4020
0.6	0.6	61.768	#61.450	0.7540	#0.7555
3.0	0.2	48.020	#47.730	0.7097	#0.6916
3.0	0.4	40.951	#40.690	1.5340	#1.5230
3.0	0.6	30.520	#30.040	2.870	#2.8631

Yang et al. [93]

Table 4.2: Steady state characteristics for *L/D*=1.0, Λ=1.0

S	ε	ϕ	ϕ(*ref*)	ϕ(*ref*)	$\bar{W}$	$\bar{W}$(*ref*)	$\bar{W}$(*ref*)
0	0.6	35.90	#35.70	*36.50	0.964	#0.951	*0.961
0	0.75	24.51	#24.10	*24.70	1.926	#1.894	*1.922
0	0.9	12.69	#12.80	*12.90	5.150	#5.055	*5.073
1	0.6	35.94	#32.10	*34.00	0.5489	#0.568	*0.567
1	0.75	29.55	#26.30	*27.70	0.7523	#0.783	*0.778
1	0.9	24.24	#21.40	*22.40	0.9882	#1.020	*1.020

Heshmat et al. [9] *Peng and Carpino [16]

4.3.2. Comparison with published experimental results

The minimum film thickness and the attitude angle are compared with the experimental results available in Ruscitto et al. [97]. Table 4.3 provides the geometry and the operating conditions for the test GFB in Ruscitto et al. [97].

Table 4.3: Geometry and operating conditions of GFB in Ruscitto et al. [97]

Bearing radius, $R=D/2$	19.05 mm
Bearing length, L	38.1 mm
Bearing radial clearance, C	20 μm
Top foil thickness t_t	101.6 μm
Bump foil thickness, t_b	101.6 μm
Bump pitch, s	4.572 mm
Half bump length, l_0	1.778 mm
Bump foil Young's modulus, E_b	214 GPa
Top foil Young's modulus, E_t	214 GPa
Bump foil Poisson's ratio, υ	0.29
Operating conditions	
Atmospheric pressure, p_a	10^5 N/ m^2
Gas viscosity, μ	2.98×10^{-5} N-s/ m^2

4.3.2.1. Attitude angle versus applied static load

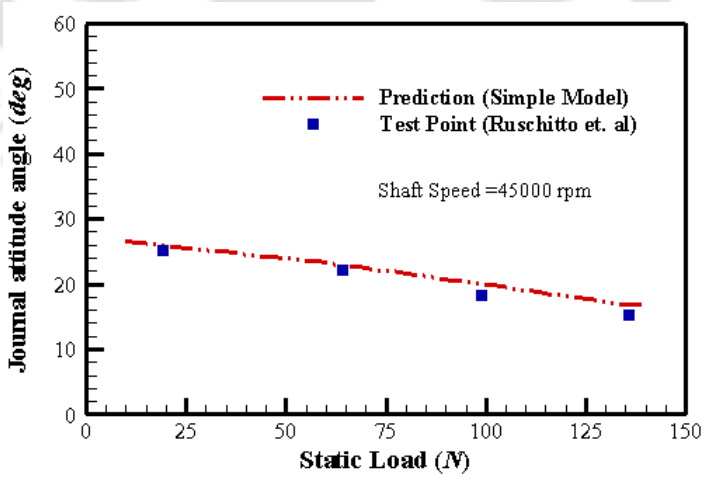

Fig. 4.1. Journal attitude angle Vs. static load for shaft speed of 45,000 rpm

Figure 4.1 presents the attitude angle versus static load for operation of shaft speeds 45,000 rpm. It has been observed that the present results overestimate the attitude angles by 2% to 6% with the experimental results for shaft speeds 45,000 rpm.

4.3.2.2. Minimum flim thickness versus applied static load

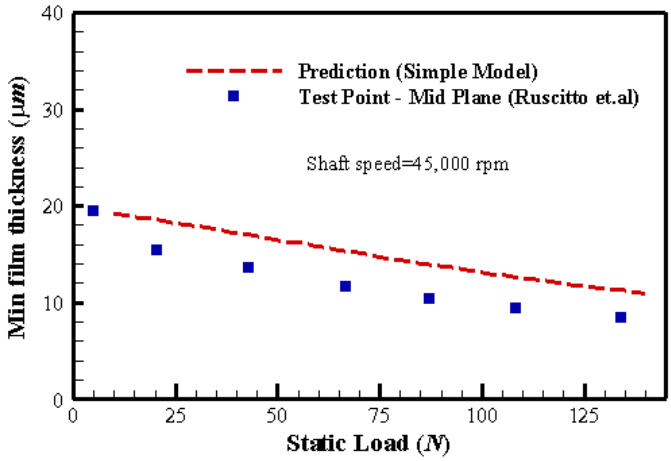

Fig. 4.2. Minimum flim thickness Vs. static load for shaft speed of 45,000 rpm

Figure 4.2 presents the minimum film thickness versus applied static load for operation of shaft speeds at 45,000 rpm. It has been observed that the present results overestimate the minimum film thickness by 0% to 25% with the experimental results for shaft speeds at 45,000 rpm

It has been observed from the comparisons of steady state characteristics in Tables (4.1) and (4.2) and experimental results in Figs. (4.1) and (4.2) that the present results are in good agreement with the published results. Therefore, the computational model to carry out the proposed analysis has been considered to be valid.

4.4. Steady State Characteristics

The steady state performance characteristics of GFB have been determined using the procedure and the solution methods described in Section (4.2). The steady state results for simple model, 1D model, 2D CPT (classical plate theory) model and 2D SDT (shear deformation theory) model have been investigated and presented.

4.4.1. Pressure Distribution, Film Thickness and Top Foil Deflection

Figures (4.3) to (4.14) represents the non-dimensional pressure distribution, the film thickness and top foil deflection for a typical GFBs with simple foil structure model, 1D model, 2D CPT model and 2D SDT models respectively for ε = 0.6, L/D=1, S=1, Λ=1. The surface of journal moves from the left to right in the direction of increasing θ. The maximum pressure occurs in the bearing center with pressure becoming ambient at both sides as shown in Figs. (4.3), (4.6), (4.9) and (4.12). And under the action of this pressure, the foil structure is deflected as shown in Figs. (4.5), (4.8), (4.11) and (4.14) and corresponding film thickness profile has been shown in Figs. (4.4), (4.7), (4.10) and (4.13) respectively for all foil structure models of the GFBs.

It has been observed from Figs. (4.3 to 4.5) for GFBs with simple foil structure model that the maximum value of averaged non-dimensional pressure is 1.2536,

(Fig. 4.3) where at the same point maximum deflection (Fig. 4.5) of the top foil takes place and has its maximum value of 0.2536. The non-dimensional minimum film thickness (Fig. 4.4) is 0.4001 which occurs at 215^0 from the fixed end of the top foil.

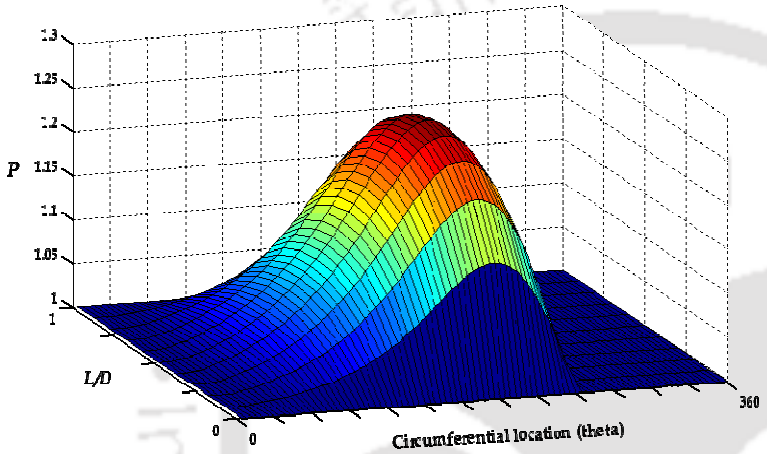

Fig. 4.3: Pressure distribution of GFBs with simple foil structure model for ε = 0.6, L/D=1, S=1, Λ=1

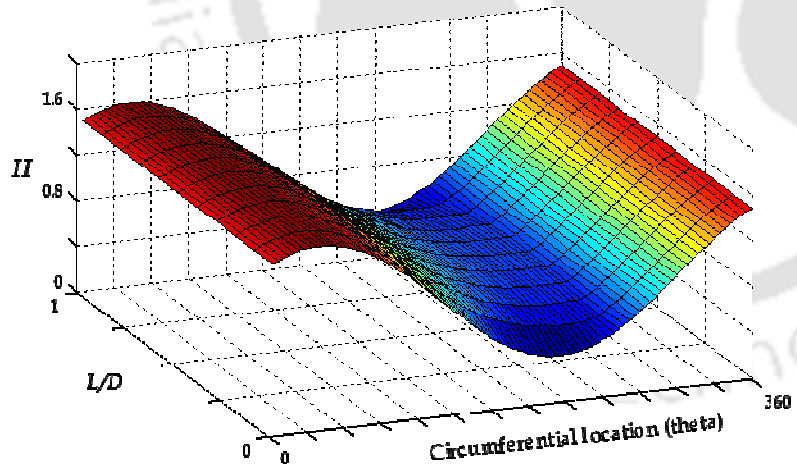

Fig. 4.4: Flim thickness of GFBs with simple foil structure model for ε = 0.6, L/D=1, S=1, Λ=1

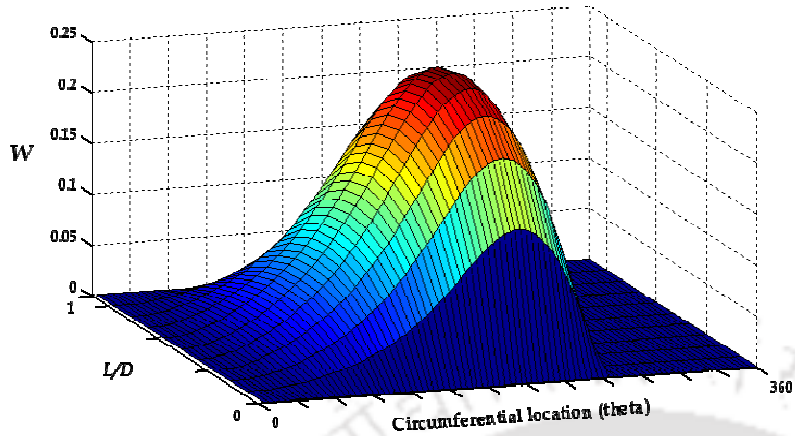

Fig. 4.5: Top foil deflection of GFBs with simple foil structure model for ε = 0.6, L/D=1, S=1, Λ=1

Figs. (4.6 to 4.8) also presents the non-dimensional pressure distribution, non-dimensional minimum film thickness and non-dimensional top foil deflection for GFBs with 1D foil structure model. It has been observed from the figures the that the maximum value of averaged non-dimensional pressure is 1.2544 (Fig.4.6), where at the same point the maximum deflection of the top foil (Fig. 4.8) takes place and its maximum value is 0.2538. The non-dimensional minimum film thickness (Fig. 4.7) value is 0.4001 which occurs at 215.39^0 from the fixed end of the top foil.

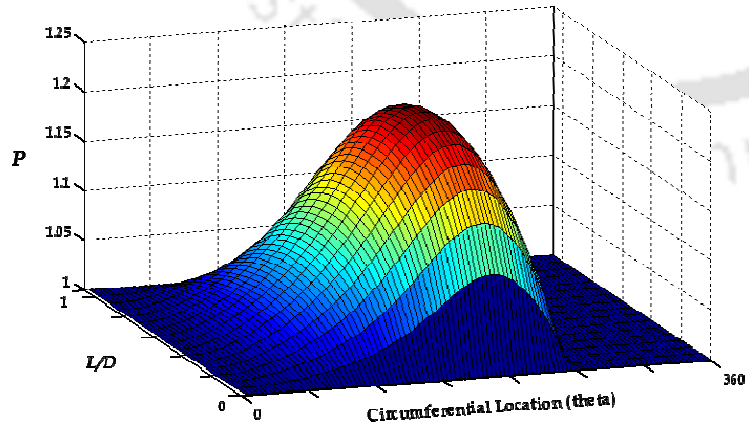

Fig. 4.6: Pressure distribution of GFBs with 1D foil structure model for ε = 0.6, L/D=1, S=1, Λ=1

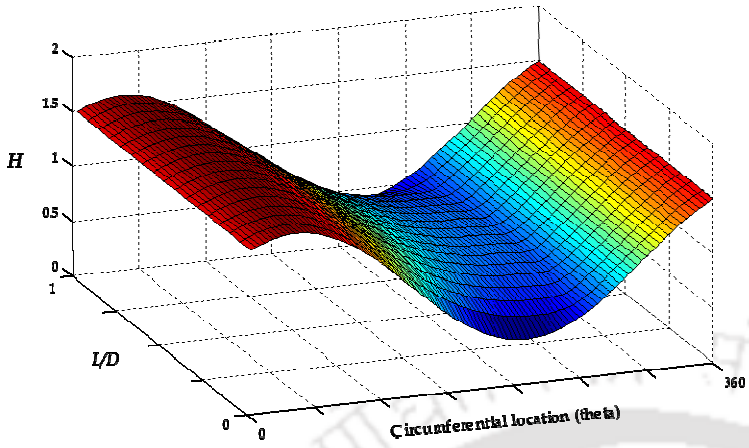

Fig. 4.7: Flim thickness of GFBs with 1D foil structure model for $\mathcal{E}$ = 0.6, *L/D*=1, *S*=1, Λ=1

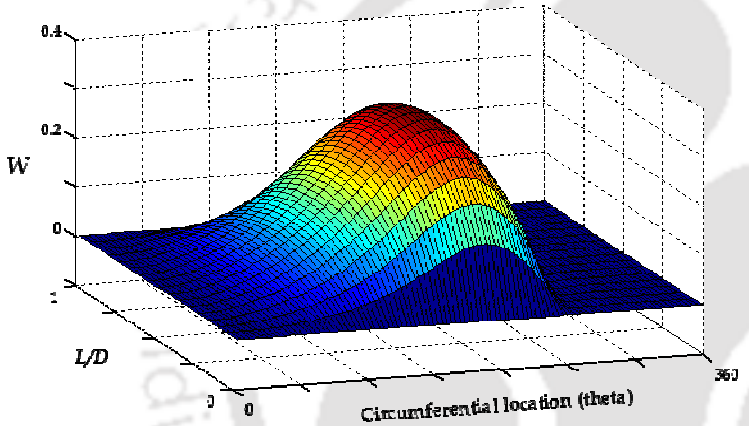

Fig. 4.8: Top foil deflection of GFBs with 1D foil structure model for $\mathcal{E}$ = 0.6, *L/D*=1, *S*=1, Λ=1

It has been observed from the Figs. (4.9, to 4.11) for GFBs with 2D CPT foil structure model that the maximum value of averaged non-dimensional pressure is 1.2556 (Fig. 4.9), where at the same point the maximum deflection of the top foil (Fig. 4.11) takes place which has its maximum value of 0.2575. The non-dimensional minimum film thickness (Fig. 4.10) value is 0.4467 which occurs at 215.74^0 from the fixed end of the top foil.

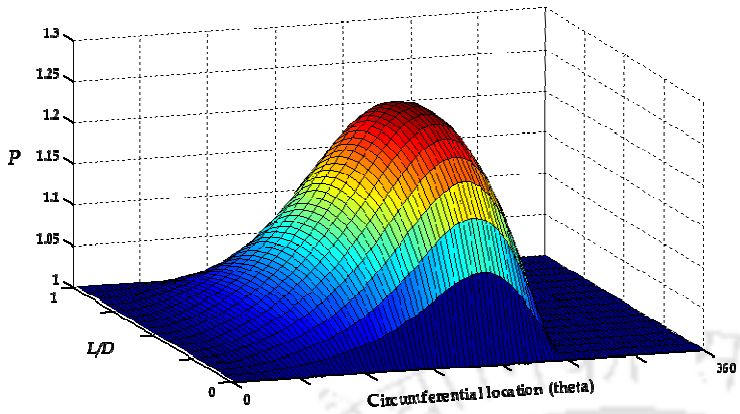

Fig. 4.9: Pressure distribution of GFBs with 2D CPT foil structure model for $\mathcal{E}$ = 0.6, *L/D*=1, *S*=1, Λ=1

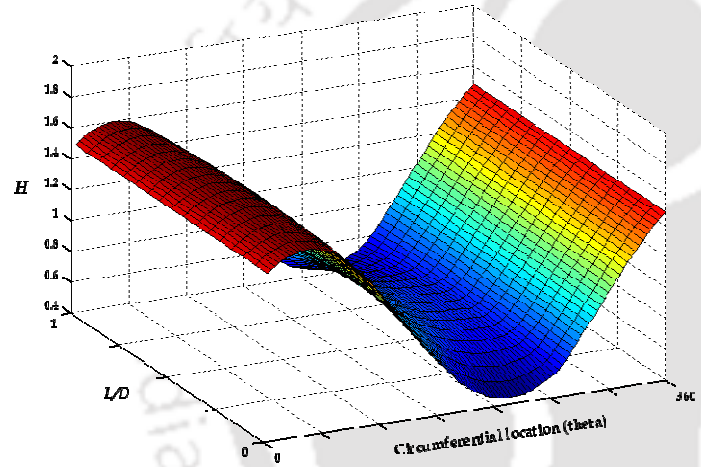

Fig. 4.10: Flim thickness of GFBs with 2D CPT foil structure model for $\mathcal{E}$ = 0.6, *L/D*=1, *S*=1, Λ=1

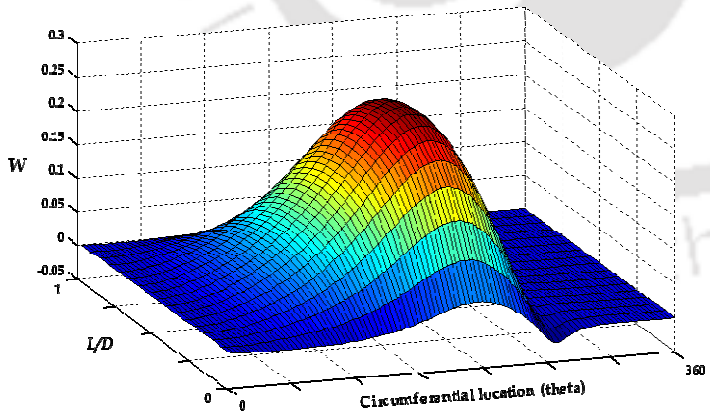

Fig. 4.11: Top foil deflection of GFBs with 2D CPT foil structure model for $\mathcal{E}$ = 0.6, *L/D*=1, *S*=1, Λ=1

Figs. (4.12 to 4.14) presents the non-dimensional pressure distribution, non-dimensional minimum film thickness and non-dimensional top foil deflection for

GFBs with 2D SDT foil structure model. It has been observed from the figures that the maximum value of averaged non-dimensional pressure is 1.2853 (Fig.4.12), where at the same point maximum deflection of the top foil (Fig. 4.14) takes place and its maximum value is 0.2385. The non-dimensional minimum film thickness (Fig. 4.13) value is 0.4555 which occurs at 217.5657^0 from the fixed end of the top foil

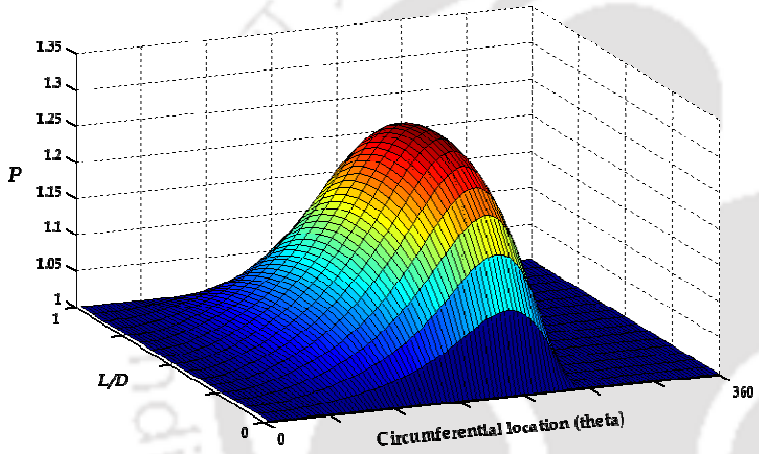

Fig. 4.12: Pressure distribution of GFBs with 2D SDT foil structure model for ε = 0.6, L/D=1, S=1, Λ=1

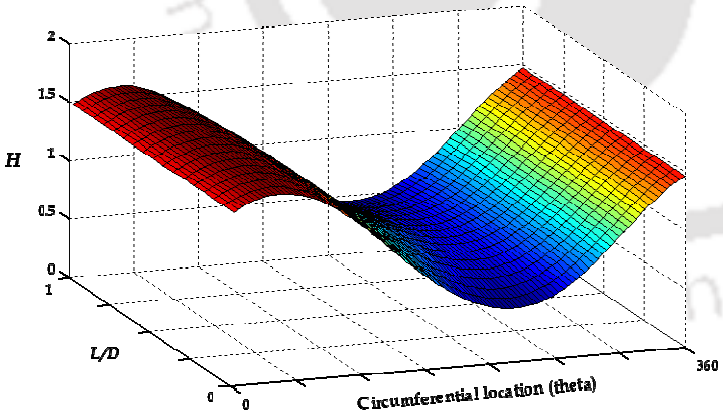

Fig. 4.13: Flim thickness of GFBs with 2D SDT foil structure model for ε = 0.6, L/D=1, S=1, Λ=1

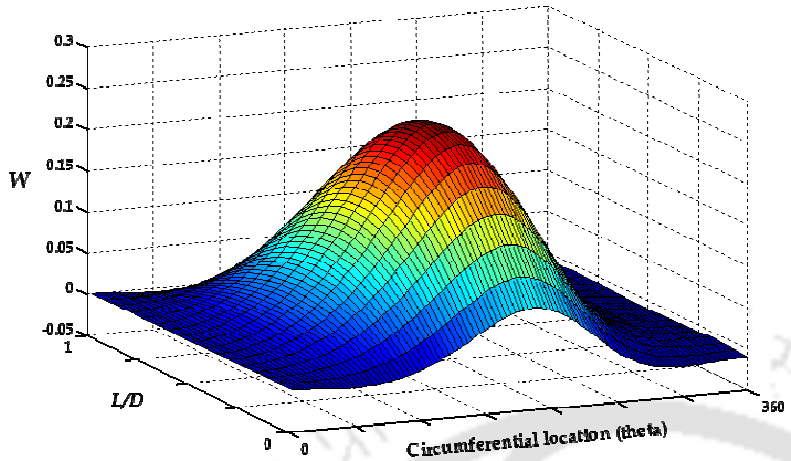

Fig. 4.14: Top foil deflection of GFBs with 2D SDT foil structure model for $\mathcal{E}$ = 0.6, *L/D*=1, *S*=1, Λ=1

4.4.2. Load carrying capacity of GFBs for different top foil models

Figure (4.15) shows the load carrying capacity ($\bar{W}$) with respect to eccentricity ratio for all considered models of the foil structure of GFBs.

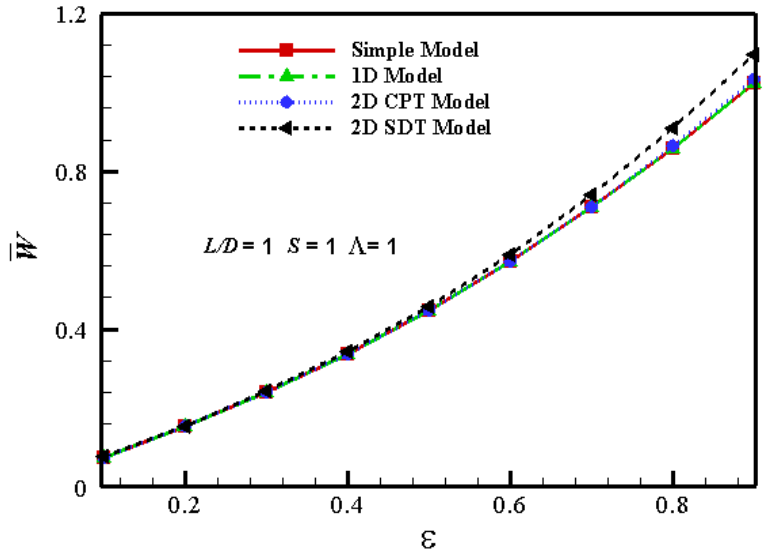

Fig. 4.15: Effect of eccentricity ratio (ε) on the load carrying capacity ($\bar{W}$) of GFB for different top foil models

It has been observed that for all foil models of the GFBs, the non-dimensional load capacity **($\bar{W}$)** increases as the eccentricity ratio increases. The increase in the load

capacity, however, does not have much disparities at lower values of eccentricity ratio **(ε),** nevertheless as the eccentricity ratio increase GFBs with 2D SDT foil model predicts a trivial increase, approximately 7% at 0.9 eccentricity ratio, compared to other top foil models of GFBs. Therefore it has been observed that at higher eccentricity ratio (beyond ε=0.6) GFBs with 2D SDT foil model predicts higher load carrying capacity as compared to all other foil models. This may be attributed to the reason that the 2D SDT foil model formulation incorporates both shearing and bending effects, whereas other models do not include shearing effect in particular.

4.4.3. Effect of bearing number on the load carrying capacity of GFBs for different top foil models

The effect of bearing number **(Λ)** on the load carrying capacity **($\bar{W}$)** of GFBs with different top foil structure models have been presented in Fig. (4.16).

It has been observed that with the increase in bearing number **(Λ),** the load carrying capacity **($\bar{W}$)** increases for all the foil models of GFBs. The increase is more or less identical for the simple model, 1D model and 2D CPT model respectively as seen from the plot; however GFB with 2D SDT foil model displays a higher load capacity compared to all other foil models. It has been observed that there is an increase of approximately 28% (at bearing number, Λ=10) in the load carrying capacity for 2D SDT foil model as compared to other foil models of GFBs

with similar bearing configuration. As mentioned in the previous section, 2D SDT model is the best model for prediction of steady state characteristics as it incorporates both shearing and bending effects.

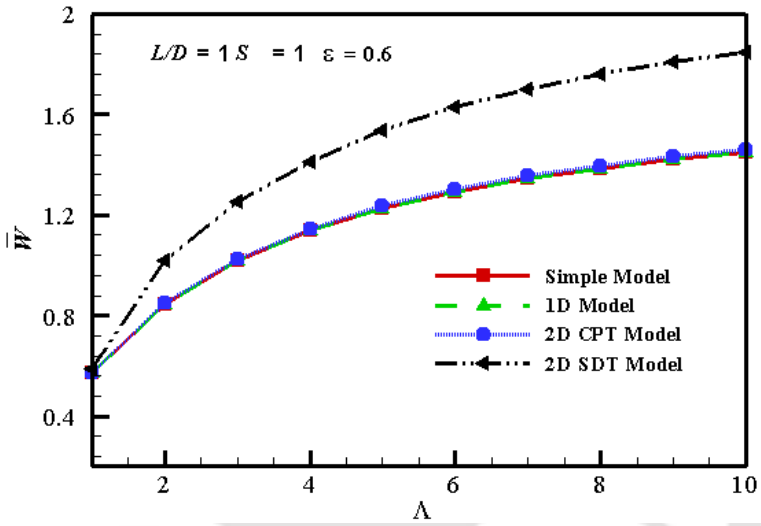

Fig. 4.16: Effect of bearing number (Λ) on the load carrying capacity ($\bar{W}$) of GFB for different top foil models

4.4.4. Attitude angle of GFB for different top foil model

Figure (4.17) depicts the variation of attitude angle **(ϕ)** with respect to eccentricity ratio of GFBs for all foil model i.e. simple model, 1D model, 2D CPT model and 2D SDT model.

As small attitude angles are a desirable features in GFBs since they denote a journal displacement parallel to the load direction, it has been apparent from Fig. (4.17) that with an increase in eccentricity ratio, the attitude angle decreases for all

the foil models of GFBs, with 2D SDT foil model displaying a slightly larger attitude angle as compared to other foil models of GFBs.

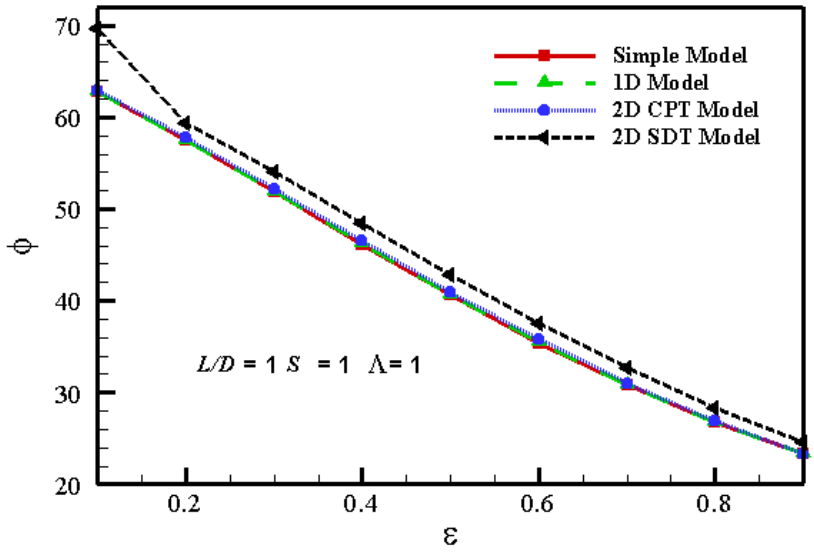

Fig. 4.17: Effect of eccentricity ratio (ε) on the attitude angle (ϕ) of GFB for different top foil model

4.4.5. Effect of compliance coefficient on the load carrying capacity of GFBs

Figure (4.18) portrays the dependency of load carrying capacity **($\bar{W}$)** on the bump compliance coefficient (S) for all the foil models of GFBs. It has been observed that the higher the values of compliance coefficient lower is the load carrying capacity of the GFBs. As the compliance coefficient varies, GFBs with 2D SDT foil model predicts higher load carrying capacity compared to other foil models with similar bearing configuration. GFB with simple foil model predicts the least load capacity compared to all other foil models. The lower load capacity of GFBs with simple

foil model with respect to compliance coefficient can be attributed to the simplicity in its foil design which does not incorporate any effect of bending and shear. Therefore it has been inferred that for all the foil models of GFBs the compliance coefficient (S) of the foils should be as low as possible to achieve a higher load carrying capacity but limiting to S=0 which is the value for a plain gas bearing (GBs). It is worth mentioning that a plain gas bearings (GBs) has much higher load carrying capacity than the GFBs with similar bearing configuration.

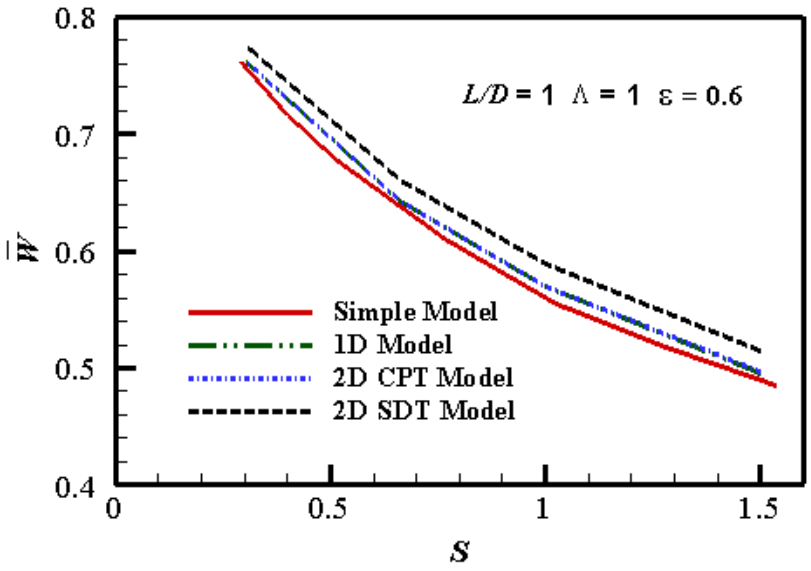

Fig. 4.18: Effect of compliance coefficient (S) on the load carrying capacity ($\bar{W}$) of GFB

4.5. Summary

In this chapter, the present computational scheme has been validated by comparing the present results with some published results. The steady state characteristics of GFBs for all the foil structural models namely the simple model,

the 1D model, the 2D CPT model and the 2D SDT model have been investigated under similar bearing configuration and the results have been presented. The effect of various non-dimensional parameters on the static characteristics of GFBs have been determined and predicted for different foil structure models of GFBs.

The stability analysis of rotor-bearing system by considering a rigid rotor supported on two symmetrical hydrodynamic gas foil bearing have been presented in the forthcoming chapter.

Chapter 5

STABALITY ANALYSIS OF GAS FOIL JOURNAL BEARING

5.1. Introduction

The steady state characteristics of the gas foil bearings (GFBs) with different foil structure models have been discussed in the previous chapter. This chapter presents the stability analysis of a fully balanced rigid rotor supported on two symmetrical gas foil journal bearings by using a non-linear time transient method. This analysis enables to trace the journal centre trajectories at different locations of the rotor and thereby estimates the critical mass parameter (a measure of stability) which is a function of speed. Several trajectories of the journal centre have been obtained and the stability curves have been drawn for different rotor-bearing parameters.

5.2. Stability Analysis

The stability analysis can be done in any one of the following ways:

- Linearized stability analysis.
- Non-linear transient analysis.

In the first method, it is assumed that the journal whirls about the mean steady state position and considering only the first order perturbation, pressure and film thickness are expressed. A set of equations, both steady-state and dynamic, are

found on substitution of the pressure and film thickness expressions in the governing Reynolds equation. Only the first order terms are retained whereas the higher order terms are neglected. Eight stiffness and damping coefficients are estimated from the resulting differential equations and these coefficients are used to determine the mass parameter (a measure of stability) by solving the equations of motion of the rotor. The critical mass parameter is a function of spin speed and is the threshold of stability. The linear theory, however, does not give any information on the journal motion once the instability sets in. Therefore, this theory does not provide post whirl orbit details. Although linear analysis for the estimation of dynamic coefficients and stability analysis is relatively easy to apply, it is sometimes criticized because it utilizes linearized film coefficients, which are only valid for small displacements of the journal from its initial static equilibrium position. Since whirl implies large amplitude of vibration, it may be argued that any analysis based upon an assumption of small amplitudes of vibration is invalid. For this reason, where resources permit, a different approach to whirl instability analysis, which does not assume a linear film, is preferred. The non-linear transient analysis, however, removes these shortcomings.

5.3. Non-linear Transient Stability Analysis

A non-linear time transient stability analysis has been carried out for a rigid rotor supported on two identical hydrodynamic gas foil journal bearings (Fig. 2.4) in the present study. Following the methods discussed in chapter 2 (Section 2.7) a

number of trajectories have been obtained for different mass parameters keeping other rotor-bearing parameters constant. Initially the journal centre equilibrium position is displaced from its static equilibrium position and the equations of motion are solved using 4th order Runge-Kutta method (described in chapter 2) at small time intervals to estimate the new position of the journal centre at every time step. In this way the journal centre trajectory is traced to study the stability behavior. A bearing is considered unstable if this trajectory grows continuously, tending to reach the clearance circle. However if the trajectory spirals in and regains the static equilibrium position, then the bearing is said to be stable. If the journal centre trajectory traverses over a loop, the bearing is said to be in a critically stable condition. This process is repeated for a number of times for different values of mass parameter ($\bar{M}$) until critically stable trajectories are obtained.

By observing the trajectories it has been witnessed that, above a certain value of mass parameter there is a transition in rotor motion from stable to unstable state. This value is called the critical mass parameter ($\bar{M}$). Though many such trajectories for different operating conditions are plotted, here only few representative plots are presented to save space. Figures (5.1) to (5.12) shows the stable, critically stable and unstable conditions of the motion trajectory of the rotor for all the foil structure models of GFBs respectively vis-à-vis simple model, 1D model, 2D CPT model and 2D SDT model. Considering the simple foil model of

the GFBs it has been observed that for $\bar{M}$ =9.0 the system remains stable (Fig. 5.1) and at $\bar{M}$ =16.9 the journal centre traverses in a loop indicating the critical state (Fig. 5.2). And at $\bar{M}$ =18 (Fig. 5.3) the system at unstable condition is shown. Similarly, the stable, critically stable and unstable conditions of GFBs for 1D model, 2D CPT model and 2D SDT model of the foil structure have been presented from Figs. (5.4) to (5.12). As mentioned above numbers of trajectories have been obtained determining different values of critical mass parameter ($\bar{M}$) at different eccentricity ratio (ε), bearing number (Λ) and compliance coefficient (S) and subsequently stability maps are plotted. These are discussed in the following sections.

(1). Simple Elastic Model

Stable

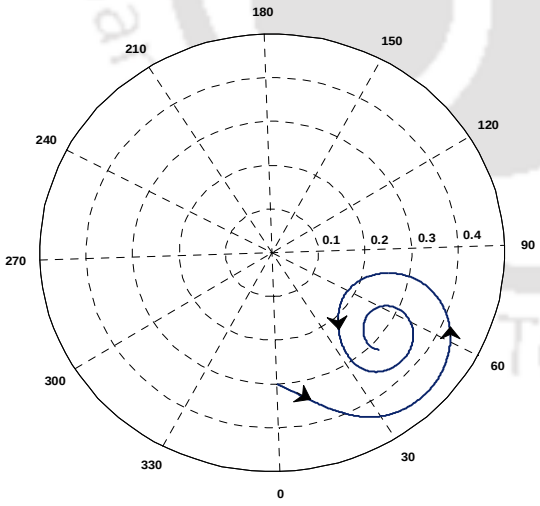

Fig. 5.1: Trajectory of journal centre for simple model for L/D=1, ε =0.3, S=1, Λ =1, $\bar{M}$ =9

Critically stable

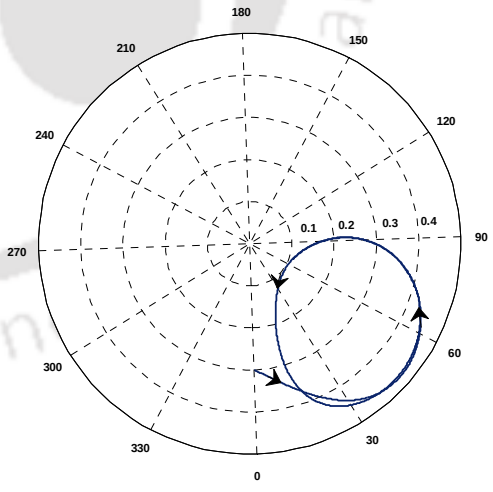

Fig. 5.2: Trajectory of journal centre for simple model for L/D=1, ε =0.3, S=1, Λ =1, $\bar{M}$ =16.9

Unstable

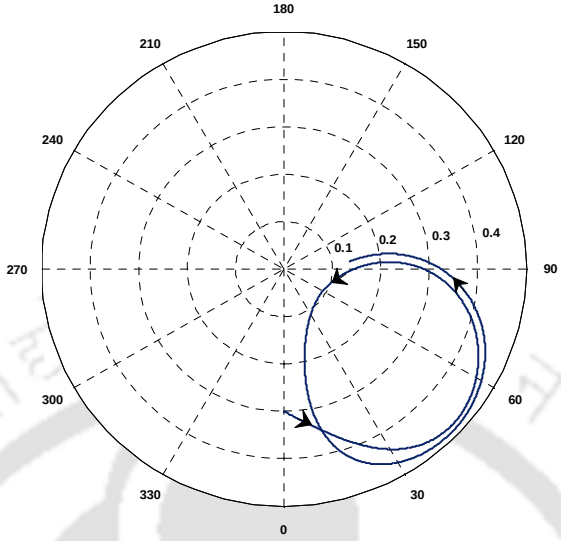

Fig. 5.3: Trajectory of journal centre for simple model for L/D=1, ε =0.3, S=1, Λ =1, $\bar{M}$ =18

(2).1D Model

Stable

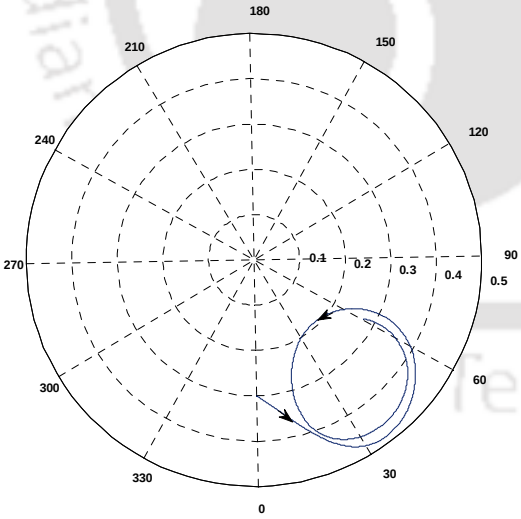

Fig. 5.4: Trajectory of journal centre for 1D model for L/D=1, ε =0.3, S=1, Λ =1, $\bar{M}$ =12

Critically stable

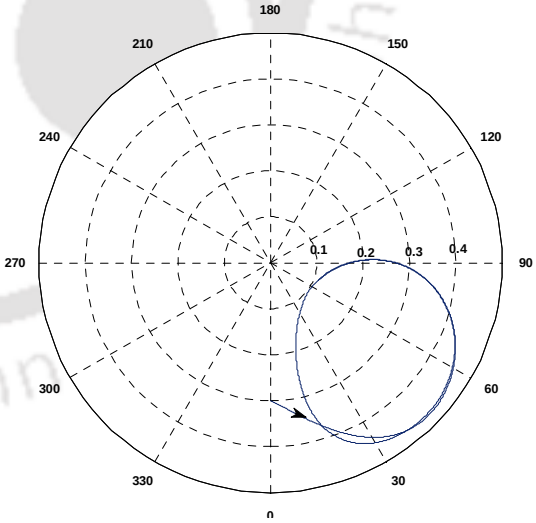

Fig 5.5: Trajectory of journal centre 1D model for L/D=1, ε =0.3, S=1, Λ =1, $\bar{M}$ =14.8

Unstable

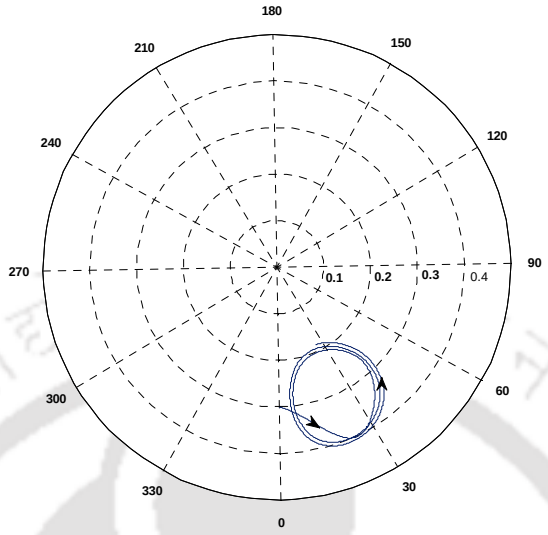

Fig 5.6: Trajectory of journal centre for 1D model for L/D=1, ε =0.3, S=1, Λ =1, $\bar{M}$ =16.4

(3). **2D CPT Model**

Stable

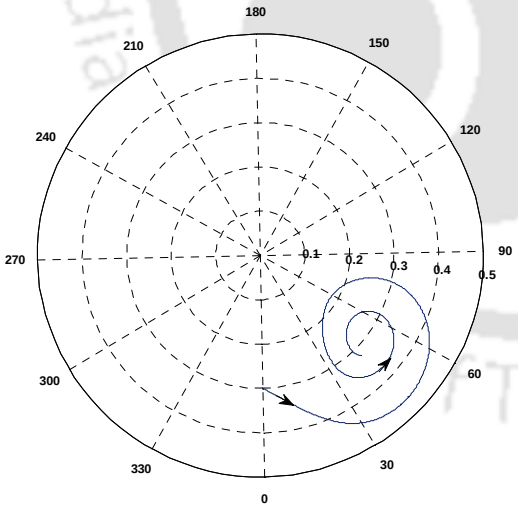

Fig. 5.7: Trajectory of journal centre for 2D CPT model for L/D=1, ε =0.2, S=1, Λ =1, $\bar{M}$ =8

Critically Stable

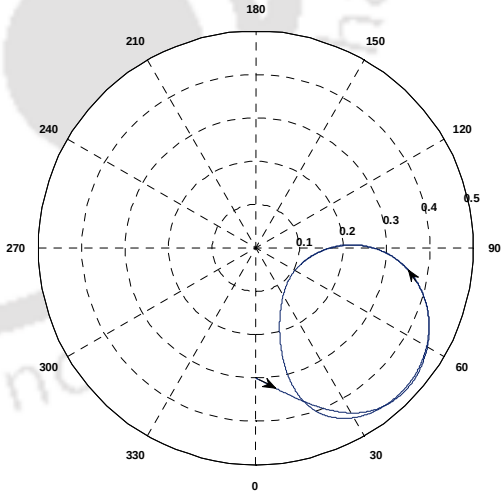

Fig. 5.8: Trajectory of journal centre for 2D CPT model for L/D=1, ε =0.2, S=1, Λ =1, $\bar{M}$ =12.4

Unstable

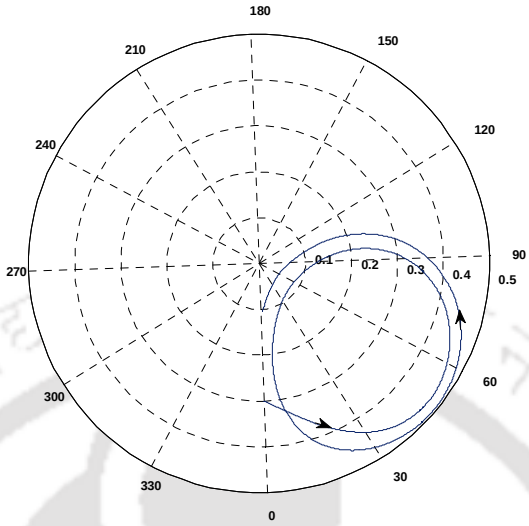

Fig. 5.9: Trajectory of journal centre for 2D CPT model for *L/D*=1, ε =0.2, *S*=1, Λ =1, $\bar{M}$ =14.5

(4). 2D SDT Model

Stable

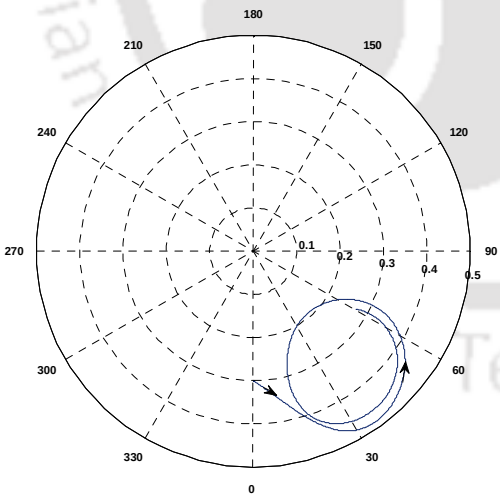

Fig. 5.10: Trajectory of journal centre for 2D SDT model for *L/D*=1, ε =0.3, *S*=1, Λ =1, $\bar{M}$ =10

Critically Stable

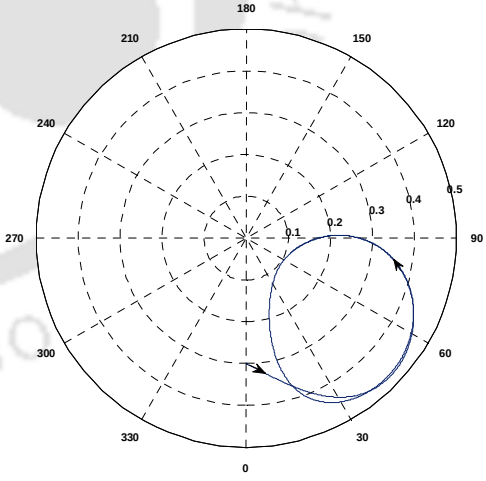

Fig. 5.11: Trajectory of journal centre for 2D SDT model for *L/D*=1, ε =0.3, *S*=1, Λ =1, $\bar{M}$ =11.3

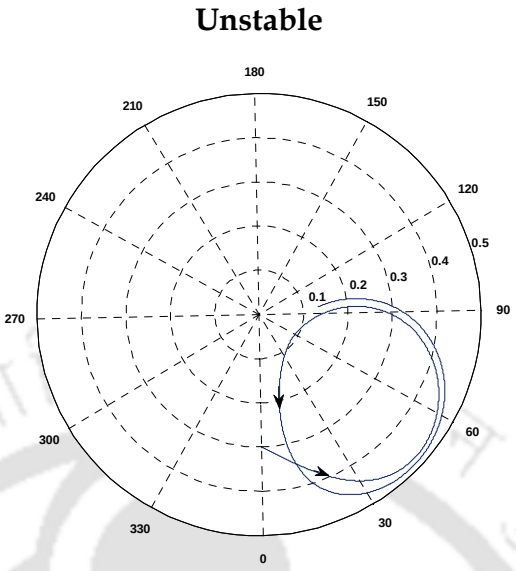

Fig. 5.12: Trajectory of journal centre for for 2D SDT model *L/D*=1, ε =0.3, *S*=1, Λ =1, $\bar{M}$ =12

5.3.1. Effect of Bearing Number on Stability

To study the effect of bearing number on the stability of GFBs with different foil models, a stability map has been plotted as shown in Fig. (5.13). The figure presents the effect of bearing number (Λ) on the stability of GFBs for all foil models vis-à-vis simple model, 1D model, 2D CPT model and 2D SDT model for a bearing configuration of L/D=1, ε =0.3, S=1.

It has been noticed from the figure that as the bearing number (Λ) increases the critical mass parameter ($\bar{M}$) increases for GFBs for all the foil models. At lower bearing number, GFBs with simple foil model predicts higher values of critical mass parameter ($\bar{M}$) as compared to other models of foil structure. However, for $\Lambda \geq 3.28$, GFBs with 2D SDT foil model predicts higher critical mass parameter than all the other foil models. This indicates that at lower speed and at lightly

loaded conditions GFBs with simple model as foil structure exhibits better rotor stability, however, at higher bearing number GFBs with 2D SDT foil model predicts better stability. The reason of such behavior may be attributed to the shearing and bending effects incorporated in the foil formulation of 2D SDT model. However, it has been observed that GFBs with 1D foil structure model predicts more conservative results with an increase in bearing number as compared to other numerical models of the GFBs. Therefore, it may be recommended that 1D model is sufficient without going for models like 2D CPT or 2D SDT model for the purpose of bearing design for stability as it would provide better factor of safety.

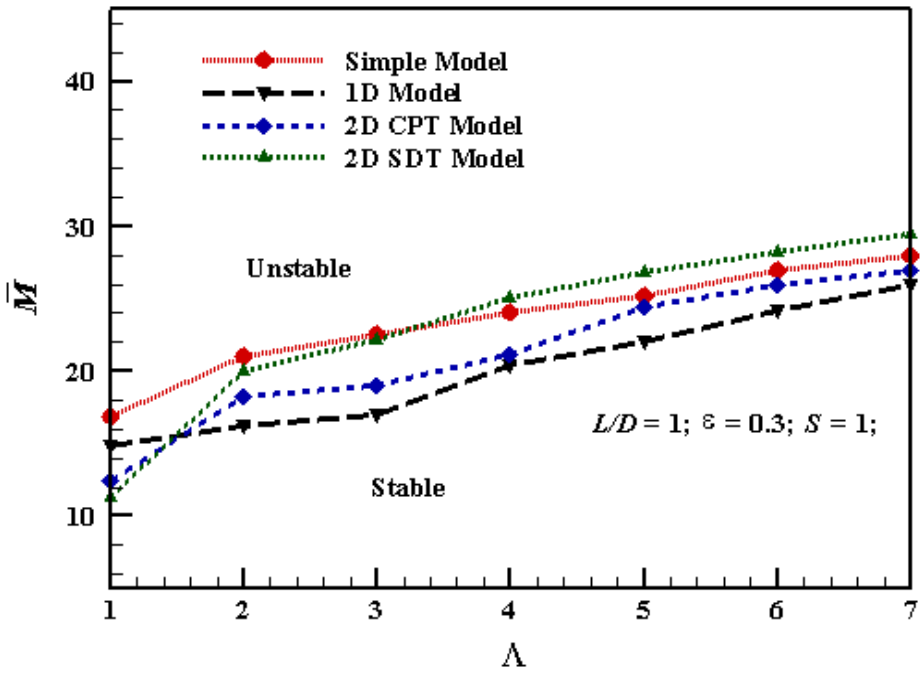

Fig. 5.13: Effect of bearing number (Λ) on the critical mass parameter ($\bar{M}$) of GFBs with different foil models for *L/D*=1, ε =0.3, *S*=1

5.3.2. Effect of Eccentricity Ratio on Stability

A stability map in the form of critical mass parameter ($\bar{M}$) versus eccentricity ratio (ε) has been presented in Fig. (5.14) for L/D=1, Λ =1, S=1 for all foil models of the GFBs (simple model, 1D model, 2D CPT model and 2D SDT model).

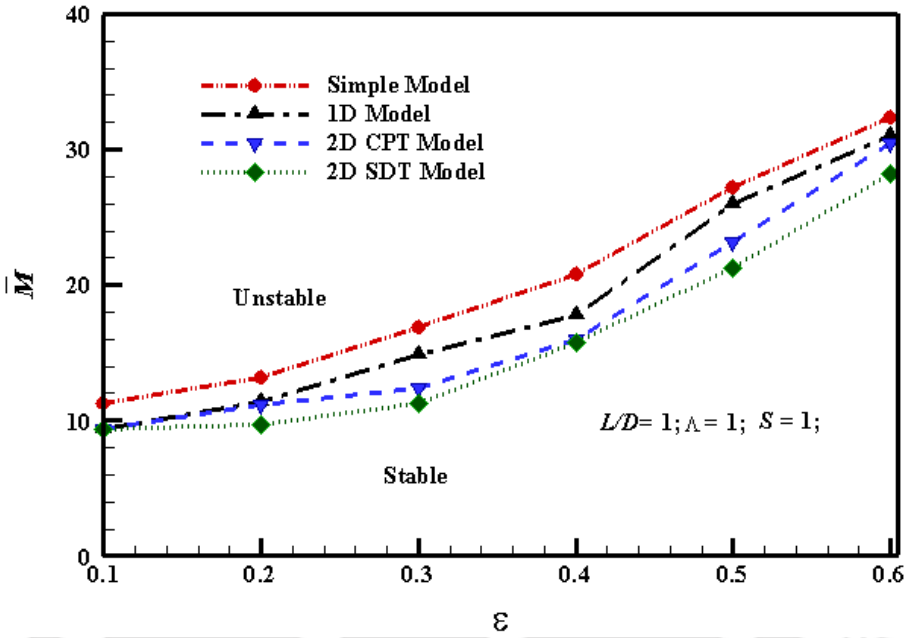

Fig. 5.14: Effect of eccentricity ratio (ε) on critical mass parameter ($\bar{M}$) of GFBs with different foil models (L/D=1, Λ =1, S=1)

Eccentricity ratio increases with the increase in load on the bearing. Stability is a concern particularly for lightly loaded bearings. It has been observed that for values of $\varepsilon \leq 0.2$ the 2D SDT model predicts more or less constant stability as compared to other foil models. Further the stability improves with eccentricity ratio for all foil models for $\varepsilon \geq 0.2$. It has also been noticed that GFBs with simple foil model depicts higher better stability as compared to other foil models and 2D

SDT foil model predicts the least for all values of eccentricity ratio. Since 2D SDT model predicts conservative stability parameter, therefore, this model suits the designers.

5.3.3. Effect of compliance coefficient on Stability

The influence of compliance coefficient (S) on stability at different bearing number (Λ) has been presented in Fig. (5.15). GFBs with simple foil model having a bump compliance coefficient of S=0, S=1 and S=2 has been considered in the present analysis. It is however significant to note that when S=0, the effect of compliance is nil, therefore GFBs are equivalent to a normal gas bearings (GBs).

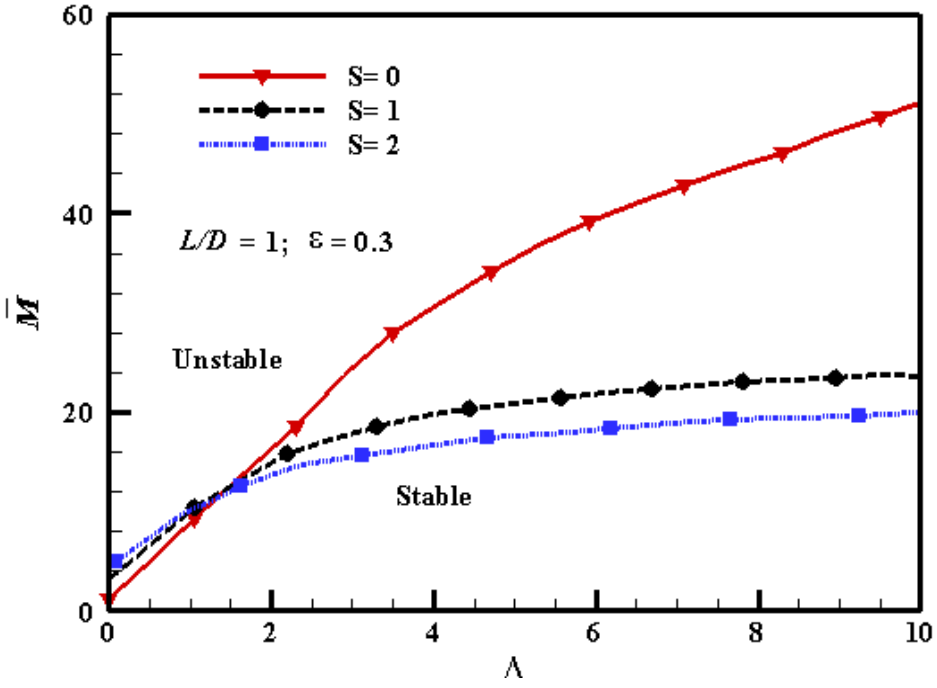

Fig. 5.15: Effect of bearing number (Λ) and compliance coefficient (S) on critical mass parameter ($\bar{M}$) for L/D=1, ε =0.3

It has been observed from Fig. (5.15) that GFBs with higher compliance coefficient

(S=2) exhibits higher critical mass parameter ($\bar{M}$) predicting better stability up to $\Lambda \leq 1.15$. However, for $\Lambda \geq 1.15$, less compliant foil structure (S=1 and S=0) predicts better stability. It has also been noticed that GFBs with compliance coefficient, S=1 and S=2 as compared to GFBs with compliance coefficient, S= 0 exhibits better stability up to bearing number $\Lambda \leq 1.34$ and $\Lambda \leq 1.28$ respectively. Nevertheless, as the bearing number increases GFBs with less compliance coefficient, S=0, predicts significantly better stability than GFBs with higher compliance coefficient (S=1 and S=2). From a conservative point of view, however, the results predicted by GFBs with higher compliance foil structure (S=2) seems more compelling as compared to bearings with less compliant foil structure.

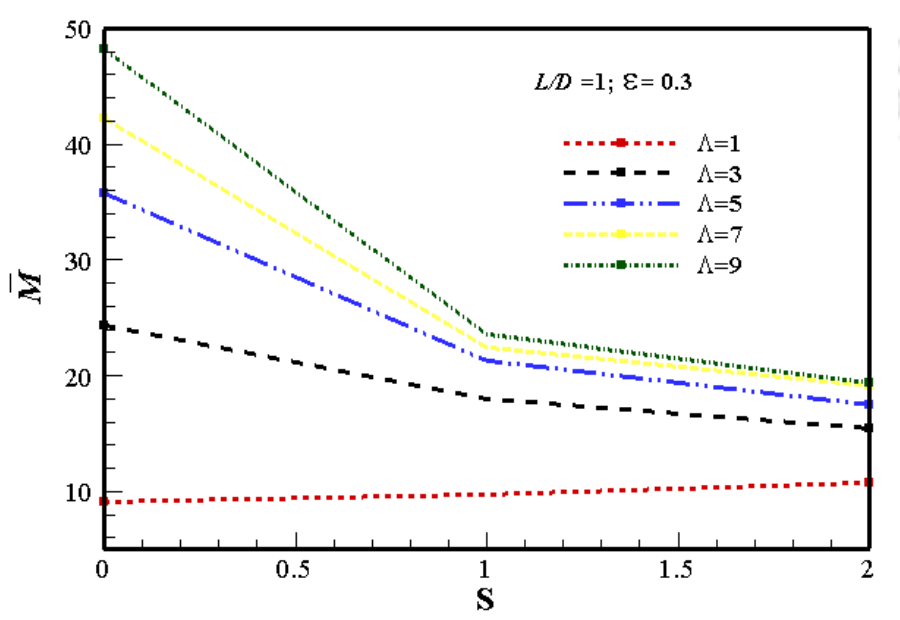

Fig. 5.16: Plot showing critical mass parameter ($\bar{M}$) versus compliance coefficient (S), for different bearing numbers (Λ) for a simple foil model of the GFBs

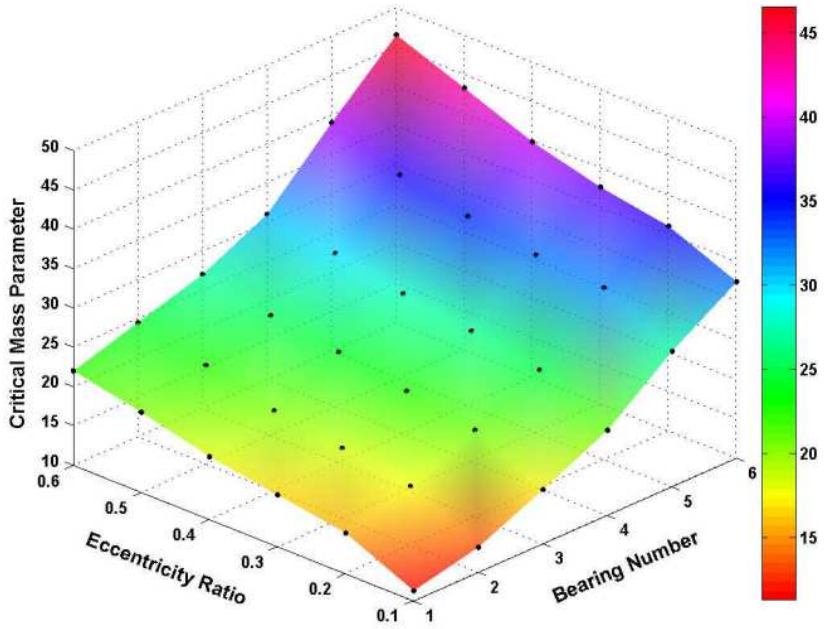

Fig. 5.17. Plot showing the variation of critical mass parameter ($\bar{M}$) for different bearing numbers (Λ) and eccentricity ratio (ε) for a simple foil model of the GFBs

The variation of the critical mass parameter ($\bar{M}$) versus compliance coefficient (S) for different bearing numbers (Λ) has been presented in Fig. (5.16), and Fig. (3.17) shows the variation of critical mass parameter ($\bar{M}$) for different bearing numbers (Λ) and eccentricity ratio (ε) for a simple foil model of the GFBs.

5.4. Computational Time

All the analyses in the present study were conducted in a computational laboratory computer with the configuration of Intel core i3 (2.88 GHz CPU). The GFBs with simple elastic foil model analysis requires much less computational time than the 1D, 2D CPT and 2D SDT foil structural models respectively as

simple model estimates the foil deflection based on the average pressure only. Therefore, in a particular case, if the time to complete the 2D model analysis requires ~10 hours, the 1D structural model analysis will take ~4 hours whereas the simple elastic model will take less than ~0.75 hours. Hence it has been observed that the iteration analysis for calculation of force coefficients and implementing the FE (finite element) matrices increases the computational time. Therefore, the introduction of the 1D, 2D CPT and 2D SDT top foil structural models into the GFBs predictive computational code increases the computational cost significantly. It is worth mentioning that the increase in computational time depends mainly on the number of degrees of freedom in the FE structural models.

5.5. Tables Showing the Summary of Important Results

Tables (5.1 to 5.5) shows the summary of some of the important results.

Table: 5.1: GFBs with simple foil structure model for *L/D*=1, *S*=1

Eccentricity Ratio (ε) ⟹			0.1	0.2	0.3	0.4	0.5	0.6
			Critical Mass Parameter Values ($\overline{M}$)					
Bearing Number (Λ) ⇓	1		11.31	13.2	16.9	20.8	27.2	32.4
	2		15.2	17.5	21	25	31.8	36
	3		16.6	18.9	22.5	26.5	32.5	37.5
	4		18	20.2	24	27.8	34	39.8
	5		20.2	22.5	25.2	29.5	35.8	43.2
	6		22	24.5	27	31	39	46.5

Table: 5.2: GFBs with 1D foil structure model for L/D=1, S=1

Eccentricity Ratio (ε) ⟹		0.1	0.2	0.3	0.4	0.5	0.6
		Critical Mass Parameter Values ($\bar{M}$)					
Bearing Number (Λ) ⇓	1	9.4	11.4	14.8	17.8	26	31
	2	12.5	14	16.2	19.5	27.2	32.8
	3	14.2	15.9	17	21	28.5	34.2
	4	16.5	18	20.4	24.2	30	36.5
	5	18.4	20.5	22	26.6	33.2	39
	6	20	22.3	24.2	28	36.6	42

Table: 5.3: GFBs with 2D CPT foil structure model for L/D=1, S=1

Eccentricity Ratio (ε) ⟹		0.1	0.2	0.3	0.4	0.5	0.6
		Critical Mass Parameter Values ($\bar{M}$)					
Bearing Number (Λ) ⇓	1	9.4	11.2	12.4	16	23.2	30.5
	2	13.2	14.8	18.2	21.2	29	34.8
	3	14.8	17.2	19	23.4	30.1	36
	4	17	18.8	21.2	25.2	31.5	38.5
	5	19.7	21.4	24.4	27.6	34.5	40.8
	6	21.5	23.5	26	29.2	38	45.2

Table: 5.4: GFBs with 2D SDT foil structure model for L/D=1, S=1

Eccentricity Ratio (ε) ⟹		0.1	0.2	0.3	0.4	0.5	0.6
		Critical Mass Parameter Values ($\bar{M}$)					
Bearing Number (Λ) ⇓	1	9.4	9.7	11.3	15.8	21.2	28.2
	2	14.5	17.8	20	24	30.5	36.4
	3	16	20.3	22.2	27.2	34	39.5
	4	18.8	22.5	25	30.2	37.5	43.2
	5	22.4	24.8	26.8	32.6	42.4	46
	6	24	26.4	28.2	34	44	50.4

5.6. Summary

Stability of a rigid rotor supported on two identical hydrodynamic gas foil journal bearings has been studied in this chapter. Non-linear time transient analysis is adopted results in plotting of journal centre trajectory for different operating conditions of the rotor. The investigation is noteworthy in the sense that critical mass parameter, which is a function of speed of rotor, can be estimated for different non-dimensional parameters such as the length to diameter ratio, bearing number, eccentricity ratio, and bump compliance coefficient. The stability maps are presented to predict the effect of these non-dimensional parameters on the stability of rotor-bearing system. The methodology and the results presented here would be useful for rotor-bearing analysis. An attempt has been made to find out alternative foil material other than structural steel in the next chapter.

Chapter 6

EFFECT OF BUMP FOIL MATERIALS ON GAS FOIL BEARINGS LOAD PERFORMANCE

6.1. Introduction

In the previous chapters, the studies on gas foil bearings (GFBs) performance characteristics and the predictions has been confined only with structural steel as the foil materials. Therefore, this chapter explores the possibilities of using different foil materials for GFBs. An initial study on the load carrying capacity of the GFBs have been made by exploring different materials keeping in perspective the steady state characteristics performance of the bearing. The geometry and the bump foil structure adopted for the preliminary study has been adhered to the simple elastic foil model [9] which many researches have worked with.

6.2. GFBs Geometry and Compliance Coefficient

A review of various geometries of GFBs adopted by different researchers has been presented in Table (6.1). The variation of bump compliance coefficient (S) for different GFB geometries as well as the material properties has also been represented.

Table 6.1: Variation of compliance coefficient (*S*) and material properties for different GFB geometries

**	s [mm]	l_o [mm]	C [µm]	t_b [µm]	υ	E_b [Gpa]	S
[24]	4.572	1.778	31.8	101.6	0.29	214	0.663
[26]	4.064	1.778	20	127	0.31	200	0.514
[31]	4.572	1.778	31.8	102	0.29	214	0.656
[34]	4.572	1.778	31.8	102	0.29	214	0.738
[46]	4.572	2.032	35.5	102	0.29	213.7	0.878
[48]	4.572	2.032	15	101.6	0.29	213.7	2.104
[59]	4.572	2.032	35.5	102	0.29	213	0.881
[74]	4.064	1.778	20	127	0.31	200	0.514
[91]	4.572	1.778	31.8	101.6	0.29	214	0.663
[92]	4.572	1.778	20	101.6	0.29	214	1.058

** References

In course of the investigation carried out for the comparison of bearing geometries, vis-a-vis, compliance coefficient as shown in Table (6.1). It is noteworthy to observe from the available literatures over the years that the foils used in GFBs are mostly structural steel, which is mainly because of its favorable characteristics. It has been, therefore, proposed to investigate the suitability of other materials for bump foil of GFBs. In view of the availability of materials used for GFBs apart from the structural steel, two materials have been considered. Firstly, copper [87] which has a Young's modulus of 117 GPa with the properties of being a good conductor, malleable and ductile making it good for bending into foils and secondly, fiber reinforced polymer (FRP) [95, 96] a composite material which have the advantage over structural steel being light weight, directional strength and stiffness, durability under harsh service environments, corrosion

resistance, design flexibility and low thermal conductivity. The FRP composites which have been considered for the analysis is a carbon fiber reinforce polymer which has a tensile modulus of 440 GPa. The steady state load capacity of the GFBs with structural steel, copper and FRP composite as the bump foil material have been predicted and compared. However, it is sensible to note that further theoretical and experimental investigations are required to validate the feasibility of copper and FRP composite properties as bump foils, which is beyond the scope of the present work. Further, though FRP composite is not isotropic, as an initial study it has been assumed to be isotropic ignoring its directional properties.

6.3. Load Capacity of GFBs with Different Foil Materials

As discussed in chapter 2 (Sections 2.4, 2.5, and 2.6) the procedures has been employed for predicting the steady state load carrying capacity of the bump type GFBs with different foil materials. It is noteworthy, however, that the load carrying capacity of the GFBs are significantly lower than plain gas bearings (GBs). A comparison of the load carrying capacity of GFBs with structural steel as bump foil materials and plain gas bearing (GB) has been presented in Fig. (6.1) for similar bearing configuration. It has been observed that the plain GB has much higher load carrying capacity than the GFB for similar bearing configuration. It has been noticed that at higher eccentricity ratio ($\varepsilon = 0.8$) the plain GB predicts 66.49% higher load carrying capacity than GFBs. This indicates that the foil structure of the GFBs plays a vital role in the load performance of GFBs. As

discuss in chapter 4 (Section 4.5.4), it has also been observed that the load performance greatly varies with bump compliance coefficient (S) of the foil, it is certain that the compliance coefficient (S) should be as low as possible to achieve a higher load carrying capacity but limiting to S=0 which is the value for a plain gas bearing (GBs). Therefore, it is perhaps essential to investigate how to achieve a higher load capacity of the GFBs and at the same time uphold the advantages of foil structure of the GFBs.

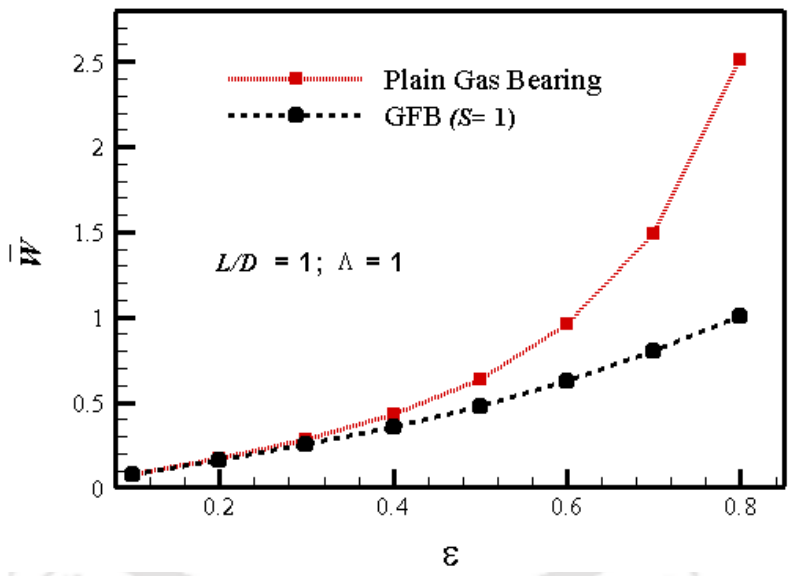

Fig. 6.1: Comparison of load carrying capacity ($\bar{W}$) of GFBs and plain gas bearings (GBs)

It has been observed that the load carrying capacity of the GFBs is mainly influenced by two factors, firstly its geometry and the operating conditions and secondly, the foil materials used. And as evident from the Table (6.1), it has been observed that different authors have adopted a similar bearing geometry.

Therefore, predictions of the GFBs steady state load capacity have been made by using different foil materials keeping similar bearing geometry and working conditions.

The non-dimensional load carrying capacity ($\bar{W}$) as well as the attitude angle **(ϕ)** of the GFBs have been predicted and presented in Fig. (6.2) and Fig. (6.3) with different foil materials namely structural steel, copper and carbon fiber reinforced polymer at different eccentricity ratio (ε).

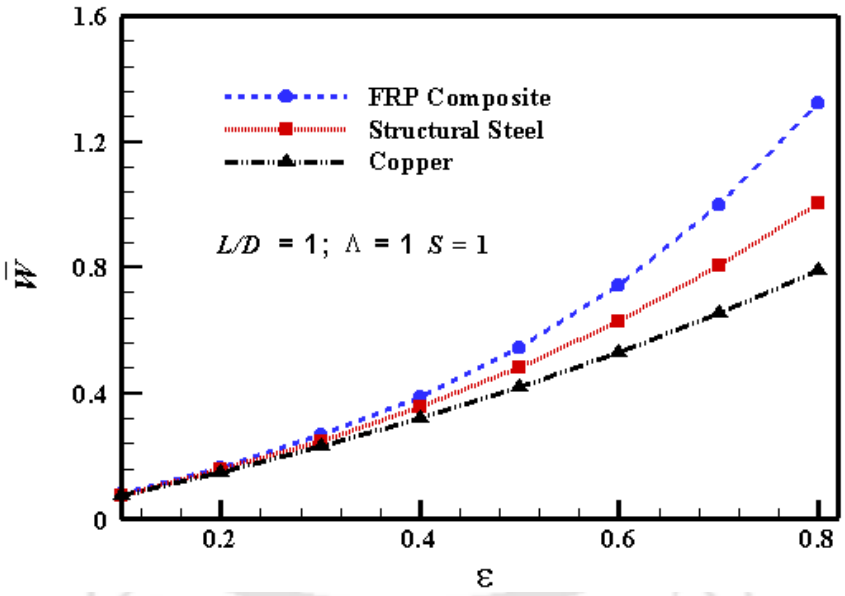

Fig. 6.2: Load carrying capacity ($\bar{W}$) with respect to eccentricity ratio (ε) of GFBs with different foil materials

It has been observe from the Fig. (6.2) that there is a significant increase in the load carrying capacity of the GFBs with FRP composite as bump foil material as compared to structural steel and copper. The higher load capacity of GFBs

predicted by using FRP composite as foil material (at higher eccentricity ratio, ε=0.8) amounts to about 31.33% and 67.66% as compared to structural steel and copper respectively. This may be attributed to the reason that FRP composite as foil material have lower compliance coefficient as compared to both structural steel and copper as foil material with similar bearing configuration. Therefore, from the load capacity performance analysis, carbon FRP composite as foil material as compared to structural steel and copper can be recommended, subject to further investigation taking into account the anistropic characteristics, particularly for bump type GFBs as the foil material.

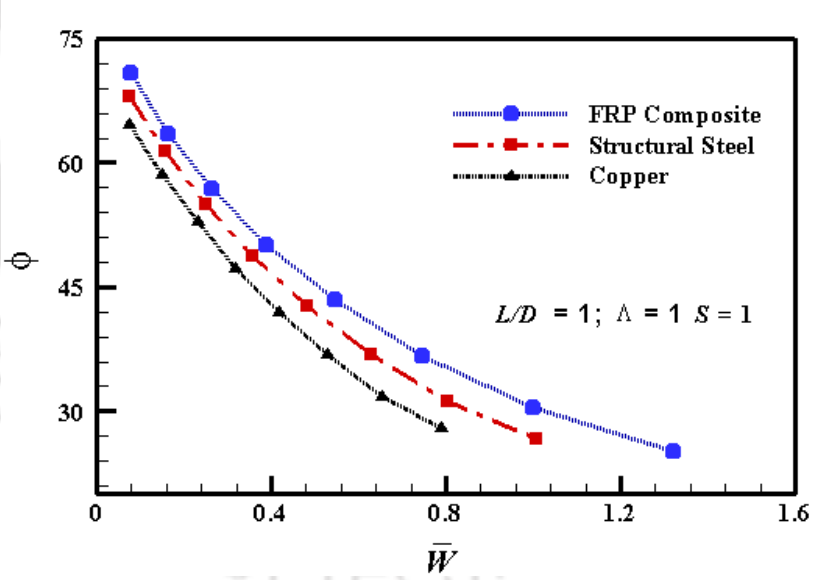

Fig. 6.3: Journal attitude angle (ϕ) versus load carrying capacity ($\bar{W}$) for GFB with different foil materials

The attitude angle (ϕ) with respect to load carrying capacity **($\bar{W}$)** of the GFBs for all three types of bump foil materials i.e., structural steel, copper and FRP

composite is presented in Fig. (6.3). It has been observed that the attitude angle decreases as the load capacity increases for GFBs with all three foil materials.

6.4. Summary

This chapter presents a preliminary study of a simple elastic foil model of a bump-type GFB, wherein the steady state load carrying capacity of the GFBs has been analyzed by considering different bump foil material namely structural steel, copper and FRP composite respectively. The results were encouraging and from the load capacity performance analysis, carbon FRP composite material as compared to structural steel and copper has been found to be a better choice particularly for bump type GFBs as the foil material. Experimentalists may consider varifying the model by experimental evidences, which is beyond the scope of the present work. Also thermohydrodynamic study of GFBs with FRP composites as the foil material, the bonding of the FRP composite with steel and the anisotropic behavior of the composite materials which have not been taken into account needs attention.

Chapter 7

CONCLUSIONS AND FUTURE SCOPE

7.1. Conclusions

In this chapter, some of the important conclusions made have been summarized based on the numerical results and discussions of problems addressed in the present thesis.

- For all foil models of the GFBs it has been observed that, load capacity **($\bar{W}$)** increases as the eccentricity ratio increases. At higher eccentricity ratio GFBs with 2D SDT foil model predicts higher load carrying capacity as compared to all other foil models. This may be attributed to the reason that 2D SDT foil model formulation incorporates both shearing and bending effects, whereas other models do not include shearing effect in particular.

- As the bearing number increases **(Λ),** an increase of approximately 28% (at bearing number, Λ=10) in the load carrying capacity has been observed for 2D SDT foil model as compared to other foil models of GFBs with similar bearing configuration. Therefore it has been inferred that 2D SDT model is the best model for prediction of steady state characteristics as it incorporates both shearing and bending effects.

- As small attitude angles are a desirable features in GFBs since they denote a journal displacement parallel to the load direction, it has been observed that with an increase in eccentricity ratio, the attitude angle decreases for all the foil models of GFBs, with 2D SDT foil model predicting a slightly larger attitude angle as compared to other foil models of GFBs.

- With an increase in the values of compliance coefficient (S), the load carrying capacity **(**$\bar{W}$**)** decreases for all the foil models of GFBs considered here**.** GFBs with 2D SDT foil model predicts higher load carrying capacity as compared to other foil models with similar bearing configuration, and simple foil model predicts the least. The lower load capacity of GFBs with simple foil model with respect to compliance coefficient can be attributed to the simplicity in its foil design which does not incorporate any effect of bending and shear.

- It has been noticed that for all the foil models of GFBs the compliance coefficient (S) of the foils should be as low as possible to achieve a higher load carrying capacity but limiting to the value for a plain gas bearing (GBs), i.e. S=0. It is worth mentioning that a plain gas bearings (GBs) has much higher load carrying capacity than the GFBs with similar bearing configuration.

- As the bearing number (Λ) increases, the critical mass parameter ($\bar{M}$) of

the GFBs increases. It has been observed that at lower speed and at lightly loaded conditions GFBs with simple model as foil structure exhibits better rotor stability, however, at higher bearing number GFBs with 2D SDT foil model predicts better stability. GFBs with 1D foil structure model predicts a more conservative results as bearing number increases compared to other foil models of the GFBs. Therefore, it may be recommended that 1D foil model of the GFBs is sufficient without going into 2D CPT or 2D SDT models for the purpose of bearing design for stability as it would provide better factor of safety.

- Eccentricity ratio increases with the increase in load on the bearing. At higher eccentricity ratio, it has been noticed that, GFBs with simple foil model predicts better stability as compared to other foil models. At lower eccentricity ratio 2D SDT model predicts more or less constant stability and implies more conservative results, therefore, this model suits the designers.
- GFBs with less compliance coefficient predicts significantly better stability than GFBs with higher compliance coefficient as the bearing number increases. From a conservative point of view, however, the results predicted by GFBs with higher compliance foil structure seems more compelling as compared to bearings with less compliant foil structure.

- It has been noticed that the computational time increases significantly with the introduction of the 1D, 2D CPT and 2D SDT top foil structural models respectively into the GFBs predictive computational code. It is worth mentioning that the increase in computational time by incorporating finite element (FE) structural models directly increases the computational costs.

- It has been noticed that the GFBs have considerably low load capacity as compared to plain GBs. An approximately 66.49% higher load carrying capacity is predicted by the plain GBs particularly at higher eccentricity ratio ($\varepsilon = 0.8$) as compared to GFBs with similar bearing material and configuration. This indicates that the foil structure plays a vital role in the load performance of the GFBs. Hence, by exploring the use of suitable foil materials for the GFBs, it has been observe that, a significant increase in the load carrying capacity can be attained. GFBs with FRP carbon composite as bump foil material has predicted an increase of about 31.33% and 67.66% higher load capacity as compared to structural steel and copper respectively. This may be attributed to the reason that FRP carbon composite as foil material have lower compliance coefficient as compared to both structural steel and copper as foil material with similar bearing configuration. Therefore, from the load capacity performance analysis,

FRP carbon composite as bump foil material as compared to structural steel and copper can be recommended, subject to further investigation taking into account the anistropic characteristics.

7.2. Scope for Future Work

Although the objectives of this thesis have been fulfilled by the contributions presented in the preceding chapters of this dissertation, further research may still be pursued for the purpose of enhancing performance of the gas foil bearings. Some of the future works which may be keenly undertaken in line with the present work are as follows,

- Incorporating friction between the bearing housing and bump foil, between the bump foil and top foil and the deflection dependency of bump foil stiffness.
- The stability analysis of the rotor-bearing configuration can be extended by considering a flexible rotor.
- Thermohydrodynamic study of GFBs with FRP carbon composites as the foil material, the bonding of the FRP composite with steel and the anisotropic behavior of the composite materials can further be addressed.
- The foil structure can be modeled by encompassing peizo electric materials in the bumps which will have the advantages of

- Controllable stiffness and damping
- Higher load carrying capacity
- Provide additional compliance to the rotor deflection
- Startup and run down efficacy

REFERENCES

[1] DellaCorte, C., Radil, K., Howard, S., and Bruckner, J., 2006. "A Preliminary Foil Gas Bearing Performance Map". NASA/TM-214343.

[2] Carpino, M., 1994. "Foil Bearing Research at Penn State" NASA Technical Report, 2, pp. 148-151.

[3] Kim, T., H., 2007. "Analysis of Side End Pressurized Bump Type Gas Foil Bearings: A Model Anchored to Test Data" Ph.D. Dissertation, Texas A&M University.

[4] DellaCorte, C., Valco, M., J., 2000. "Load Capacity Estimation of Foiled Air Journal Bearings for Oil-Free Turbomachinary Applications" NASA/TM-209782.

[5] Peng, Z., 2003. "Thermodynamic analysis of compressible Gas Flow in Compliant Foil Bearings" Thesis: Master of Science (MS), Louisiana State University and Agricultural and Mechanical College.

[6] Koepsel, F., 1976. "Gas Lubricated Foil Bearing Development for Advanced Turbomachines" AFAPL-TR. 01, pp. 76-114.

[7] Agrawal, G., L., 1997, "Foil Air/Gas Bearing Technology – an Overview," ASME Paper No. 97-GT-347.

[8] Nalepa, K., Pietkiewicz, P., and Żywica, G., 2009. "Development of the Foil Bearing Technology" Techn. Sc., No 12. DOI 10.2478/v10022-009-0019-2

[9] Heshmat, H., Walomit, J., and Pinkus, O., 1983. "Analysis of Gas-Lubricated Compliant Journal Bearings" ASME J. ASME J. Lubr. Technol., 105, pp. 647–655

[10] Heshmat, H., 1994, "Advancements in the Performance of Aerodynamic Foil Journal Bearings: High Speed and Load Capability" ASME J. Tribol., 116, pp. 287–295.

[11] Heshmat, H., 2000, "Operation of Foil Bearings Beyond the Bending Critical Mode," ASME J. Tribol., 122, pp. 192–198.

[12] Lee, Y., B., Kim, T., H., Kim, C., H., Lee, N., S., and Choi, D. H., 2004, "Dynamic Characteristics of a Flexible Rotor System Supported by a Viscoelastic Foil Bearing," Tribol. Int., 37, pp. 679–687

[13] Ku, C., P., and Heshmat, H., 1992. "Complaint Foil Bearing Structural Stiffness Analysis Part I: Theoretical Model—Including Strip and Variable Bump Foil Geometry" ASME J. Tribol. 114, pp. 394–400.

[14] Ku, C., P., and Heshmat, H., 1993. "Complaint Foil Bearing Structural Stiffness Analysis Part II: Experimental Investigation" ASME J. Tribol. 113, pp. 364–369

[15] Heshmat, H., Shapiro, W., and Gray, S., 1982, "Development of Foil Journal Bearings for High Load Capacity and High Speed Whirl Stability," ASME J. Lubr. Technol., 104, pp. 149–156.

[16] Peng, J., P., and Carpino, M., 1993 "Calculation of Stiffness and Damping Coefficient for Elastically Supported Gas Foil Bearings" ASME J. Tribol. 115, pp. 20–27

[17] Ku, C., P., and Heshmat, H., 1994. "Structural Stiffness and Coulomb Damping in Compliant Foil Journal Bearing: Theoretical Considerations" STLE, Tribology Transactions. 37, pp. 525–533.

[18] Juan, C., H., and Connolly, D., 1992. "Three-dimensional finite element analyses of self-acting foil bearings" Computer Methods in Applied Mechanics and Engineering. 100, pp. 31-43

[19] Tadjbaksh, I., G., and Ahmadi, G., 1993. "Numerical Technique in the Hydrodynamic Theory of Foil Bearings" Int. J. of Engng. Sci. 21(7), pp. 781-789

[20] Braun, M., J., Choy, F. K., Dzodzo, M. and Hsu, J., 1996. "Two-dimensional dynamic simulations of a continuous foil bearing" Tribol. Int., 29 (1), pp. 61-68.

[21] Peng, Z., 2003. "Thermodynamic analysis of compressible Gas Flow in Compliant Foil Bearings" Thesis: Master of Science (MS), Louisiana State University and Agricultural and Mechanical College.

[22] Peng, Z., C., and Khonsari, M., M., 2006. "A Thermo hydrodynamic Analysis of Foil Journal Bearings" ASME J. Tribol., 128, pp. 534-541.

[23] Kim, T., H., and San Andre´s, L., 2007. "Analysis of advanced gas foil bearings with piecewise linear elastic supports" Tribol. Int., 40, pp. 1239-1245

[24] Kim, T., H., and San Andre´s, L., 2008. "Heavily Loaded Gas Foil Bearings - A Model Anchored to Test Data" ASME J. Eng. Gas Turb. Power. 130, pp. 012504.

[25] San Andre´s, L., and Kim, T., H., 2009. "Analysis of gas foil bearings integrating FE top foil models" Tribol. Int., 42, pp.111-120.

[26] San Andre´s, L., and Kim, T., H., 2010. "Thermohydrodynamic Analysis of Bump Type Gas Foil Bearings - A Model Anchored to Test Data" ASME J. Eng. Gas Turb. Power. 132, pp. 042504

[27] Iordanoff, I., Bou Said, B., Mezianne, A., and Berthier, Y., 2007. "Effect of internal friction in the dynamic behavior of aerodynamic foil bearings" Tribol. Int., 41, pp. 387-395

[28] Park, D. J., Kim, C. H., Jang, G. H., and Lee, Y. B., 2007. "Theoretical considerations of static and dynamic characteristics of air foil thrust bearing with tilt and slip flow" Tribol. Int., 41, pp. 282-295.

[29] Knowels, S. W., 2009. "An Investigation of foil thickness on Performance for Oil Free Bearings" Thesis - Master of Science (MS), Case Western Reserve University.

[30] Feng, K., and Kaneko, S., 2009. "Calculation of Dynamic Coefficient for Multi-wound Foiled Bearings" Journal of System Design and Dynamics. 3 (5), pp. 841-852

[31] Lee, D. H., Kim, Y. C., and Kim, K. W., 2009. "The effect of Coulomb friction on the static performance of foil journal bearings" Tribol. Int., 43, pp. 1065-1072.

[32] Yu, H., Shuangtao, C., Rugang, C., and Qiaoyu, Z., 2011. "Numerical study on foil journal bearings with protuberant foil structure" Tribol. Int., 44 (9), pp. 1061-1070.

[33] Yang, L., Qi, S., Geng, H., and Yu, L., 2011. "Stability Analysis on Rotor Systems Supported by Self-acting Tilting pad Gas Bearings with Frequency Effects" Chinese Journal of Mechanical Engineering. 24, pp. 1-6.

[34] Lez, S., L., Arghir, M., and Frene, J., 2007. "A New Bump-Type Foil Bearing Structure Analytical Model" ASME J. Eng. Gas Turb. Power. 129, pp. 1047-1057.

[35] Lez, S., L., Arghir, M., and Frene, J., 2007. "Static and Dynamic Characterization of a Bump-Type Foil Bearing Structure" ASME J. Tribol., 129, pp. 75-83.

[36] Reddy, D., S., K., Swarnamani, S., and Prabhu, B., S., 1997. "Analysis of aerodynamic multileaf foil journal bearings" Wear. 209, pp. 115-122.

[37] Lee, D., and Kim, D., 2011. "Design and Performance Prediction of Hybrid Air Foil Thrust Bearings [HAFB]" ASME J. Eng. Gas Turb. Power. 133, pp. 042501

[38] DellaCorte, C., and Valco, M., J., 2000. "Load Capacity Estimation of Foiled Air Journal Bearings for Oil-Free Turbomachinary Applications" ARL-TR-2334.

[39] Howard, S., A., and DellaCorte, C., 2006. "Gas Foil Bearings for Space Propulsion Nuclear Electric Power Generation". NASA/TM-214115.

[40] Kim, D., Creary, A., Chang, S., S., and Kim, J., H., 2009. "Mesoscale Foil Gas Bearings for Palm- Sized Turbomachinery Design, Manufacturing, and Modeling" Journal of Engineering for Gas Turbines and Power. 131, pp. 042502

[41] Radil, K., C., and DellaCorte, C., 2009. "A Three-Dimensional Foil Bearing Performance Map Applied to Oil-Free Turbomachinery". ARL-TR-4473.

[42] DellaCorte, C., and Bruckner, R., J., 2011. "Remaining Technical Challenges and Future Plans for Oil-Free Turbomachinery" Journal of Engineering for Gas Turbines and Power. 133, pp. 042502.

[43] Song, J., H., and Kim, D., 2007. "Foil Gas Bearing With Compression Springs Analyses and Experiments" ASME J. Tribol., 129, pp. 628-639.

[44] Arora, V., Van der Hoogt, P., J., M., Aarts, R., G., K., M., and de Boer, A., 2010. "Identification of dynamic properties of radial air-foil bearings" Int. J. Mech. Mater Des. 6, pp. 305–318.

[45] San Andrés, L., Ryu, K., and Kim, T., H., 2011. "Identification of Structural Stiffness and Energy Dissipation Parameters in a Second Generation Foil Bearing Effect of Shaft Temperature" ASME J. Eng. Gas Turb. Power. 133, pp. 032501

[46] Rubio, D., San Andrés, L., 2007. "Structural Stiffness, Dry Friction Coefficient, and Equivalent Viscous Damping in a Bump-Type Foil Gas Bearing" ASME J. Eng. Gas Turb. Power. 129, pp. 494-502.

[47] Breedlove, A., W., 2007. "Experimental identification of structural force coefficients in a Bump-Type Foil Bearing" Thesis: Master of Science (MS). Texas A&M University.

[48] Kim, T., H., Breedlove, A., W., and San Andrés, L., 2009. "Characterization of a Foil Bearing Structure at Increasing Temperatures Static Load and Dynamic Force Performance" ASME J. Tribol., 131, pp. 041703.

[49] Kumar, M., and Kim, D., 2009. "Static performances of hydrostatic air bump foil bearing" Tribol. Int., 43, pp. 752-758

[50] Yang, L., Hu, D., Liu, H., Yu, L., 2008. "Experimental Investigation on the Performance of Aerodynamic Compliant Foil Air Bearings" Proceedings of the IEEE, International Conference on Automation and Logistics Qingdao. China. pp. 1285-1289

[51] Dickman, J., R., 2010. "An Investigation of Gas Foiled Thrust Bearing Performance and Its Influencing Factors" Thesis - Master of Science (MS), Case Western Reserve University.

[52] Lee, Y., B., Park, D., J., Kim, C., H., and Kim, S., J., 2007. "Operating characteristics of the bump foil journal bearings with top foil bending phenomenon and correlation among bump foils" Tribol. Int., 41, pp. 221-233

[53] Kim, D., and Lee, D., 2010. "Design of Three-Pad Hybrid Air Foil Bearing and Experimental Investigation on Static Performance at Zero Running Speed" ASME J. Eng. Gas Turb. Power. 132, pp. 122504

[54] Radil, K., Howard, S., and Dykas, B., 2002. "The Role of Radial Clearance on the Performance of Foil Air Bearings" NASA/TM-211705

[55] Lee, Y., B., Kim, T., H., Kim, C., H., Lee, N., S., and Choi, D., H., 2003. "Dynamic characteristics of a flexible rotor system supported by a viscoelastic foil bearing (VEFB)" Tribol. Int., 37, pp. 679-687

[56] San Andre´s, L., and Kim, T., H., 2008. "Forced nonlinear response of gas foil bearing supported rotors" Tribol. Int., 41, pp. 704-715.

[57] San Andrés, L., Ryu, K., and Kim, T., H., 2011. "Thermal Management and Rotor dynamic Performance of a Hot Rotor- Gas Foil Bearings System—Part I Measurements" ASME J. Eng. Gas Turb. Power. 133, pp. 062501

[58] Kim, T., H., and San Andre´s, L., 2009. "Effect of Side Feed Pressurization on the Dynamic Performance of Gas Foil Bearings A Model Anchored to Test Data" ASME J. Eng. Gas Turb. Power. 131, pp. 012501

[59] San Andre´s, L., Rubio, D., and Kim, T., H., 2007. "Rotordynamic Performance of a Rotor Supported on Bump Type Foil Gas Bearings Experiments and Predictions" ASME J. Eng. Gas Turb. Power. 129, pp. 850-857

[60] Howard, S. A., 2009. "Misalignment in Gas Foil Journal Bearings -An Experimental Study Modeling" ASME J. Eng. Gas Turb. Power. 131, pp. 022501

[61] San Andrés, L., and Ryu, K., 2008. "Flexure Pivot Tilting Pad Hybrid Gas Bearings Operation Wit Worn Clearances and Two Load-Pad Configurations" ASME J. Eng. Gas Turb. Power. 130, pp. 042506

[62] Shetty, P., K., 2010. "Imbalance Response of a Four Degree of Freedom rigid Rotor Support by Hybrid Three Pad Air Foil Bearing" Thesis: Master of Science (MS). The University of Texas at Arlington

[63] San Andrés, L., 2006. "Hybrid Flexure Pivot-Tilting Pad Gas Bearings Analysis and Experimental Validation" ASME J. Tribol., 128, pp. 551-558.

[64] Kaneko, S., Miyano, Y., and Watanabe, T., 2005. "Static and Dynamic Characteristic of a Micro Gas Turbine Rotor Supported by Radial Foiled Bearings" PowerMEMS. The University Of Tokyo, Japan, pp. 89-92

[65] Kim, D., and Park, S., 2009. "Hydrostatic air foil bearings Analytical and experimental investigation" Tribol. Int., 42, pp. 413-425.

[66] Osborne, D., A., and San Andre´s, L., 2006. "Experimental Response of Simple Gas Hybrid Bearings for Oil-Free Turbomachinery" Journal of Engineering for Gas Turbines and Power. 128, pp. 626-633.

[67] Bou-Saïd, B., Grau, G., and Iordanoff, I., 2008. "On Nonlinear Rotor Dynamic Effects of Aerodynamic Bearings with Simple Flexible Rotors" ASME J. Eng. Gas Turb. Power. 130, pp. 012503

[68] Heshmat, H., Hryniewicz, P., Walton II, J., F., Willis, J., P., Jahanmir, S., and DellaCorte, C., 2005. "Low-friction wear-resistant coatings for high-temperature foil bearings" Tribol. Int., 38, pp. 1059-1075.

[69] Sadashiva, R., P., 2010. "Experimental Investigation of Thermal behaviors of Air Foil Bearings [AFB]" Thesis -Master of Science (MS). University of Texas at Arlington

[70] Dykas, B., D., and Tellier, D., W., 2008. "A Foil Thrust Bearing Test Rig for Evaluation of High Temperature Performance and Durability" ARL-MR-0692.

[71] Radil, K., and Zeszotek, M., 2004. "An Experimental Investigation into the Temperature Profile of a Compliant Foiled Air Bearing" Army Research Laboratory. NASA/TM-213100

[72] Feng, K., and Kaneko, S., 2009. "Thermohydrodynamic (THD) Study of Multi-wound Foil Bearing Using Lobatto Point Quadrature" ASME J. Tribol., 131, pp. 021702

[73] San Andrés, L., and Kim, T., H., 2010. "Thermohydrodynamic Model Predictions and Performance Measurements of Bump-Type Foil Bearing for Oil-Free Turboshaft Engines in Rotorcraft Propulsion Systems" ASME J. Tribol., 132, pp. 011701.

[74] Lee, D., Kim, D., and Sadashiva, R., P., 2011. "Transient Thermal Behavior of Preloaded Three-Pad Foil Bearings Modeling and Experiments" ASME J. Tribol., 133, pp. 021703.

[75] Kim, T., H., and San Andrés, L., 2006. "Limits for High-Speed Operation of Gas Foil Bearings" ASME J. Tribol., 128, pp. 670-673

[76] Bauman, S., 2005. "An Oil-Free Thrust Foil Bearing Facility Design, Calibration, and Operation" NASA/TM-213568.

[77] Salehi, M., Heshmat, H., Walton II, J., F., and Tomaszewski, M., 2007. "Operation of a Mesoscopic Gas Turbine Simulator at Speeds in Excess of 700,000 rpm on Foil Bearings" ASME J. Eng. Gas Turb. Power. 129, pp. 170-176.

[78] Hikichi, K., Togo, S., Isomura, K., Saji, N., Esashi, M., and Tanaka, S., 2009. "Ultra-High Speed Tape-Type Radial Foil Bearing for Micro Turbo Machinery" Power MEMS. Washington DC. Dec. 1-4, pp. 79-82.

[79] Zhou, Q., Hou, Y., and Chen, C., 2008. "Dynamic stability experiments of compliant foil thrust bearing with viscoelastic support" Tribol. Int., 42, pp. 662-665.

[80] Vleugels, P., Waumans, T., Peirs, J., Al Bender, F., and Reynaerts, D., 2006. "High-speed foil bearings for micro gas turbines test set-up". The Sixth International Workshop on Micro and Nanotechnology for Power Generation and Energy Conversion Applications. Berkeley, Nov. 29-Dec. 01, pp. 57-60.

[81] Xiong, L., Y., Wu, G., Hou, Y., Liu, L., Q., Ling M., F., and Chen, C., Z., 1997. "Development of aerodynamic Foil Journal Bearings for a high speed cryogenic turboexpander" Cryogenics. 37, pp. 221-230.

[82] Creary, A., J., 2009. "Manufacturing of a Gas Foil Bearing for Palm-Sized Turbomachinery" Thesis -Master of Science (MS). Texas A&M University.

[83] Dykas, B., Bruckner, R., J., DellaCorte, C., Edmonds, B., and Prahl, J., 2009. "Design, Fabrication, and Performance of Foil Gas Thrust Bearings for Microturbomachinery Applications" ASME J. Eng. Gas Turb. Power. 131, pp. 012301.

[84] Radil, K., C., and DellaCorte, C., 2009. "Foil Bearing Starting Considerations and Requirements for Rotorcraft Engine Applications" ARL-TR-4873.

[85] Howard, S., A., Bruckner, R., J., and DellaCorte, C., 2007. "Gas Foil Bearing Technology Advancements for Closed Brayton Cycle (CBC) Turbines" NASA/TM-214470.

[86] Dykas, B., D., 2006. "Factors Influencing the Performance of Foil Gas Thrust Bearings for Oil-Free Turbomachinery Applications" Thesis: Doctor of Philosophy, Case Western University.

[87] Hou, Y., Zhu, Z., H., and Chen, C., Z., 2003. "Comparative test on two kinds of new compliant foil bearing for small cryogenic turbo-expander" Cryogenics. 44, pp. 69-72

[88] Koepsel, W., F., 1976. "Gas Lubricated Foil Bearing Development for Advanced Turbomachines" AFAPL-TR-114(1)

[89] Bruckner, R., J., 2009. "Windage Power Loss in Gas Foil Bearings and the Rotor-Stator Clearance of High Speed Generators Operating in High Pressure Environments" NASA/TM-215826.

[90] Hashimoto, H., 2000. "Experimental studies of porous foil bearings for web-handling" Tribol. Int., 33, pp. 191-196.

[91] Feng, K., and Kaneko, S., 2010 "Analytical Model of Bump-Type Foil Bearings Using a Link-Spring Structure and a Finite-Element Shell Model" ASME J. Tribol. 132, pp. 021706.

[92] Ruscitto D, Mc Cormick J, and Gray S. 1978. "Hydrodynamic Air Lubricated Compliant Surface Bearing for an Automotive Gas Turbine Engine" I-Journal Bearing Performance. NASA CR-135368

[93] Yang, P., Zhu, K., Q., Wang, X., L., 2009. "On the non-linear stability of self-acting gas journal bearings" Tribol. Int., 42, pp. 71– 76.

[94] Reddy, J., N., 1993, "An Introduction to the Finite Element Method" McGraw Hill, Inc, Second Edition.

[95] Tuakta C. 2005. "Use of Fiber Reinforced Polymer Composite in Bridge Structures" Thesis, Master, Massachusetts Institute of Technology.

[96] Chaban, V., V., and Nazarenko, J., S., 2011. "Simulated strength and structure of carbon–carbon reinforced composite" Mater. Chem. Phys. 129 (3), pp. 1240-1246

[97] Ruscitto, D., Mc Cormick, J., and Gray, S., 1978, "Hydrodynamic Air Lubricated Compliant Surface Bearing for an Automotive Gas Turbine Engine" I-Journal Bearing Performance, NASA CR-135368.

LIST OF PUBLICATIONS

The present thesis work has led to the following publications:

1. Jamir, T., M., and Kakoty, S., K., 2013 "Load Capacity Analysis of Gas Foil Bearing (GFB) for Different Foil Materials" Springer, Proceedings of International Conference on Advances in Tribology and Engineering Systems, Ahmedabad, India, pp. 331-343
2. Jamir, T., M., Kakoty, S., K., and Kalita, K., 2014, "Gas Foil Bearing Analysis and the Effect of Bump Foil Thickness on Its Performance Characteristics Using A Non-Linear Matrix Equation Solver" International Journal of Recent advances in Mechanical Engineering. 3 (3), pp. 15-30
3. Jamir, T., M., Kakoty, S., K., and Kalita, K., 2014. "Gas Foil Bearings (GFBs) With Different Bump Foil Materials" Trends in Machine Design, STM Journals. 1(2), pp. 1-11

Vitae

T. Moasunep Jamir hail from Khar Village, Mokokchung District, Nagaland. He attained his initial schooling from Nagaland, and later acquired his Bachelors and Master's degree in Mechanical Engineering from L. D. College of Engineering, Ahmedabad, Gujarat University. He has briefly worked as a visiting faculty in L. D. College of Engineering, Ahmedabad, Gujarat University, and later pursued his Ph.D. from Indian Institute of Technology Guwahati, Guwahati, Assam.

Presently he is working as an Assistant Professor, in the Department of Mechanical Engineering, in Delhi Technological University (formerly Delhi College of Engineering), New Delhi.

Email: sunepbokdi@gmail.com